

Proceedings of the International Workshop on Advances in Nanomaterials
Măgurele - Bucharest, September 17-19, 2018

Proceedings of the
International Workshop on Advances in Nanomaterials
Măgurele - Bucharest, September 17-19, 2018

Editor: Victor Bârsan

Horia Hulubei Publishing House
Bucharest - Măgurele, 2018

Cover designer: Tóth Erzsébet

Book designer: Radu Dragomir

ISBN: 978-606-94603-9-9

Copyright:
Editura Horia Hulubei (Horia Hulubei Publishing House),
editura.hh@gmail.com

The Horia Hulubei Publishing House is hosted by the UNESCO Chair of
Horia Hulubei Foundation.

Foreword

This volume collects several lectures presented by invited speakers from Croatia, Macedonia, Romania and Serbia at the International Workshop on Advances in Nanomaterials, held in Măgurele-Bucharest, September 17–19, 2018. The workshop was mainly focused on (i) Low dimensional systems and heterojunctions, (ii) Size effects, quantum dots and nanomagnetism, (iii) Spintronics and multifunctionality, and (iv) Photovoltaics, photocatalysis and photonics. Its scientific aspects were supervised by an International Advisory Board, composed of Prof. Ștefan Antohe (Bucharest), Dr. Victor Bârsan (Bucharest), Dr. Victor Kuncser (Bucharest), Prof. Nenad Novkovski (Skopje), Prof. Nicola Seriani (ICTP).

The workshop is already a traditional activity, starting in 2012. It puts together researchers with different profiles - experimental, theoretical and computational physicists, chemists and engineers – mainly from Central and Eastern European countries. The scientific and financial support of ICTP - Trieste was essential for the success of these scientific meetings.

In 2018, the workshop was organized by the National Institute of Materials Physics (NIMP) with its International Center for Training and Advanced Research (Centre International de Formation et Recherche Avancée – CIFRA), by the Physics Department of the University of Bucharest and by the UNESCO Chair of the Horia Hulubei Foundation. Its main sponsors were ICTP Trieste and NIPM.

The editors are grateful to authors who contributed to this *Proceedings*. The other lecturers are also present with their abstract, included at the end of the volume. Hopefully, the publication of a proceedings volume might become a rule for the future similar workshops.

Victor Bârsan
Editor

Măgurele - Bucharest, December 2018

CONTENTS

| | |
|--|------------|
| Part I. Lectures | 1 |
| Organic and biologic thin films based photovoltaic devices: preparation, characterization and optimization Sorina Iftimie, V. A. Antohe, A. Radu and S. Antohe | 3 |
| Shaping Laguerre-Gaussian laser modes (with or without phase singularities) by using fork-shaped gratings Suzana Topuzoski, Ljiljana Janicijevic, Lyubomir Stoyanov, Ivan Stefanov and Alexander Dreischuh | 17 |
| An overview on local structure and magnetism of Fe-C nanocomposites S. G. Greculeasa, F. Dumitrache, I. I. Lungu, N. Iacob, V. Kuncser | 27 |
| AC magnetometry for hyperthermia applications Marija Perovic, Marko Boskovic, Viktor Cosic | 43 |
| Spin configurations in RE-Fe and RE-Fe-B systems and related functionalities A. E. Stanciu, C. Locovei, G. Schinteie, N. Iacob, V. Kuncser | 51 |
| Superposed Shape Memory and Magnetocaloric Effects of NiFeGa Heusler alloys. Effects of thermal treatments and of Co and Al Substitutions F. Tolea, M. Sofronie, A. D. Crisan, B. Popescu, M. Tolea | 65 |
| Interface state densities in different heterojunctions N. Novkovski, A. Paskaleva, A. Skeparovski, and D. Spassov | 75 |
| Critical behavior of an anharmonic nanoscopic solid C. Popa | 85 |
| Exact and approximate analytical solutions of Weiss equation of ferromagnetism and their experimental relevance. Theoretical aspects (I) V. Barsan | 105 |
| Exact and approximate analytical solutions of Weiss equation of ferromagnetism and their experimental relevance. Experimental aspects (II) | 127 |

| | |
|--|------------|
| V. Kuncser | |
| Part II. Abstracts of other presentations | 131 |
| | |
| | |
| | |

Part I. Lectures

Study of the physical properties of chlorophyll-a and polymers thin films for photovoltaic applications – a brief review

S. Iftimie¹, V.A. Antohe,^{1,2} A. Radu,¹ and S. Antohe^{1,3}

¹University of Bucharest, Faculty of Physics, Bucharest, Romania

²Université Catholique de Louvain, Institute of Condensed Matter and Nanosciences,
Louvain-la-Neuve, Belgium

³Academy of Romanian Scientists, Bucharest, Romania

Corresponding author: S. Antohe (Stefan Antohe), University of Bucharest, Faculty of Physics, Bucharest, Romania, Atomistilor 405, 077125, Magurele, Ilfov,
E-mail: santohe@solid.fizica.unibuc.ro

Abstract

We review part of the recent results of conductive polymers and chlorophyll-a (Chl-a) thin films based photovoltaic structures, obtained by spin-coating, in ambient atmosphere. Exploiting the advantage that Chl-a is soluble in orthogonal solvents and alcohol, the discussed photovoltaic devices involve the customization of both holes selective layer (HSL) and active layer. The obtained results indicated that the presence of Chl-a in the architecture of active layer enlarges the spectral domain, increasing the number of photo-generated charge carriers, while for HSL improves the holes collection to the front contact. A particular blend, working as HSL, based on poly(3,4-ethylenedioxythiophene)-poly(styrenesulfonate) (PEDOT:PSS) and Chl-a, in 4:1 wt.%, led to almost double value of the external quantum efficiency, in terms of reference devices.

Keywords: P3HT, PC₆₁BM, Chl-a, photovoltaics

Introduction

Nowadays, the attention gained by organic photovoltaic devices (OPVs) is strongly correlated with the unique physical and chemical properties of conductive polymers [1-3] and a particular architecture involving a 3D interpenetrating network built by mixing a conductive polymer and a fullerene derivative and denoted “bulk-heterojunction” [4-6]. Particular interest was paid to a blend based on poly(3-hexylthiophene-2,5-diyl) (P3HT) and [6,6]-phenyl-C61 butyric acid methyl ester (PC₆₁BM), working as donor and acceptor materials, respectively, due to their convenient

match of the energetic levels and high miscibility. The frequently used weight ratio between these two components is 1:1, while as solvent 1, 2-dichlorobenzene or chloroform is used. Furthermore, because it was proved that oxygen and moisture lead to serious degradation of OPVs [7, 8], usually, the fabrication and characterization of such devices are made in glove-boxes; dedicated equipments which ensure low volumes of oxygen. In order to improve both the power conversion efficiency and time stability of these kinds of structures, different configurations had been taken into account, involving the preparation methods or customizing the constitutive [9-12]; e.g. Socol et al. proved that by increasing the weight ratio of C₆₀ amount for the active layer, the photovoltaic performances of the blend heterostructures are increased due to a better charge carriers' collection to electrodes [13]. Also, Kommeren et al. had proposed the use of different solvents than the orthogonal ones and the obtained results were similar with reference devices [14] and Al-Zanganawee et al. modified the architecture of the active layer by adding functionalized single wall carbon nanotubes [15].

The conventional OPVs devices are designed in order to facilitate the holes collection to anode and the electrons to cathode, so intermediate layers working as holes selective layer (HSL) and electrons selective layer (ESL) are added. One of the frequently used HSL is poly(3,4-ethylenedioxythiophene)-poly(styrenesulfonate) (PEDOT:PSS), while as ESL, lithium fluoride (LiF) or calcium fluoride (CaF) are selected. The optimization of such kind of films had achieved the same importance as the optimization of the active layer, because the generated photo-current is a measure of the photovoltaic performances of the devices.

Chlorophyll-a (Chl-a) is a natural porphyrin, the key-molecule in the photosynthesis process, and has similar p-type electrical conductivity. Usually, Chl-a can be easily extracted by chromatography [16] and has the advantage of being soluble in both orthogonal solvents and alcohol. Despite its great potential for photovoltaic applications [17,18], a relatively small number of papers are focused on this topic because some issues are still waiting an answer. One of them is related to poor time stability of Chl-a due to the non-regeneration process of it.

In this paper we review few recent results related to conductive polymers and Chl-a thin films based photovoltaic devices. Photo-electrical behavior of different architectures involving the customization of either the HSL or active layer is discussed in terms of conventional structures. The reported results indicated that Chl-a can be a suitable candidate for OPVs because enlarges the spectral domain of the active layer, and, also, as constitutive of HSL improves the short-circuit current density.

Experimental procedures

Fabrication routine and materials. Chlorophyll-a and conductive polymers thin films based photovoltaic structures were fabricated by spin-coating, in ambient atmosphere, taking into account different architectures. First step of the preparation routine consisted in the deposition of a hole selective layer (HSL) onto optical glass substrates covered with indium tin oxide (ITO) working as anode. Before the HSL deposition, the substrates were subsequently cleaned in acetone, isopropyl alcohol and deionized water for 15 minutes each procedure. In order to increase the charge carriers collection to the front electrode, customized configurations of the HSL based on Chl-a and poly(3,4-ethylenedioxythiophene)-poly(styrenesulfonate) (PEDOT:PSS) were build, e.g. bi-layer structures PEDOT:PSS/Chl-a and Chl-a/PEDOT:PSS and PEDOT:PSS + Chl-a (4:1) mixture. Likewise, the active layer was tailored too as blend between poly(3-hexylthiophene-2,5-diyl) (P3HT), as donor, [6,6]-phenyl-C₆₁ butyric acid methyl ester (PC₆₁BM), as acceptor, and Chl-a, in different weight ratios. For some obtained samples, the improvement of electrons collection to back electrode was facilitated by the deposition of an ultra-thin film of lithium fluoride (LiF, 10 nm), by thermal evaporation (TVE). To complete the photovoltaic structures an aluminum (Al) cathode was deposited, by TVE too. The working parameters used to grow the HSL were as follows: the angular velocity 2000 rpm and the speed time 40 seconds, while in the case of the active layer a two-step procedure was used; first the angular velocity was set to 650 rpm for 60 seconds, and second it was increased to 1500 rpm for 15 seconds. To remove all solvent traces of both HSL and active layer, annealing was performed at 120°C for 1h30 for the first and at 110°C for 30 minutes, for the latter. The active area of all fabricated photovoltaic structures was 0.4 cm². For ease of discussion, in Table 1 the prepared architectures together with their tailored holes selective layers and active films are presented.

Characterization techniques. Morphological and surface features of fabricated thin films were analyzed by scanning electron microscopy (SEM) and atomic force microscopy (AFM), respectively. The SEM equipment used was a TESCAN VEGA, XMU model, while the AFM was a MDT Ntegra machine. Optical investigations of active layers were performed in the wavelength range of 300 – 800 nm, covering the absorption bands of P3HT, PCBM and Chl-a. Parameters characterizing photovoltaic structures i.e. short-circuit current (I_{sc}), open circuit voltage (V_{oc}) and fill factor (FF) were determined by current-voltage (I-V) measurements, at room temperature, using a Keithley 2400 sourcemeter and a Newport Oriel solar simulator, working in AM 1.5 conditions (a solar zenith of 48.2° and an incident power density of 100 W/cm²). The external quantum efficiency (EQE) values of fabricated devices were calculated by action spectra, at room temperature, too.

Table 1. The configurations of fabricated photovoltaic structures and their active layers

| Structure | Hole selective layer | Active layer | Reference |
|---|-----------------------|---|-----------|
| glass/ITO/PEDOT:PSS/P3HT:PC ₆₁ BM (1:1, wt.)/Al | PEDOT:PSS | P3HT:PC ₆₁ BM (1:1) | [19] |
| glass/ITO/PEDOT:PSS/P3HT:PC ₆₁ BM:Chl-a (1:1:10, wt.)/Al | PEDOT:PSS | P3HT:PC ₆₁ BM:Chl-a (1:1:10) | [19] |
| glass/ITO/PEDOT:PSS/Chl-a/P3HT:PC ₆₁ BM (1:1, wt.)/Al | PEDOT:PSS/Chl-a | P3HT:PC ₆₁ BM (1:1) | [19] |
| glass/ITO/PEDOT:PSS:Chl-a(4:1, wt.)/P3HT:PC ₆₁ BM(1:1, wt.)/LiF/Al | PEDOT:PSS:Chl-a (4:1) | P3HT:PC ₆₁ BM (1:1) | [20] |
| glass/ITO/PEDOT:PSS/P3HT:PC ₆₁ BM:Chl-a (1:1:1, wt.)/LiF/Al | PEDOT:PSS | P3HT:PC ₆₁ BM:Chl-a (1:1:1) | [20] |
| glass/ITO/Chl-a/PEDOT:PSS/P3HT:PC ₆₁ BM (1:1, wt.)/LiF/Al | Chl-a/PEDOT:PSS | P3HT:PC ₆₁ BM (1:1) | [20] |

Results and discussion

The mixture between P3HT and PCBM is commonly used as active layer in the field of bulk-heterojunction photovoltaic devices due to an appropriate energy level alignment of their highest occupied molecular orbital (HOMO) and lowest unoccupied molecular orbital (LUMO), related to valence band and conduction band, respectively, of inorganic semiconductors. The usage of buffer layers, such as HSL or electron selective layer (ESL), e.g. LiF, or the fabrication of tailored HSL involving Chl-a demands suitable energy levels of constitutive. The energy band offset diagram of component materials of the prepared samples is presented in Figure 1, together with the chemical structure of P3HT, PCBM and Chl-a.

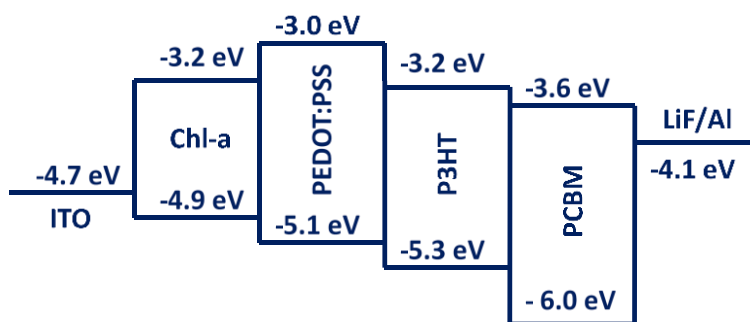


Fig. 1a – Diagram energy levels of component materials of prepared photovoltaic devices.

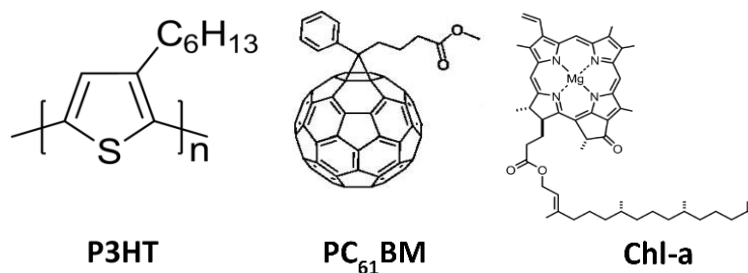


Fig. 1b – Chemical structure of P3HT, PC₆₁BM and Chl-a.

One may notice the very good match of LUMO of Chl-a with LUMO of P3HT, in one hand, and on the other hand the match of HOMO of Chl-a with HOMO of PEDOT:PSS. Due to this characteristic features, Chl-a offers the advantage of customizing both the HSL and the active layer. While PEDOT:PSS is a heavily doped *p*-type semiconductor [21,22], Chl-a has similar *p*-type electrical conductivity, and either a mixture between these constitutive or a bi-layer configuration is possible to decrease the energetic barrier between the active layer and front electrode, in order to improve holes collection, if was optimized. Nevertheless, an architecture such as Chl-a/PEDOT:PSS seems to be more appropriate than PEDOT:PSS/Chl-a used in glass/ITO/PEDOT:PSS/Chl-a/P3HT:PC₆₁BM (1:1, wt.%) /Al structures from Table 1.

In order to determine how the presence of Chl-a influences the surface morphology of fabricated samples, AFM images and SEM micrographs were made, and are presented in Figure 2 for glass/ITO/Chl-a/P3HT:PC₆₁BM (1:1, wt.%), glass/ITO/P3HT:PC₆₁BM:Chl-a (1:1:10, wt.%) and glass/ITO/P3HT:PC₆₁BM (1:1, wt.%) thin films. By using the Gwyddion software package the root mean square (RMS) and roughness average (R_a) parameters were calculated, and are summarized in Table 2.

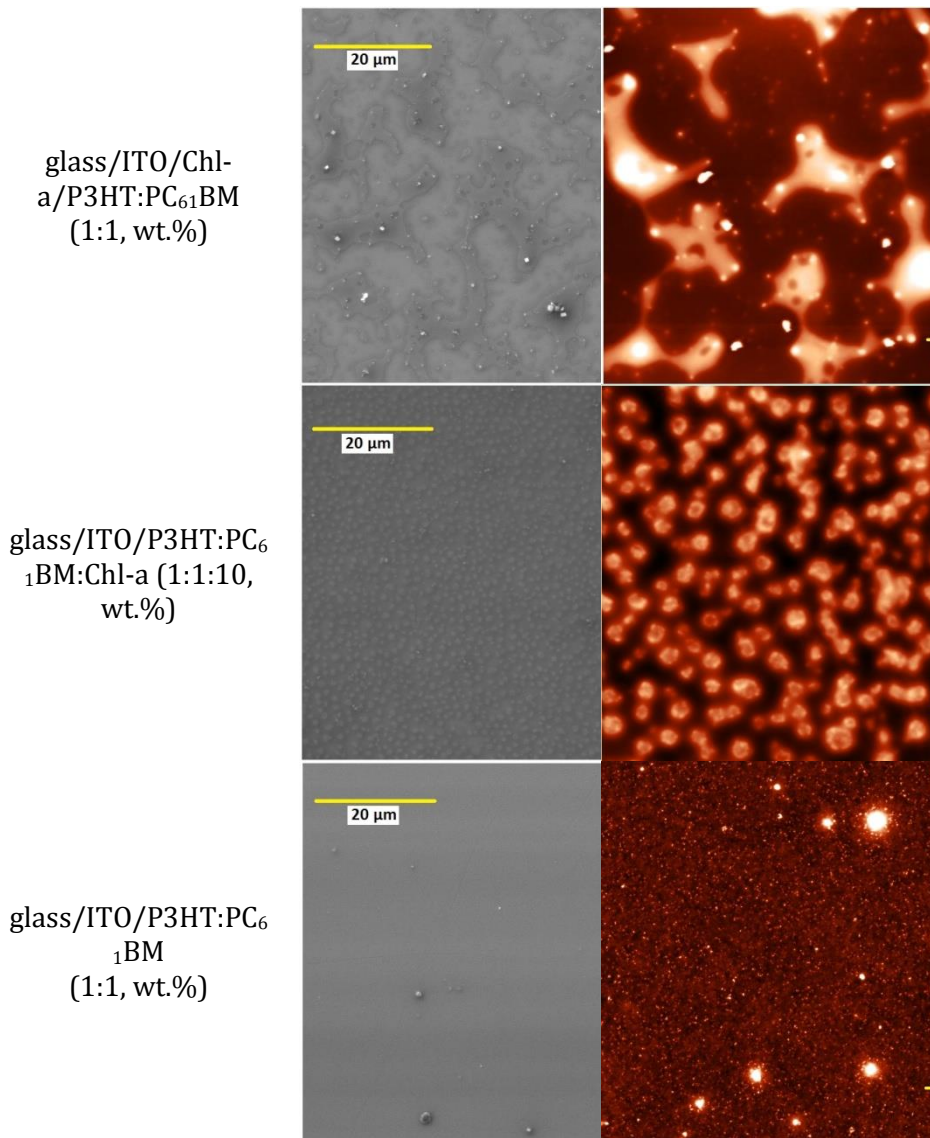


Fig. 2 – SEM micrographs and AFM images of fabricated glass/ITO/Chl-a/P3HT:PC₆₁BM (1:1, wt.%), glass/ITO/P3HT:PC₆₁BM:Chl-a (1:1:10, wt.%) and glass/ITO/P3HT:PC₆₁BM (1:1, wt.%) thin films. For the AFM images the scanned area was 25 μm × 25 μm, working in non-contact mode [19].

Table 2. Calculated values of root mean square (RMS) and roughness average (R_a) of growth glass/ITO/Chl-a/P3HT:PC₆₁BM (1:1, wt.%), glass/ITO/P3HT:PC₆₁BM:Chl-a (1:1:10, wt.%) and glass/ITO/P3HT:PC₆₁BM (1:1, wt.%) thin films. The software package used was Gwyddion.

| Structure | Thickness (nm) | RMS (nm) | R_a (nm) |
|---|----------------|----------|------------|
| Chl-a/P3HT:PC ₆₁ BM (1:1, wt.%) | 206 | 54 | 43 |
| P3HT:PC ₆₁ BM:Chl-a (1:1:10, wt.%) | 277 | 56 | 47 |
| P3HT:PC ₆₁ BM (1:1, wt.%) | 175 | 2.4 | 1.1 |

While RMS is defined as the square root of the distribution of the surface heights, R_a is related to the mean height calculated for the whole scanned area. The values presented in Table 2 were determined using the following expressions [23]:

$$RMS = \sqrt{\frac{1}{L} \int_0^L |(y(x))^2| dx} \quad (1)$$

$$R_a = \frac{1}{L} \int_0^L |z(x)| dx \quad (2)$$

in which L is the length of the profile on x-axis and $y(x)$ is the variation of the height from the profile line for each data point, and in equation (2) z is the function that describes the surface profile analyzed in terms of height (z) and position (x) [24,25].

From both RMS and R_a it can be inferred that the surface of P3HT:PC₆₁BM (1:1, wt.%) thin films is more smooth and homogeneous than that of glass/ITO/Chl-a/P3HT:PC₆₁BM (1:1, wt.%) and glass/ITO/P3HT:PC₆₁BM:Chl-a (1:1:10, wt.%) samples, proving the good miscibility between the components, i.e. the solvent used was 1,2-dichlorobenzene. By adding the Chl-a either in the bi-layer architecture or in the mixture the values of RMS and R_a have increased about 200 times. In the case of glass/ITO/P3HT:PC₆₁BM:Chl-a (1:1:10, wt.%) layers, this behavior can be associated with the fact that Chl-a molecules are too large and cannot occupy the sites in the P3HT matrix, leading to the creation of clusters at the surface. As SEM micrographs and AFM images indicate, these clusters are around 1 μ m diameter and are relatively uniform distributed. It is well-known that subjected to annealing at temperatures around 100°C, the P3HT:PC₆₁BM (1:1, wt.%) blend show an early crystalline structure [26] and one can easily notice the similarity of the form of the clusters indicated by AFM images and SEM micrographs. We assume that the pre-crystallization process involved not only P3HT and PC₆₁BM, but affected the

Chl-a molecules, too. Nevertheless, it is difficult to conclude if the sites correlated with Chl-a are preferential or randomly chose. For glass/ITO/Chl-a/P3HT:PC₆₁BM (1:1, wt.%) configuration, the increase of RMS are R_a values is related to a physically non-optimized interface between Chl-a and P3HT:PC₆₁BM (1:1, wt.%), as AFM and SEM investigations showed, despite that Chl-a was deposited from a methanol solution. Due to the fact that Chl-a molecules are large, part of the mixture between P3HT:PC₆₁BM (1:1, wt.%) get in, and clusters of about 5 μm were formed. Moreover, the bi-layer type architecture led to direct contact between components, so clusters with random forms were created.

The optical absorption spectra of Chl-a, P3HT:PC₆₁BM (1:1, wt.%) and P3HT:PC₆₁BM:Chl-a (1:1:10, wt.%) thin films are presented in Figure 3.

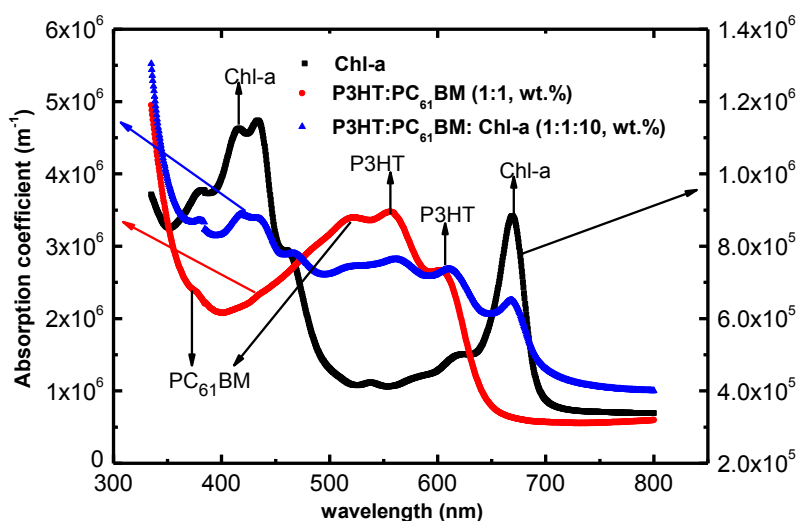


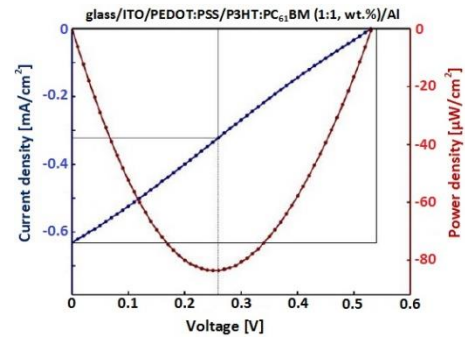
Fig. 3 – Absorption spectra of Chl-a, P3HT:PC₆₁BM (1:1, wt.%) and P3HT:PC₆₁BM:Chl-a (1:1:10, wt.%) thin films, determined in the wavelength range of 300 – 800 nm, at room temperature [19].

One may observe that despite the smaller absorption coefficient values of individual Chl-a layer, the spectral domain that covers, it is complementary with that of P3HT:PC₆₁BM (1:1, wt.%). Between the particular maxima of Chl-a located at 670 nm (Q-band) and 435 nm (Soret band), the specific absorption features of P3HT at 550 nm and at 600 nm, attributed to π - π^* transitions, are easily visible [27]. PC₆₁BM is a methano-fullerene derivative with no notable optical absorption below 550 nm, however the footprint of a peak can be identified around 370 nm. Nevertheless, the UV absorption maxima of such materials are highly dependent of the solvent used, as L.-L. Deng and collaborator showed [28].

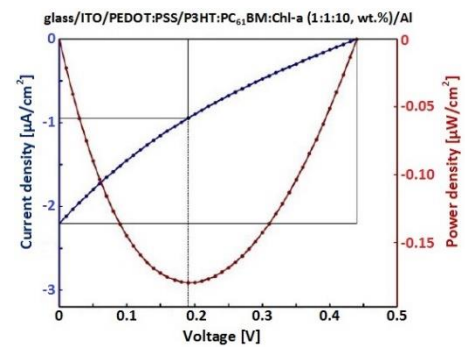
Even though the general optical absorption decreases, the spectral domain covered by P3HT:PC₆₁BM:Chl-a (1:1:10, wt.%) thin film has been significantly enlarged from 350 to 700 nm, merging the maxima of all constitutive. Moreover, the position of peaks is slightly shifted for the ternary compound, proving that no chemical interaction took place, though efficient charge transfer between polymer chains and fullerene molecules was mentioned [29,30].

The I-V characteristics of fabricated devices, drawn in AM 1.5 conditions, are shown in Figure 4, while the calculated values of specific parameters are summarized in Table 3.

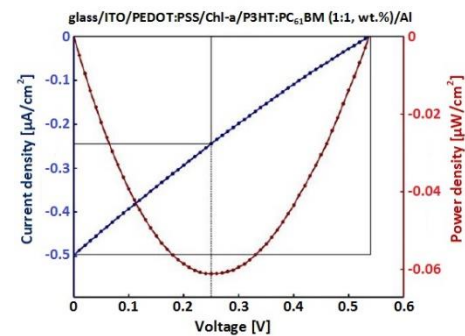
**glass/ITO/PEDOT:PSS/P3HT:PC₆₁B
M (1:1, wt.%) /Al [19]**



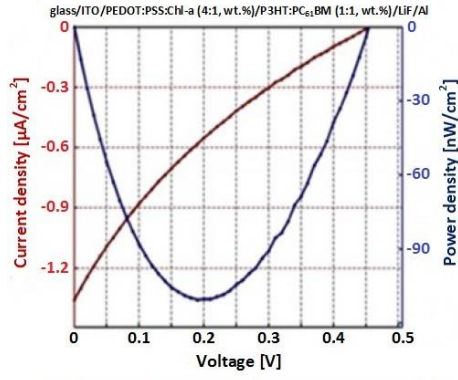
**glass/ITO/PEDOT:PSS/P3HT:PC₆₁B
M:Chl-a (1:1:10, wt.%) /Al [19]**



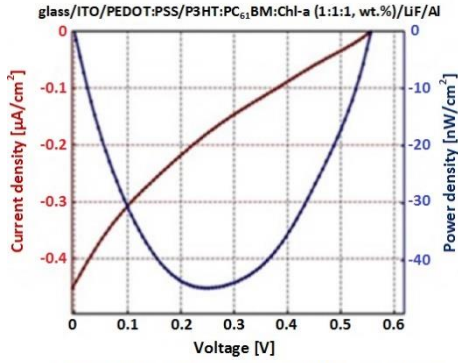
**glass/ITO/PEDOT:PSS/Chl-a
/P3HT:PC₆₁BM (1:1, wt.%) /Al [19]**



glass/ITO/PEDOT:PSS:Chl-a(4:1, wt.%) /P3HT:PC₆₁BM(1:1, wt.%) /LiF /Al [20]



glass/ITO/PEDOT:PSS/P3HT:PC₆₁BM:Chl-a (1:1:1, wt.%) /LiF /Al [20]



glass/ITO/Chl-a /PEDOT:PSS/P3HT:PC₆₁BM(1:1, wt.%) /LiF /Al [20]

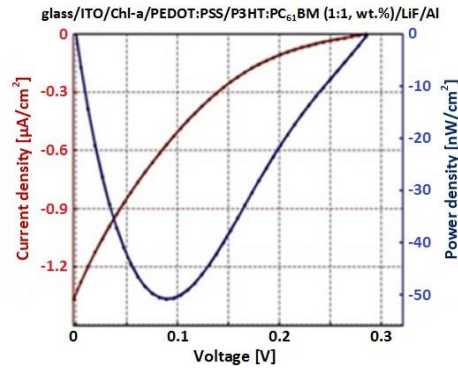


Fig. 4 – I-V characteristic of fabricated photovoltaic devices, obtained in AM 1.5 conditions, together with the maximum power density [19,20].

Table 3. Short-circuit current density (J_{sc}), open circuit voltage (V_{oc}), fill factor (FF), and external quantum efficiency (EQE) of prepared structures, calculated from I-V characteristics in the fourth quadrant (AM 1.5 conditions). All measurements were performed at room temperature.

| Structure | | J_{sc} ($\mu\text{A}/\text{cm}^2$) | V_{oc} (V) | FF (%) | EQE (%) |
|--|---------|---|-----------------|-----------|------------|
| glass/ITO/PEDOT:PSS/P3HT:PC ₆₁ BM wt.%) /Al | (1:1, | 631 | 0.54 | 25 | 18 |
| glass/ITO/PEDOT:PSS/P3HT:PC ₆₁ BM:Chl-a (1:1:10, wt.%) /Al | | 2.2 | 0.44 | 19 | 15 |
| glass/ITO/PEDOT:PSS/Chl-a/P3HT:PC ₆₁ BM wt.%) /Al | (1:1, | 0.5 | 0.54 | 23 | 21 |
| glass/ITO/PEDOT:PSS:Chl- a(4:1,wt.%) /P3HT:PC ₆₁ BM(1:1, wt.%) /LiF/Al | | 1.4 | 0.50 | 19 | 35 |
| glass/ITO/PEDOT:PSS/P3HT:PC ₆₁ BM:Chl-a wt.%) /LiF/Al | (1:1:1, | 0.5 | 0.60 | 18 | 16 |
| glass/ITO/Chl-a/PEDOT:PSS/P3HT:PC ₆₁ BM wt.%) /LiF/Al | (1:1, | 1.4 | 0.30 | 13 | 18 |

For glass/ITO/PEDOT:PSS/Chl-a/P3HT:PC₆₁BM (1:1, wt.%) /Al sample it is clear that the match of energy levels are not appropriate to facilitate the holes collection to anode, although the values of V_{oc} , FF and EQE are not very low as comparing with those of glass/ITO/PEDOT:PSS/P3HT:PC₆₁BM (1:1, wt.%) /Al conventional devices. More convenient is a tailored HSL such as Chl-a/PEDOT:PSS and this was proved by the almost three times higher value obtained for J_{sc} . In the case of architectures based on P3HT:PC₆₁BM:Chl-a (1:1:10, wt.%) and P3HT:PC₆₁BM:Chl-a (1:1:1, wt.%) active layers, the electrical results indicate that the early crystallization process observed by both AFM images and SEM micrographs improved the percolation paths of charge carriers' transport, so the short-circuit current density was fourth times higher in the case of the first one. Nevertheless, in this paper only two weight ratios of Chl-a amount blend in the active layer were discussed but further studies are required in order to fully understand the physical processes involved. A HSL as PEDOT:PSS:Chl-a (4:1, wt.%) seems to be suitable to decrease the energetic barrier between the active layer and front contact, assuring a better collection of holes, fact proved by the determined EQE value, almost double the other prepared devices. In the case of these materials, the usage of a mixture of two components with same type electrical conductivity led to better results than a bi-layer architecture of them, despite the fact that no chemical interaction took place. In this situation, we assume that the annealing performed after the deposition of the mixture has the same effect as for the P3HT:PC₆₁BM:Chl-a (1:1:10, wt.%) active layer. By using Chl-a/PEDOT:PSS as HSL, an additional energetic barrier is built and the holes collection is facilitate, but the overall performances are decreased

because the series resistance of the photovoltaic structures becomes larger. Chose of the specific weight ratio between PEDOT:PSS and Chl-a was established by taking into account electrical and photo-electrical results for different situations, e.g. (3:2), (2:3 and (1:4) (not shown here).

Conclusions

Bulk-heterojunction photovoltaic structures based on P3HT, PC₆₁BM and Chl-a were fabricated by spin-coating in ambient atmosphere, taking into account different configurations. Exploiting the advantage that LUMO of Chl-a is matching with LUMO of P3HT and HOMO of Chl-a with HOMO of PEDOT:PSS we tailored both the active layer and the HSL. In the case of active layer, two weight ratios of Chl-a amount were blended with P3HT:PC₆₁BM (1:1, wt.%), namely 1 wt.% and 10 wt.%. Both, the AFM images and SEM micrographs show that an early crystallization process took place after annealing at 110°C (30 min) for P3HT:PC₆₁BM:Chl-a (1:1:10, wt.%), improving the percolation path of charge carriers' transport. The photo-electrical measurements confirmed this feature by an increase of J_{sc} more than fourth times compared with the similar structure glass/ITO/PEDOT:PSS/P3HT:PC₆₁BM:Chl-a (1:1:1, wt.%)/LiF/Al. The overall photovoltaic performances proved a customized HSL such as PEDOT:PSS:Chl-a (4:1) is more efficient than a bi-layer architecture of Chl-a/PEDOT:PSS, despite the fact that no chemical interaction takes place between the components. A configuration as Chl-a/PEDOT:PSS introduces one a hand an additional energetic barrier that increases the series resistance of the fabricated devices and reducing the V_{oc} and one the other hand increase the defect state at the interface then increasing the recombination processes, and decreasing the photocurrent. By this study, we demonstrated that the presence of Chl-a in the configuration of the active layer enlarges the spectral domain from 350 to 700 nm, covering all the specific peaks of the component materials, while, if optimization is made, used in the architecture of HSL improves the photo-electrical behavior of the prepared photovoltaic devices.

Acknowledgements

This study was supported by the Romanian Ministry of Research and Innovation under the project 40PCCDI/2018.

References

- [1] O.P. Dimitriev, D.A. Blank, C. Ganser, C. Teichert, "Effect of the polymer chain arrangement on exciton and polaron dynamics in P3HT and P3HT:PCBM thin films", *J Phys Chem C* **122** (2018) 17096-17109.
- [2] B. Hajduk, H. Bednarski, B. Jarzabek, H. Janeczek, P. Nitschke, "P3HT:PCBM blend films phase diagram on the base of variable-temperature spectroscopic ellipsometry", *Beilstein J Nanotechnol* **9** (2018) 1108-1115.

- [3] L. Magherusan, P. Skraba, C. Besleaga, S. Iftimie, N. Dina, M. Bulgariu, C.G. Bostan, C. Tazlaoanu, A. Radu, L. Ion, M. Radu, A. Tanase, G. Bratina, S. Antohe, "Electrical and photoelectrical properties of organic photovoltaic cells based on polymer blends ITO/PEDOT/P3HT:PCBM (1:1)", *J Optoelectron Adv M* **12** (2010) 212-218.
- [4] G.A. Nemnes, S. Iftimie, A. Palici, A. Nicolaev, T.L. Mitran, A. Radu, S. Antohe, "Optimization of the structural configuration of ICBA/P3HT photovoltaic cells", *Appl Surf Sci* **424** (2017) 264-268.
- [5] M. Girtan, "On the stability of the electrical and photoelectrical properties of P3HT and P3HT:PCBM blends thin films", *Org Electron* **14** (2013) 200-205.
- [6] N. Sharma, C.M.S. Negi, A.S. Verma, S.K. Gupta, "C60 concentration influence on MEH-PPV:C60 bulk-heterojunction-based Schottky devices", *J Electron Mater* **47** (2018) 7023-7033.
- [7] M. Girtan, "New Trends in Solar Cells Research – Future Solar Energy Devices", *SpringerBriefs in Applied Sciences and Technology*, 2018, 45-75.
- [8] V. Singh, "Degradation of fill factor in P3HT:PCBM based organic solar cells", *Cur Appl Phys* **17** (2017) 1450-1454.
- [9] J. Al-Zanganawee, M. Al-Timimi, A. Pantazi, O. Brincoveanu, C. Moise, R. Mesterca, D. Balan, S. Iftimie, M. Enachescu, "Morphological and optical properties of functionalized SWCNTs:P3OT nanocomposite thin films, prepared by spin-coating", *J Ovonic Res* **12** (2016) 201-207.
- [10] J. Al-Zanganawee, S. Iftimie, A. Pantazi, R. Mesterca, A. Jderu, S. Antohe, M. Enachescu, "On the physical properties of inverted photovoltaic structures based on P3OT:F-SWCNTs active layer", *J Ovonic Res* **14** (2018) 287-292.
- [11] Y.A.M. Ismail, "Aluminum nanoparticles prepared by ultrasonic ablation technique inside the active layer of organic solar cells", *J Nano Res-Sw* **51** (2018) 48-60.
- [12] U. Jabeen, T. Adhikari, S.M. Shah, J.M. Nunzi, A. Badshah, I. Ahmad, "Enhancement of efficiency by embedding ZnS and Mn-doped ZnS nanoparticles in P3HT:PCBM hybrid solid state solar cells", *Euro Phys J-Appl Phys* **78** (2017) 34810.
- [13] M. Socol, N. Preda, A. Stanculescu, C. Breazu, C. Florica, F. Stanculescu, S. Iftimie, M. Girtan, G. POPescu-Pelin, G. Socol, "Organic heterostructures deposited by MAPLE on AZO substrate", *Appl Surf Sci* **417** (2017) 196-203.
- [14] S. Kommeren, M.J.J. Coenen, T.M. Eggenhuisen, T.M.W.L. Slaats, H. Gorter, P. Groen, "Combining solvents and surfactants for inkjet printing PEDOT:PSS on P3HT/PCBM in organic solar cells", *Org Electron* **61** (2018) 282-288.
- [15] J. Al-Zanganawee, S. Iftimie, A. Pantazi, O. Brincoveanu, R. Mesterca, A. Radu, S. Antohe, M. Enachescu, "On the morphological, electrical and photoelectrical properties of P3HT:F-SWCNTs based photovoltaic cells", *J Ovonic Res* **13** (2017) 63-70.
- [16] L. Tugulea, S. Antohe, "Photovoltaic characteristics of Si/Chla structure", *Photosynth Res* **34** (1992) 167-167.
- [17] S. Antohe, L. Tugulea, V. Gheorghe, V. Ruxandra, I. Caplanus, L. Ion, "Electrical and photovoltaic properties of ITO/chlorophyll a/TPyP/Al p-n junction cell", *Phys Status Solidi A* **153** (1996) 581-588.
- [18] S. Shoji, H. Tamiaki, "Supramolecular light-harvesting antenna system by co-aggregates of zinc (bacterio) chlorophyll a derivatives with biomimetic chlorosomal self-assemblies", *Dyes Pigm* **160** (2019) 514-518.

- [19] S. Iftimie, M.E. Barbinta-Patrascu, D. Gazdaru, A. Radu, B. Bitu, D. Staicu, N. Korganci, L. Ion, S. Antohe, "Photovoltaic structures based on biologic/polymeric semiconducting thin films", *Dig J Nanomater Bios* **10** (2015) 1249-1255.
- [20] B. Bitu, S. Iftimie, A. Radu, V.A. Antohe, D. Coman, C. Miron, D. Staicu, L. Dan, L. Ion, S. Antohe, "On the electrical and photo-electrical behavior of the photovoltaic cells based on polymeric and chlorophyll-a thin films", *P Romanian Acad A* (just accepted to publication).
- [21] D. Khodagholy, J. Rivnay, M. Sessolo, M. Gurfinkel, P. Leleux, L.H. Jimison, E. Stavrinidou, T. Herve, S. Sanaur, R.M. Owens, G.G. Malliaras, "High transconductance organic electrochemical transistors", *Nat Commun* **4** (2013) 2133.
- [22] S. Zhang, P. Kumar, A.S. Nouas, L. Fontaine, H. Tang, F. Cicoira, "Solvent-induced changes in PEDOT:PSS films for organic electrochemical transistors", *APL Mater* **3** (2015) 014911.
- [23] S. Iftimie, A. Radu, M. Radu, C. Besleaga, I. Pana, S. Craciun, M. Girtan, L. Ion, S. Antohe, "Influence of PEDOT:PSS layer on the performances of bulk-heterojunction photovoltaic cells based on MEH-PPV:PCBM (1:4) polymeric blends", *Dig J Nanomater Biostruct* **6** (2011) 1631-1638.
- [24] B. Rajesh Kumar, T. Subba Rao, "AFM studies on surface morphology, topography and texture of nanostructured zinc aluminum oxide thin films", *Dig J Nanomater Bios* **7** (2012) 1881-1889.
- [25] R.R.L. De Oliveira, D.A. Albuquerque, T.G.S. Cruz, F.M. Yamoji, F.L. Leite, "Chapter 7: Measurement of the Nanoscale Roughness by Atomic Force Microscopy – Basic Principles and Applications", *Atomic Force Microscopy: Imaging, Measuring and Manipulating Surfaces at the Atomic Scale*, ed. Victor Bellito, ISBN: 978-953-51-0414-8.
- [26] S. Antohe, S. Iftimie, L. Hrostea, V.A. Antohe, M. Girtan, "A critical review of photovoltaic cells based on organic monomeric and polymeric thin film heterojunctions", *Thin Solid Films* **642** (2017) 219-231.
- [27] V. Shrotriya, J.Y. Ouyang, R.J. Tseng, G. Li, Y. Yang, "Absorption spectra modification in poly(3-hexylthiophene):methanofullerene blend thin films", *Chem Phys Lett* **411** (2005) 138-143.
- [28] L.-L. Deng, S.-L. Xie, C. Yuan, R.-F. Liu, J. Feng, L.-C. Sun, X. Lu, S.-Y. Xie, R.-B. Huang, L.-S. Zheng, "High LUMO energy level C60(OCH3)4 derivatives: Electronic acceptors for photovoltaic cells with higher open-circuit voltage", *Sol. Energy Mater Sol Cells* **111** (2013) 193-199.
- [29] Z.W. Jin, J.Z. Wang, "PIN architecture for ultrasensitive organic thin film photoconductors", *Sci Rep* **4** (2014) 5331.
- [30] S. Iftimie, A. Majkic, C. Besleaga, V.A. Antohe, A. Radu, M. Radu, I. Arghir, C. Florica, L. Ion, G. Bratina, S. Antohe, "Study of electrical and optical properties of ITO/PEDOT/P3HT:PCBM(1:1)/LiF/Al photovoltaic structures", *J Optoelectron Adv M* **12** (2010) 2171-2175.

Transformation of circularly obstructed Bessel beam by the spiral phase plate

Suzana Topuzoski* and Ljiljana Janicijevic

*Faculty of Natural Sciences and Mathematics, Institute of Physics,
University "Ss. Cyril and Methodius," Skopje-1000, Republic of Macedonia*

*Corresponding author: suzana_topuzoski@yahoo.com

Abstract. We present a theoretical study about the transformation of a nondiverging Bessel beam with phase singularity n , which is transversally truncated by a circular aperture, in the process of diffraction by the spiral phase plate with integer topological charge p . The diffracted wave field is described by the derived expressions for its amplitude and intensity distributions, followed by the expressions for the vortex radius and propagation interval.

1. Introduction

Durnin has discovered that the Helmholtz equation has a class of "diffraction-free mode solutions"-they are beams whose transverse intensity profiles are remarkably resistant to the diffractive spreading [1,2,3]; because of this they can be also called the nonspreading or nondiverging beams. The simplest of them is the beam described by the Bessel function of the first kind and zeroth order, named the zeroth-order Bessel beam (BB), whose central core is bright and is surrounded by successive dark and bright rings, and it doesn't possess a screw (vortex) phase singularity [1]. The high-order Bessel beams (described by high-order Bessel functions) have dark core along their propagation axes (with zero intensity), surrounded by successive bright and dark rings. They can possess vortex phase singularity (i.e. optical vortex) on the optical axis and helicoidal wavefronts, which characterize them as vortex beams.

Mathematically the Bessel beam can contain an infinite number of rings, meaning that over an infinite area it would carry infinite power. However, as Durnin and his coworkers showed in [2] an approximation to a Bessel beam (a quasi-Bessel beam) can be made practically. A zeroth-order BB beam was generated by illuminating an annular slit, placed in the focal plane of a lens, with a collimated beam [2], by using a conical lens (axicon) [4], or, by means of holographic elements having transmission function of axicon type $t(r) = \exp[-i2\pi r/r_0]$, where r is the radial coordinate and r_0 is a constant [5]. By multiplying the axicon transmission function with a

complex, azimuthally varying factor $\exp(ip\varphi)$, and drawing the system of lines of maximum phase, a binary amplitude grating was achieved; its photo-reduced version was used in experiment for producing a high-order Bessel beam (when $p \neq 0$) [6].

The phase function $\exp(ip\varphi)$ is the transmission function of the optical element named the spiral phase plate (SPP), whose phase increases along the azimuthal coordinate φ , p times from 0 to 2π ; p is integer showing the phase singularity order or the value of the topological charge (TC). SPP is well known optical element which transforms the Gaussian beam into an output vortex beam [7, 8, 9].

In the work of J. Arlt and K. Dholakia [10], an axicon was illuminated by a Laguerre-Gaussian beam with topological charge l , and a high-order Bessel beam with same TC l was observed in a defined propagation interval. In [11] a method for generating nondiverging vortex Bessel beam when a Laguerre-Gaussian beam with azimuthal mode number n and zeroth radial mode number illuminates a helical axicon placed in the plane of the beam waist, is presented. The helical axicon [12] is a hybrid optical element consisted of an axicon and spiral phase plate (SPP). In [11] it is shown that the incident beam TC can be increased or reduced by the value of the helical axicon TC, or it can be annulled.

Here we theoretically study the transformation of a nondiverging Bessel beam with phase singularity n , which is transversally truncated by a circular aperture, in the process of diffraction by the SPP with integer topological charge p . Analytical expressions describing the diffracted wave-field amplitude and intensity distributions are derived and analyzed. They are followed by definitions of expressions for the vortex radius and for the propagation interval of the diffracted nondiverging beam. Also, a formula for the diffracted wave field is given, when the incident BB is not obstructed by the circular aperture.

2. Definition of the SPP transmission function and the incident beam

The transmission function of the spiral phase plate is written as

$$T(r, \varphi) = \exp(\pm ip\varphi), \quad (1)$$

where p is the value of its TC. The TC can be positive or negative ($\pm p$), depending on the direction of rotation of the helicoidal phase (whether it is clockwise or counter-clockwise oriented).

The transverse amplitude profile of the incident nondiverging beam is described by a Bessel function of the first kind and $|n|$ th order (n is integer), $J_n(k\alpha_0 r)$, where r is radial coordinate, $k = 2\pi/\lambda$ is wave number (with λ being the light wavelength) and $k\alpha_0$ is the radial component of the wave vector. The beam is truncated in the transversal plane with a circular aperture of radius R and this is described with the function

$\text{circ}\left(\frac{r}{R}\right) = \begin{cases} 1, & \text{for } r \leq R \\ 0, & \text{otherwise} \end{cases}$. Thus, in the plane with polar coordinates (r, φ) , at distance ζ , the incident beam wave amplitude can be written as

$$U(r, \varphi, \zeta) = \text{circ}\left(\frac{r}{R}\right) A(\zeta) \exp(-ik\zeta) J_n(k\alpha_0 r) \exp(in\varphi). \quad (2)$$

For $n=0$ the beam Eq. (2) does not have a phase singularity, whereas, for $n \neq 0$ it possesses a phase singularity of $|n|$ th order and its optical axis is dark. We will consider n with positive value.

In [11] where the transformation of a Laguerre-Gaussian beam with zeroth radial mode number and azimuthal mode number n , into a nondiverging vortex Bessel beam (as that given by Eq.(2)) by using the helical axicon with TC p , is studied, the parameter α_0 is: $\alpha_0 = (n'-1)\gamma$, with n' denoting the axicon refractive index and γ being the axicon base angle. The diffracted beam has TC equal to $n+p$. One should point out that the incident beam waist is in the axicon base plane. As special case of incident beam of mode $(n=0, l=0)$ i.e. Gaussian mode on the helical axicon, the output Bessel beam will have same TC as that of the helical axicon. If only the axicon is present, then the Gaussian beam transforms into zeroth-order BB (within given propagation interval and in paraxial approximation). Then, the function $A(\zeta)$ appearing in Eq. (2) as aperture function will be:

$$A(\zeta) \propto \left(\frac{\sqrt{2}\zeta}{w_0/\alpha_0}\right)^{1/2} \exp\left[-\frac{\zeta^2}{(w_0/\alpha_0)^2}\right] \exp(ik\alpha_0^2\zeta/2) \quad (\text{where } w_0 \text{ is the Gaussian beam waist radius}).$$

3. The diffracted wave field amplitude and intensity

In the observation screen $\Pi(\rho, \theta, z)$ situated a distance $(z - \zeta)$ from the diffractive optical element plane, the wave field in the point (ρ, θ, z) can be calculated starting from the Fresnel-Kirchhoff integral [13]

$$U(\rho, \theta, z) = \frac{ik}{2\pi(z-\zeta)} \exp\left\{-ik\left[(z-\zeta) + \frac{\rho^2}{2(z-\zeta)}\right]\right\} \times \iint_{\Delta} T(r, \varphi) U(r, \varphi, \zeta) \exp\left[-i\frac{k}{2}\left(\frac{r^2}{z-\zeta} - \frac{2r\rho\cos(\varphi-\theta)}{z-\zeta}\right)\right] r \, dr \, d\varphi. \quad (3)$$

After the transmission function and the incident beam are involved in Eq. (3), the integration over the azimuthal variable has been performed by using the Jacoby-Anger identity for Bessel function [14]:

$\exp(ia \cos b) = \sum_{s=-\infty}^{\infty} i^s J_s(a) \exp(isb)$ and the Dirac delta function definition:

$\int_0^{2\pi} \exp[i\varphi(a-b)] d\varphi = 2\pi \delta_{a,b}$. Thus, the diffracted wave field amplitude Eq.

(3) can be written in the form

$$U(\rho, \theta, z) = \frac{ikA(\zeta)}{z-\zeta} \exp\left[-ik\left(z + \frac{\rho^2}{2(z-\zeta)}\right)\right] \exp[i(n \pm p)(\theta + \pi/2)] Y(\rho, z), \quad (4)$$

where the integral over the radial variable is denoted as

$$Y(\rho, z) = \int_0^{\infty} \text{circ}\left(\frac{r}{R}\right) J_n(k\alpha_0 r) J_{|n \pm p|}\left(\frac{k\rho}{z-\zeta} r\right) \exp\left[-\frac{ikr^2}{2(z-\zeta)}\right] r dr. \quad (5)$$

In order to solve the integral Eq. (5) we will apply the trigonometric approximation for the Bessel function $J_n(k\alpha_0 r)$ when its argument has big value, which, except for $r=0$, is justified because of the presence of the wavelength in the denominator of the argument [15]

$$J_\nu(x) \approx \sqrt{\frac{2}{\pi x}} \cos\left[x - (2\nu+1)\pi/4\right] = \frac{1}{\sqrt{2\pi x}} \left\{ \exp\left[i\left(x - (2\nu+1)\frac{\pi}{4}\right)\right] + \exp\left[-i\left(x - (2\nu+1)\frac{\pi}{4}\right)\right] \right\} \quad (6)$$

for the values: $\nu = n$, $x = k\alpha_0 r$. Then Eq. (5) transforms into

$$Y(\rho, z) = \frac{1}{\sqrt{2\pi}} \frac{1}{\sqrt{k\alpha_0}} \left\{ \exp[-i(2n+1)\pi/4] \int_0^{\infty} \text{circ}\left(\frac{r}{R}\right) J_{|n \pm p|}\left(\frac{k\rho}{z-\zeta} r\right) \exp\left[-ik\left(\frac{r^2}{2(z-\zeta)} - \alpha_0 r\right)\right] r^{1/2} dr \right. \\ \left. + \exp[i(2n+1)\pi/4] \int_0^{\infty} \text{circ}\left(\frac{r}{R}\right) J_{|n \pm p|}\left(\frac{k\rho}{z-\zeta} r\right) \exp\left[-ik\left(\frac{r^2}{2(z-\zeta)} + \alpha_0 r\right)\right] r^{1/2} dr \right\}. \quad (7)$$

Both of the integrals appearing in the previous equation,

$$Y_{1,2} = \int_0^{\infty} \text{circ}\left(\frac{r}{R}\right) J_{|n \pm p|}\left(\frac{k\rho}{z-\zeta} r\right) \exp\left[-ik\left(\frac{r^2}{2(z-\zeta)} \mp \alpha_0 r\right)\right] r^{1/2} dr,$$

are solved by using the stationary phase method [13,16]. Namely, each of the integrals in

Eq. (7) is of type $Y' = \int_0^{\infty} f(r) \exp[-ik\mu(r)] dr$, and according to this method, its

solution can be evaluated around the critical point r_c (which contributes

mostly in the diffraction integral) as $Y' \approx \frac{f(r_c) \exp[-ik\mu(r_c)]}{[k\mu''(r_c)]^{1/2}}$. The value of the

critical point is obtained when the first derivative of the function $\mu(r)$ is set

to zero i.e. $\mu'(r) = 0$, while $\mu''(r_c)$ denotes the value of the second derivative

at the critical point.

For both of the integrals Y_1 and Y_2 the function $f(r)$ is same

$f(r) = r^{1/2} \text{circ}\left(\frac{r}{R}\right) J_{|n\pm p|}\left(\frac{k\rho r}{z-\zeta}\right)$. However, they have different functions

$\mu(r)$: $\mu_1(r) = \frac{r^2}{2(z-\zeta)} - \alpha_0 r$ and $\mu_2(r) = \frac{r^2}{2(z-\zeta)} + \alpha_0 r$, and because of

this their stationary points are different: $(r_c)_1 = \alpha_0(z-\zeta)$ and $(r_c)_2 = -\alpha_0(z-\zeta)$. After evaluating these integrals around the respective stationary points, Eq. (7) gets the form

$$Y = \frac{(z-\zeta)}{k\sqrt{2\pi}} \exp\left[\frac{ik\alpha_0^2(z-\zeta)}{2}\right] J_{|n\pm p|}(k\alpha_0\rho) \times \left\{ \text{circ}\left(\frac{z-\zeta}{R/\alpha_0}\right) \exp[-i(2n+1)\pi/4] + i(-1)^{|n\pm p|} \text{circ}\left(-\frac{z-\zeta}{R/\alpha_0}\right) \exp[i(2n+1)\pi/4] \right\}. \quad (8)$$

Finally, when the previous equation (8) is involved in Eq. (4) the diffracted wave field amplitude is obtained as

$$U(\rho, \theta, z) = \frac{i}{\sqrt{2\pi}} A(\zeta) \exp\left[-ik\left(z + \frac{\rho^2}{2(z-\zeta)} - \frac{\alpha_0^2(z-\zeta)}{2}\right)\right] \exp[i(n\pm p)(\theta + \pi/2)] \times J_{|n\pm p|}(k\alpha_0\rho) \left\{ \text{circ}\left(\frac{z-\zeta}{R/\alpha_0}\right) \exp[-i(2n+1)\pi/4] + i(-1)^{|n\pm p|} \text{circ}\left(-\frac{z-\zeta}{R/\alpha_0}\right) \exp[i(2n+1)\pi/4] \right\}. \quad (9)$$

The second term in the sum into the bracket in Eq. (9) denotes the virtual beam propagating in the negative direction of the z axis, and will not be considered further; so, the wavefield of the real diffracted beam in Eq. (9) has amplitude

$$U(\rho, \theta, z) = \frac{i}{\sqrt{2\pi}} A(\zeta) \exp\left[-ik\left(z + \frac{\rho^2}{2(z-\zeta)} - \frac{\alpha_0^2(z-\zeta)}{2}\right)\right] \exp[-i(2n+1)\pi/4] \times \exp\left[i(n\pm p)\left(\theta + \frac{\pi}{2}\right)\right] \text{circ}\left(\frac{z-\zeta}{R/\alpha_0}\right) J_{|n\pm p|}(k\alpha_0\rho). \quad (10)$$

The output beam, Eq. (10), is Bessel beam, nondiverging within the propagation interval $[\zeta, (z-\zeta)_{\max}]$, where $(z-\zeta)_{\max} = \frac{R}{\alpha_0} = \frac{R}{(n-1)\gamma}$. It is

also a vortex beam with central dark core, except for the case when $n-p=0$ is satisfied (then the beam will be chargeless and with central bright core). The topological charge of the diffracted beam can be increased (when both the incident BB and the SPP have same in sign TCs) or reduced (when the TC of the incident beam is with opposite sign than that of the SPP) compared to that of the incident beam, or equal to zero (when the BB and the SPP have same in value but opposite in sign TCs). The wave field intensity calculated as $I(\rho, \theta, z) \propto |U(\rho, \theta, z)|^2$ is given by

$$I(\rho, \theta, z) = \frac{1}{2\pi} |A(\zeta)|^2 \text{circ}\left(\frac{z-\zeta}{R/\alpha_0}\right) J_{|n\pm p|}^2(k\alpha_0\rho) \quad (10a)$$

When the condition $n-p=0$ is met, then the output beam is described by the zeroth-order Bessel function and has the following amplitude and intensity

$$U(\rho, \theta, z) = \frac{iA(\zeta)}{\sqrt{2\pi}} \exp\left[-ik\left(z + \frac{\rho^2}{2(z-\zeta)} - \frac{\alpha_0^2(z-\zeta)}{2}\right)\right] \exp[-i(2n+1)\pi/4] \text{circ}\left(\frac{z-\zeta}{R/\alpha_0}\right) J_0(k\alpha_0\rho) \quad (11)$$

$$I(\rho, \theta, z) = \frac{1}{2\pi} |A(\zeta)|^2 \text{circ}\left(\frac{z-\zeta}{R/\alpha_0}\right) J_0^2(k\alpha_0\rho) \quad (11a)$$

The vortex radius (defined as the radial position of the maximum intensity in the first bright ring surrounding the vortex core from the beam centre) is found from the intensity distribution, Eq. (10a), as

$$\rho_{\max} = j_{n\pm p,1} / (k\alpha_0), \quad (12)$$

where $j_{n\pm p,1}$ are the values of the Bessel function argument for which the first derivatives define their first maxima. So, they are found as roots of the equations $|J_{|n\pm p|+1}(k\alpha_0\rho)| = |J_{|n\pm p|-1}(k\alpha_0\rho)|$.

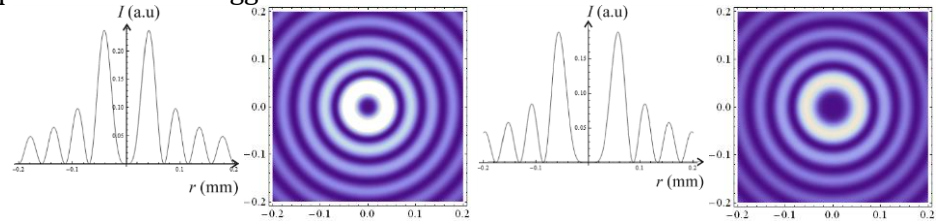
In case the output beam is with bright-axis, the radius of its central bright spot is defined by the position of the first minimum value of the Bessel function (i.e. the position of the first dark ring surrounding the central bright spot) from the beam centre

$$\rho_o = 2,4 / (k\alpha_0). \quad (13)$$

In Fig. 1 we present the radial (left side) and transverse (right side) intensity profiles of the diffracted beam for $n=1, p=1$ (a), $n=2, p=1$ (b), $n=2, p=-1$ (c), $n=2, p=-2$ (d) and $n=1, p=3$ (e). They are calculated for the following parameters: $n'=1,48$ (for $\lambda=980\text{nm}$) and $\gamma=1,35^\circ=0,024\text{rad}$ i.e. $\alpha_0=(n'-1)\gamma=0,012\text{rad}$, at distance $(z-\zeta)=10\text{cm}$. With r_{\max} and r_0 the radii of the vortex and of the central bright spot are denoted, respectively. When the TC n of the incident beam is increased, the TC of the output beam ($n+p$) is increased, which implies the increment of the vortex radius, also - this can be seen from Fig. 1 (a) and (b). The vortex radius can be increased in other way when increasing the TC of the SPP (compare Fig. 1 (a) and (e)). When the SPP has TC with smaller modulus and opposite sign compared to that of the incident beam, then the vortex radius of the diffracted beam is decreased due to the decrement of its TC - Fig. 1 (c).

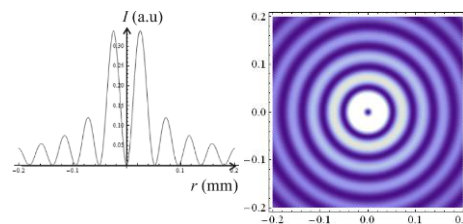
Finally, when $p=-n$, then one obtains a zeroth-order Bessel beam, shown in Fig. 1 (d).

In Fig. 2 we present the radial intensity distributions, calculated at distance $(z-\zeta)=10\text{cm}$, for twice bigger value of the parameter $\alpha_0=0,024\text{rad}$ ($\gamma=0,048\text{rad}$) than in Fig. 1, and for two different TCs of the incident BB and SPP: $n=1, p=1$ (a) and $n=2, p=-2$ (b). By making comparison of Fig. 1 (a) with Fig. 2 (a), and Fig. 1 (d) with Fig. 2 (b), one can conclude that the vortex radius is decreasing when increasing the value of the parameter α_0 , so does the radius of the central bright spot for the chargeless beam. Also, in the same radial interval there are more bright and dark rings when the parameter α_0 is bigger.

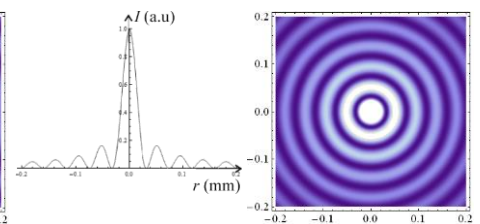


a) $n=1, p=1$ ($r_{\max}=0,04\text{mm}$)

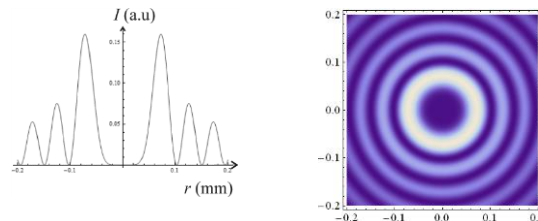
b) $n=2, p=1$ ($r_{\max}=0,058\text{mm}$)



c) $n=2, p=-1$ ($r_{\max}=0,025\text{mm}$)



d) $n=2, p=-2$ ($r_0=0,033\text{mm}$)



e) $n=1, p=3$ ($r_{\max}=0,07\text{mm}$)

Fig. 1. Radial intensity distributions for $\alpha_0=0,012\text{rad}$ and: $n=1, p=1$ (a), $n=2, p=1$ (b), $n=2, p=-1$ (c), $n=2, p=-2$ (d) and $n=1, p=3$ (e).

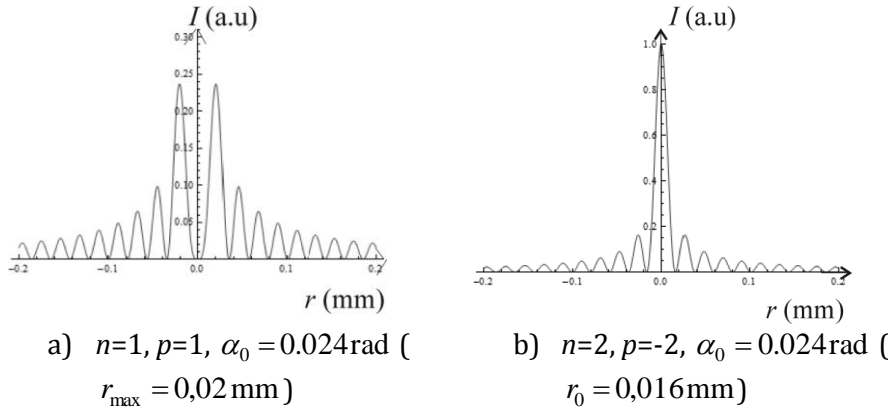


Fig. 2. Radial intensity distributions for $\alpha_0 = 0.024\text{rad}$ and: $n=1, p=1$ (a) and $n=2, p=-2$ (b).

In our previous work [17] the diffraction of non-obstructed Bessel beam by a fork-shaped grating is studied. It is well known that the field in the first diffraction orders of the fork-shaped grating is same to the diffracted field behind the SPP. Thus, if the BB was not obstructed by circular aperture, then behind the SPP the diffracted beam will have same amplitude as that in the first diffraction orders in [17]

$$U(\rho, \theta, z) = \left[\frac{-ik}{2(z-\zeta)} \right]^{(n\pm p)/2} \rho^{|n\pm p|} \exp \left[i(n\pm p) \left(\theta + \frac{\pi}{2} \right) \right] \left[\frac{kc^2(z-\zeta)}{2i} \right]^{n/2} \frac{1}{\Gamma(n\pm p+1)} \exp \left[-ik \left(z + \frac{\rho^2}{2(z-\zeta)} \right) \right] \\ \times \sum_{s=0}^{\infty} \frac{1}{s!} \frac{\Gamma(s+n+1\pm p/2)}{\Gamma(s+n+1)} \left[\frac{-kc^2(z-\zeta)}{2i} \right]^s {}_2F_1 \left(-s, -(n+s); n\pm p+1; \frac{\rho^2}{c^2(z-\zeta)^2} \right) \quad (14)$$

where $\Gamma(\dots)$ is Gamma function and ${}_2F_1(a, b; f; d)$ is the Gaussian hypergeometric function. One can see that this expression is more complicated than Eq. (10).

4. Conclusion

In this work we theoretically studied the transformation of the nondiverging Bessel beam (with or without phase singularity), which is transversally obstructed by a circular aperture, in the process of diffraction by the spiral phase plate with integer topological charge p . The expressions for the wave field amplitude and intensity are calculated by using the method of stationary phase. The output beam is Bessel beam with TC equal to the algebraic sum of the TCs of the incident beam and of the SPP. When the incident BB and the SPP have same in value but opposite in sign TCs, the output beam is chargeless, zeroth-order BB.

Further, expression for the propagation interval of the diffracted beam is obtained, as well as the expressions for the radii of the vortex (if the beam is high-order BB) and of the central bright spot (if the beam is zeroth-order BB). The intensity profiles for different values of the TCs of the incident beam and the SPP are numerically calculated. The analysis of the radial intensity distributions for two different values of the parameter α_0 (which is involved in the argument of the incident BB), show that by increasing this parameter one can achieve the narrower dark vortex spot (for high-order BB) and narrower bright spot (for zeroth-order BB).

The very small particles (having diameter of micrometer or smaller) with lower refractive index than that of the surrounding medium can be caught in the dark regions between the bright rings, while the particles with higher refractive index than that of the surrounding medium are caught in the bright rings. The Bessel beam with phase singularity possesses orbital angular momentum, which can be transferred to the trapped particles in optical tweezers experiments. In the dark core of the high-order BB atoms can be trapped and transported an extended distance without transverse spreading. Also, the BBs have applications in industry for precise machine cutting and fabrication of 3D structures using multiphoton polymerization, then in optical communications, statistical physics (for studying how particles with inherent Brownian motion act in external potential) and many others [18, 19].

References

- [1] J. Durnin, "Exact solutions for nondiffracting beams. I. The scalar theory", *J. Opt. Soc. Am. A* 4 (1987) 651-654.
- [2] J. Durnin, J. J. Miceli, Jr. and J. H. Eberly, "Diffraction-free beams", *Phys. Rev. Lett.* 58 (1987) 1499- 1501.
- [3] J. Durnin, J. J. Miceli and J. H. Eberly, Reply, *Phys. Rev. Lett.* 66 (1991) 838.
- [4] R. M. Herman and T. A. Wiggins, "Production and uses of diffractionless beams", *J. Opt. Soc. Am. A* 8 (1991) 932-942.
- [5] J. Turunen, A. Vasara and A. T. Friberg, "Holographic generation of diffraction-free beams", *Appl. Opt.* 27 (1988) 3959-3962.
- [6] A. Vasara, J. Turunen and A. T. Friberg, "Realization of general nondiffracting beams with computer-generated holograms", *J. Opt. Soc. Am. A* 6 (1989) 1748-1754.
- [7] S. N. Khonina, V. V. Kotlyar, M. V. Shinkaryev, V. A. Soifer and G. V. Uspleniev, "The phase rotor filter", *J. Mod. Opt.* 39 (1992) 1147-1154.
- [8] M. W. Beijersbergen, R. P. C. Coerwinkel, M. Kristensen and J. P. Woerdman, "Helical-wavefront laser beams produced with a spiral phaseplate", *Opt. Commun.* 112 (1994) 321-327.
- [9] V. V. Kotlyar, A. A. Almazov, S. N. Khonina, V. A. Soifer, H. Elfstrom and J. Turunen, "Generation of phase singularity through diffracting a plane or Gaussian beam by a spiral phase plate", *J. Opt. Soc. Am. A* 22 (2005) 849-861.
- [10] J. Arlt and K. Dholakia, "Generation of high-order Bessel beams by use of an axicon", *Opt. Comm.* 177 (2000) 297-301.

- [11] S. Topuzoski and Lj. Janicijevic, "Conversion of high order Laguerre-Gaussian beams into Bessel beams of increased, reduced or zero-th order by use of a helical axicon", *Opt. Commun.* 282 (2009) 3426-3432.
- [12] S. N. Khonina, V. V. Kotlyar, V. A. Soifer, M. V. Shinkaryev and G. V. Uspleniev, "Trochoson," *Opt. Commun.* 91 (1992) 158-162.
- [13] M. Born, and E. Wolf, *Principles of Optics* (Cambridge, University Press, 1999).
- [14] H. Bateman and A. Erdelyi, *Higher Transcendental Functions II* (Nauka, Moscow, 1974).
- [15] M. Abramowitz and I. A. Stegun, *Handbook of Mathematical Functions* (Dover, New York, 1964).
- [16] C. Paterson and R. Smith, "Higher-order Bessel waves produced by axicon-type computer-generated holograms", *Opt. Commun.* 124 (1996) 121-130.
- [17] Lj. Janicijevic and S. Topuzoski, "Diffraction of nondiverging Bessel beams by fork-shaped and rectilinear grating", in *Proceedings of the Sixth International Conference of the Balkan Physical Union (American Institute of Physics, Vol. 899, 2007)* 333-334.
- [18] D. McGloin and K. Dholakia, "Bessel beams: diffraction in a new light", *Contemp. Phys.* 46 (2005) 15-28.
- [19] M. Duocastella and C. B. Arnold, "Bessel and annular beams for materials processing", *Laser Photonics Rev.* 6 (2012) 607-621.

An overview on local structure and magnetism of Fe-C nanocomposites

S.G. Greculeasa¹, F. Dumitrache², I. I. Lungu², N. Iacob¹, V. Kuncser¹

¹ *National Institute of Materials Physics, Atomistilor 405A, 077125, Magurele, Ilfov, Romania*

² *National Institute for Laser, Plasma and Radiation Physics, P.O. Box MG-36, 077125, Magurele, Romania*

Corresponding author: kuncser@infim.ro

Abstract

Core-shell iron-based nanoparticles have a great attraction in biomedicine, sensors, catalysis etc. due to outstanding structural and magnetic properties. This review presents an updated outlook on the local configurations and magnetic properties of novel Fe-C composite core-shell nanoparticles. The specificities of a large number of preparation and processing techniques were addressed, but main results were presented on those systems prepared by laser pyrolysis. Obstacles in obtaining a good control of magnetic properties, such as oxide phases, very broad size distributions, phase intermixing at the core-shell interface, or insufficient relative Fe content were brought to spotlight and ways to surmount them were proposed. Magnetic relaxation phenomena specific to these types of small complex nanoparticulate systems were approached.

Keywords: core-shell, local configurations, magnetic relaxation, interface, Mössbauer spectroscopy, magnetometry

1. Introduction

Core-shell iron based magnetic nanoparticles are exceptional nanostructures with important size induced effects, e.g. with tunable coercivity with respect to bulk, as well as with superparamagnetic behaviour for reduced particle sizes. Therefore, they are attracting much interest in advanced applications: biomedicine such as MRI or hyperthermia or cytotoxicity tests [1-5], catalysis [6,7], microwave absorption [8-10], magnetic separation of biomolecules [11], magneto-optical devices, magnetic recording systems, sensors, ion batteries [12], hydrogen storage, carbon nanotube grow [13], water treatment [14].

However, nanoparticles of metallic Fe have low stability in air, water, acid or base environment or at high temperatures due to oxidation, agglomeration and corrosion, causing a high impact on magnetic properties and limiting their advantages. To note the importance of preserving the metallic character of the particles due to the corresponding increased magnetization with respect to the oxide counterparts. In this regard, protective shells (organic coatings or inorganic layers) are a viable approach to chemically stabilize the Fe nanoparticles from oxidation, thermal or temporary degradation. Carbon or carbon-based phases [15-17], carbon and organic matrix such as polyaniline [18], polypyrrole [8] and polystyrene [19], oxides as silica [20], metals with low oxidation degree such as Au [21] can be used as protective shells. Generally, core-shells nanoparticles are considerably improved in many regards relative to the corresponding single components but care has to be paid to the optimization of the shell in order to preserve the magnetic properties of the nanoparticles (thicker shells will reduce the magnetization of the overall system whereas thinner shells might not be effective against oxidation). By using carbon as a protective shell it becomes possible not only to prevent oxidation but also to improve the anti-agglomeration behaviour of the nanoparticles because of the magnetic coupling reduction. Compared to organic matrix, oxides or metals, carbon layers have better chemical and thermal stability, conductivity, electrocatalytic activity and biocompatibility, lower density, favour chemical functionalization, are abundant and cost-effective (especially when compared to noble metals).

In this review, a few advanced preparation methods will be presented, along with the corresponding specific geometries of the obtained nanostructures with a main focus on nanoparticulate Fe-C systems obtained by laser pyrolysis. Main issues related to such Fe-C nanoparticles will be addressed, especially the presence of unwanted oxide phases and phase mixture at the core-shell interface. Tools to improve magnetic properties, as well as aspects regarding magnetic relaxation phenomena in Fe-C nanosystems obtained by laser pyrolysis are detailed.

2. Preparation and processing of Fe-C composite nanostructures

The production of Fe-based magnetic nanoparticles encapsulated by carbon is performed by complex processes and special precursors are required. This procedure is challenging due to the highest saturation magnetization of Fe among all the other magnetic materials. The most used processing methods for achieving this aim are: arc discharge, pulsed plasma discharge, carbon arc route, hydrothermal route, radio frequency thermal plasma reaction method, template reduction, solution combustion synthesis, chemical vapor deposition, reduction and carbonization, simultaneous reduction/pyrolysis, laser pyrolysis.

The simple and cost-effective arc discharge method was used to prepare carbon-coated iron nanoparticles of spherical shape and sizes in the 40-55 nm range (graphitic shells of 20-30 nm) [22,23], as well as in the 4-45 nm range [24,25]. Fe-C nanoparticles obtained by pulsed plasma discharge in a liquid [4] showed low cytotoxicity. Further on, Fe-C nanocapsules prepared by arc discharge were embedded in polypyrrole-paraffin (see figure 1) by *in situ* oxidative polymerization method [8], with superior microwave absorption properties. Fe-C nanoparticles prepared by carbon arc route showed good cytotoxic results [2].

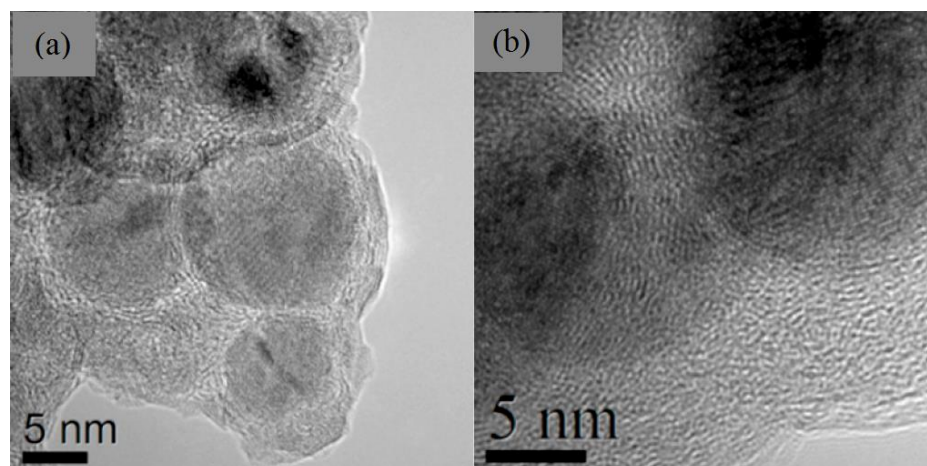


Figure 1. HRTEM images of Fe-C nanostructures (a) and Fe/C/PPy composites (b). Reprinted (adapted) with permission from [8]. Copyright © 2016 American Chemical Society.

The hydrothermal route followed by an annealing temperature in argon at temperatures between 400 and 600°C [26] was used to prepare composites of magnetite nanoparticles and carbon nanocapsules (Fe_3O_4 -CNCs), γ - Fe_2O_3 -CNCs, and Fe-C nanostructures. At the highest annealing temperature (see figure 2), the oxidation is completely removed. The hydrothermal method was followed by a thermal reduction process also in [27]. Oxides were successfully removed by annealing in a mixture gas of hydrogen and argon at 550°C. Moreover, in order to remove the non-encapsulated Fe nanoparticles and to improve dispersion, acid treatment was applied. However, the magnetic properties were considerably damaged. In other study [28], acid treatment was used to generate carboxylic groups on the graphite shell for further functionalization, but increase of defects was detected, which is expected to alter magnetic properties. The stabilization in aqueous suspensions of Fe nanoparticles encapsulated in C (coated with polyvinyl-alcohol) was succeeded by Aguilo-Aguayo *et al.* [1] using a modified arc-discharge plasma method.

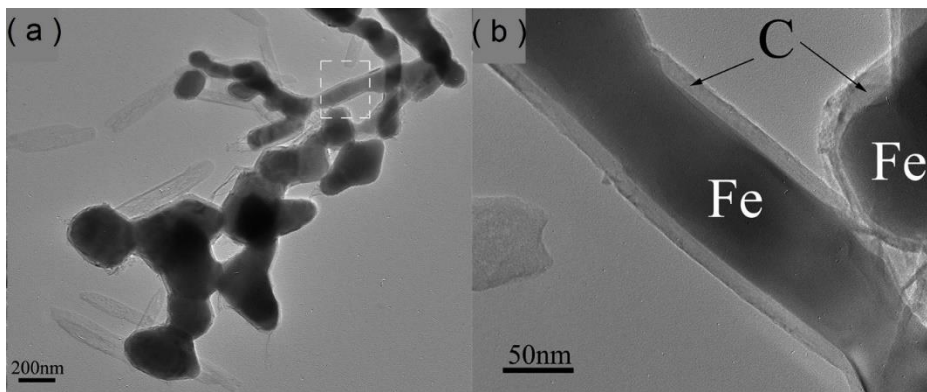


Figure 2. TEM images of Fe-C nanostructures and hollow CNCs. Reprinted (adapted) with permission from [26]. Copyright 2011 American Chemical Society.

Iron nanoparticles encapsulated in C were prepared by Bystrzejewski *et al.* by a flow-through radio frequency thermal plasma reaction method [29]. A purification process (based on HCl and ethanol) was necessary to remove Fe nanoparticles not encapsulated (which would modify the magnetic properties) and small Fe-C nanostructures were obtained (although having a broad diameter distribution between 10 and 100 nm).

Composites of Fe/Fe₃C-C were also obtained by a green template reduction method [12], using α -FeOOH templates, glucose and urea (reducing and chelating agents), annealed at 800°C. A template free method was used to prepare mesoporous structures of graphite encapsulated iron based nanostructures (Fe₃C/Fe nanosheet composites), called solution combustion synthesis [7]. Starting materials were dissolved in deionized water and carbonized in Ar at moderate and high temperatures. The Fe based nanostructures encapsulated in C were successfully prepared without templates.

Radio frequency-catalytic chemical vapor deposition was used to prepare Fe-C core shell nanostructures (and other elements) [3], followed by annealing in H₂ atmosphere up to 800°C and acid treatment.

Magnetic nanoparticles (Fe and Fe₃O₄) in a carbon matrix were prepared by reduction/pyrolysis of Fe³⁺ dispersed in sucrose [30]. Basically, Fe³⁺ ions were impregnated in sucrose, followed by pyrolysis at temperatures in the range 400 – 800°C. Fe-C core shell particles assembled in nanocubes were prepared by the hydrothermal method and pyrolysed in N₂ [10].

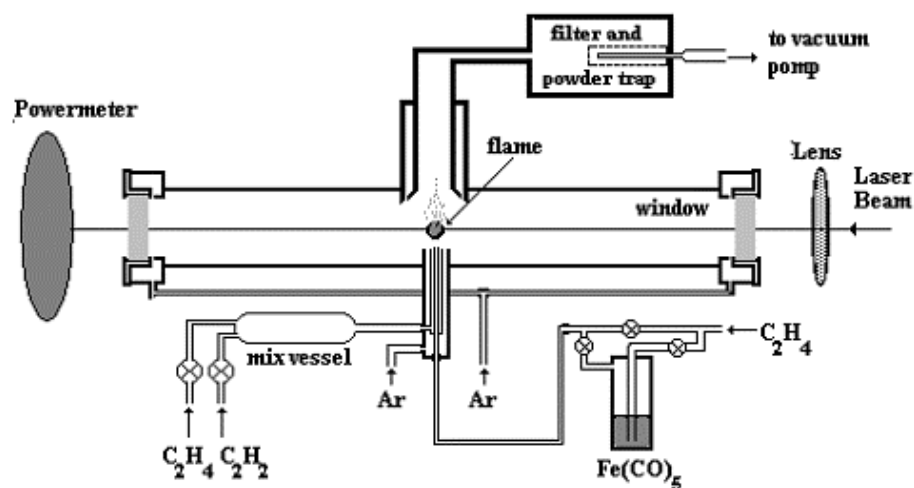


Figure 3. Schematic representation of the laser pyrolysis synthesis technique

Remarkable results were obtained using a preparation method called laser pyrolysis that combines the fast heating of gas phase processes with the sudden quenching of reaction products. It is a one step synthesis method that allows the control of structural and magnetic properties by carefully tuning the preparation parameters. In order to prepare C coated Fe core-shell nanoparticles, precursors such as iron pentacarbonyl vapors, as iron donor, and an ethylene/acetylene mixture [31,32] as carbon source are introduced in a flow reactor through a central nozzle system with three concentric tubes (see figure 3). The reactive mixture flows are confined using an Ar flow (from 1500 to 2500 sccm) emerging through the external tubes. A secondary Ar flow (300sccm) was admitted from the nozzles placed near by both IR-windows in order to avoid some particle deposition on them. A CO₂ laser beam with 100W nominal power is focused on the reaction area generating a pyrolytic flame. The structural and magnetic properties of the Fe-C nanocomposites can be improved by optimizing the initial parameters of the preparation, such as the nozzle diameter controlling the gas flow [15,17] and the precursor type and content [15,16,31]. Mean particle size, Fe/C ratio and saturation magnetization increase with nozzle diameter [17]. In [16], the C₂H₂/C₂H₄ carbon source mixture was optimized at 50% to balance an increased Fe content and the protective behaviour of the C shell.

3. Tuning magnetic properties

The magnetic properties of Fe-C nanostructures depend strongly on the size of the nanoparticles, iron content and phase composition, oxidation state and quality of the core-shell interface. All these parameters can be

controlled either by specific parameters of the laser pyrolysis or of alternative methods, or by parameters of further processing procedures as well, one of the most important being the temperature.

3.1. Size

One of the most imperative challenges in the design of magnetic properties of Fe-C nanostructures is the ability to control their size, namely their size distribution. In this respect, intensive efforts have been done to find optimal processing parameters leading to a desired average size in condition of an as much as narrower size distribution. The size of the nanoparticles dictates the magnetic behaviour which can be at a given temperature, either superparamagnetic or ferromagnetic (magnetic frozen). The entire magnetic response of the nanoparticles of interest for most applications is therefore imposed by these parameters. Depending on the involved anisotropy, very small particles (with less than 10 nm for the Fe core) may possess superparamagnetic behaviour [17]. More details on superparamagnetism are given in [section 5](#).

3.2. Oxidation

In order to achieve high saturation magnetization (M_s) of Fe-based nanoparticles, valence state is important and the metallic character of the core needs to be preserved. Even using a protective shell such as carbon, issues related to the uncovered Fe nanoparticles (due to non-uniform coverage) subject to oxidation and degradation still remain. Therefore, oxidation is a serious concern since it considerably modifies the magnetic performance. For example, metallic Fe-C nanostructures have presented high M_s values, up to 90 emu/g, while values less than half were reported for their oxide counterparts – composites of Fe_3O_4 / $\gamma\text{-Fe}_2\text{O}_3$ and carbon nanocapsules [26].

One of the few powerful techniques that can be used to precisely discriminate between different Fe phases (always appearing in such particulate Fe-C nanocomposites) is Mössbauer spectroscopy. Some examples of Mössbauer analysis of C coated Fe nanoparticles are found in [17]. At room temperature, one of the reported samples was composed of phases in which spectral components were completely collapsed due to superparamagnetic relaxation of Fe oxides (see [section 4](#)). Other reported samples (which was obtained within different conditions of pyrolysis) contained both metallic (Fe and carbide) and oxidised Fe phases. This is just a typical example proving that C encapsulation may succeed only partially and oxidation can not be completely avoided. It is a challenging matter of interest to find suitable tools to separate the Fe core-C shell nanoparticles from their C matrix and Fe oxide counterpart.

3.3. Fe-C interface and C/Fe ratio

The protective performances of carbon coatings depend on their structural integrity. However, it is difficult to obtain a clear interface between the core and the shell and carbide phases – mostly Fe_3C but also other phases such as Fe_7C_3 and Fe_5C_2 [15-17;30] can be also formed. Even hybrid nanostructures containing iron and carbon based might be subjected to oxidation issues. The formation of Fe-C phases is affecting the protective behaviour of the shells and the overall magnetic properties of the structures.

Examples of Mössbauer spectra of Fe-C nanocomposites containing 1% and 8%wt iron and obtained by sucrose pyrolysis at different temperatures are shown in figure 4 [30]. The Fe_3C phase is not formed at temperatures lower than 800°C. The processing temperature needs to be high enough to allow formation of the α -Fe phase, but lower to prevent Fe-C intermixing. In this case, the optimal temperature for the sample containing 8% iron is 600°C.

It was found that Fe is encapsulated preferentially at low C/Fe ratio [29]. For higher carbon content, the encapsulation yield decreases. In the Fe-C nanostructures, presented in figure 4 [30], the phase composition and content are influenced considerably by the pyrolysis temperature and Fe content. The processing temperature has a considerable impact on the Fe valence, phase formation and, consequently, magnetism of the final product. The materials processed at 400°C show no sign of metallic Fe, but only oxides in magnetic and superparamagnetic states. When increasing the processing temperature at 600°C, α -Fe starts to form in the sample of higher Fe content. At 800°C the oxidation is considerably reduced in favour of metallic Fe and carbide. High iron content encourages the formation of metallic phases of magnetic character (Fe and Fe_3C as well), especially at higher pyrolysis temperature. In accordance with the local structure, there is a monotonic correlation (linear in some cases [29]) between the iron content and saturation magnetization values in Fe-C nanostructures.

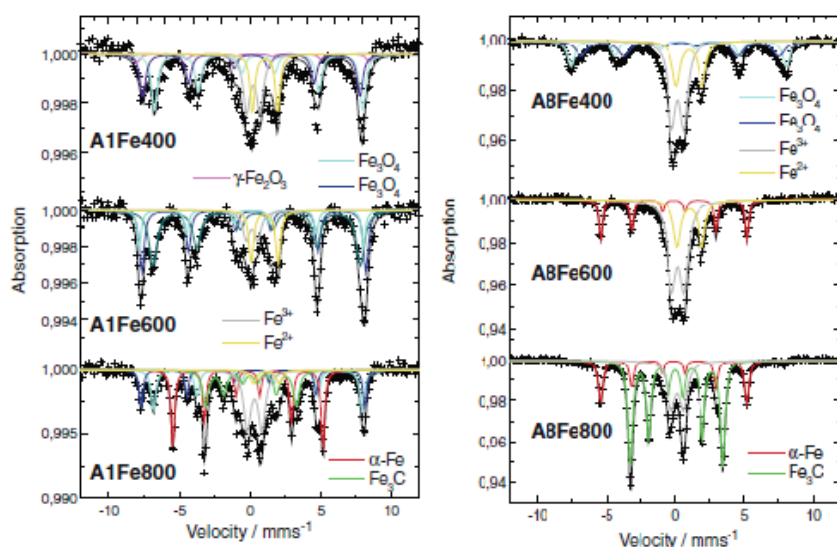


Figure 4 Room temperature Mössbauer spectra of Fe-C nanocomposites containing 1% (left) and 8% (right) iron obtained after sucrose pyrolysis at 400, 600 and 800°C. Reprinted (adapted) with permission from [30]. Copyright Springer Science+Business Media B.V. 2011.

4. Preparation temperature and processing

Magnetic and morphological parameters of Fe-C nanoparticulate systems obtained in different conditions are mentioned in Table 1. In the special case of laser pyrolysis, the higher the temperature of the preparation method or of the successive thermal annealing treatment, the higher the saturation magnetization is obtained, as depicted in Table 1. However, post processing such as acid treatment is very detrimental to the saturation magnetization (as evidenced in figure 5) in favour of the coercivity.

Table 1 Magnetic parameters of Fe-C nanostructures for different preparation and processing conditions

| Sample | Preparation method | Treatment | Fe NP size (nm) | M_s (emu/g) | H_c (Oe) | Source |
|-----------------|-------------------------------------|--|-----------------|---------------|------------|--------|
| Fe-C core-shell | hydrothermal | TA in H ₂ -Ar, 550°C, 3h | 10 - 20 | 47.3 | 75 | [6] |
| | | TA in H ₂ -Ar, 550°C, 3h; HCl | 10 - 20 | 0.015 | 639 | |
| Mesoporous Fe/C | hydrothermal, carbothermic reaction | TA in Ar 900°C, 3h | 5.1 | 16.3 | 560 | [9] |
| Fe-C core-shell | arc discharge | - | 50 | 34.8 | 221 | [23] |

| Sample | Preparation method | Treatment | Fe NP size (nm) | M _s (emu/g) | H _c (Oe) | Source |
|-------------------|---|---------------------------------------|-----------------|------------------------|---------------------|--------|
| Fe-C nanocapsules | arc discharge | TA in air 800°C, 3.5h | 6-40 | 85 | 397 | [24] |
| Fe-C core-shell | RF-cCVD | TA in H ₂ , 800°C, 3h; HCl | 7-15 | 10 | | [3] |
| Fe-C core-shell | hydrothermal, pyrolysis in N ₂ (600°C, 650°C, and 700°C) | - | 3-100 | 106-121 | 338-440 | [10] |
| Fe-C | pulsed plasma in liquid | - | <7.9> | 12 | 480 | [4] |
| Fe-C core-shell | Laser pyrolysis T= 635°C | - | <3.9> | 28.4 | - | [17] |
| | Laser pyrolysis T= 645°C | - | <5.7> | 37.2 | - | |
| | Laser pyrolysis T= 665°C | - | <6.4> | 58.9 | 54 | |
| | Laser pyrolysis T= 675°C | - | <10.5> | 65.9 | 46 | |

* TA = thermal annealing treatment

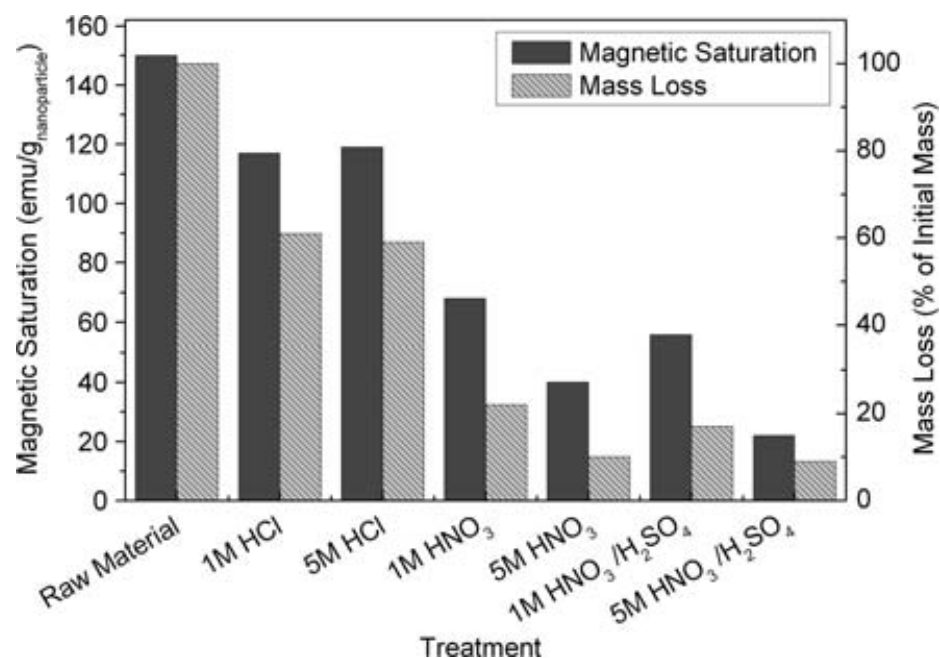


Figure 5 The mass loss of the carbon-encapsulated Fe nanoparticles and corresponding magnetic saturation after treatments under acidic conditions. The Fe nanoparticles were treated at 120°C for 15 minutes. Reprinted with permission from [28]. Copyright Springer Science+Business Media B.V. 2009.

5. Magnetic relaxation phenomena

The magnetization can be easily flipped by thermal fluctuations over the anisotropy energy barrier of very small ferro/ferri-magnetic nanoparticles which will enter in these conditions (enough higher temperature with respect to the anisotropy) the so-called superparamagnetic regime. The moments of the particles can fluctuate as the temperature increases, within the Néel relaxation time, τ , given by:

$$\tau = \tau_0 \exp\left(\frac{KV}{k_B T}\right) \quad (1)$$

where τ_0 is the attempt time (characteristic of a material), K is the anisotropy constant, V is the volume of the nanoparticle and k_B is the Boltzmann's constant.

The blocking temperature, T_B , is the temperature at which the relaxation time matches the timescale of the measuring technique, τ_M :

$$T_B = \frac{KV}{k_B \ln(\tau_M/\tau_0)} \quad (2)$$

Below T_B the particles are called to be in a blocked state, while above T_B the particles are fluctuating. Size is very influential and particles having a broad size distribution will be blocked at different T_B . The blocking temperature is also highly dependent on the measuring method. Magnetic relaxation phenomena can be evidenced in magnetic measurements, temperature dependent Mössbauer spectroscopy measurements, as well as neutron scattering and muon spin spectroscopy. In magnetic measurements, T_B can be easily deduced from the zero-field-cooled field-cooled procedure or from the coercive field dependence of temperature, which for non-interacting nanoparticles approaching the superparamagnetic regime should respect the relationship:

$$H_C = H_0 \left(1 - \sqrt{\frac{T}{T_B}}\right) \quad (3)$$

where H_0 is the coercive field at 0 K (approximated with the coercive field at the lowest temperature).

In Mössbauer spectroscopy measurements, in the regime of collective excitations specific to temperatures much lower than T_B , the hyperfine magnetic field, B_{hf} , decreases by the following relation:

$$B_{hf} = B_0 \left(1 - \frac{k_B T}{2KV}\right) \quad (4)$$

where B_0 is the hyperfine magnetic field at the lowest temperature.

The anisotropy barrier energy KV can be obtained from eq. (4). Further on, the average size of the nanoparticles can be deduced by considering the anisotropy constant from magnetic measurements. The blocking temperature specific to the Mössbauer spectroscopy technique may be easily obtained from eq. (2).

The Mössbauer spectra of very small Fe-C nanocomposites (few nm) containing Fe oxides, Fe carbides and metallic Fe, were reported in

[15]. The probability distribution of the magnetic hyperfine field is shown on the right side of each corresponding spectrum. All three contributions present a magnetic relaxation behavior. The outer sextet (highest hyperfine magnetic field) collapses below 80 K, suggesting a blocking temperature between 40 and 80 K. The temperature evolution of the hyperfine magnetic field indicates a relaxation mechanism of collective excitations for Fe and Fe carbide phases, while the steep decrease corresponding to the Fe oxide is related to the superparamagnetic transition. A wide range of blocking temperatures was derived from the magnetic measurements for the investigated samples – between 390 and 670 K.

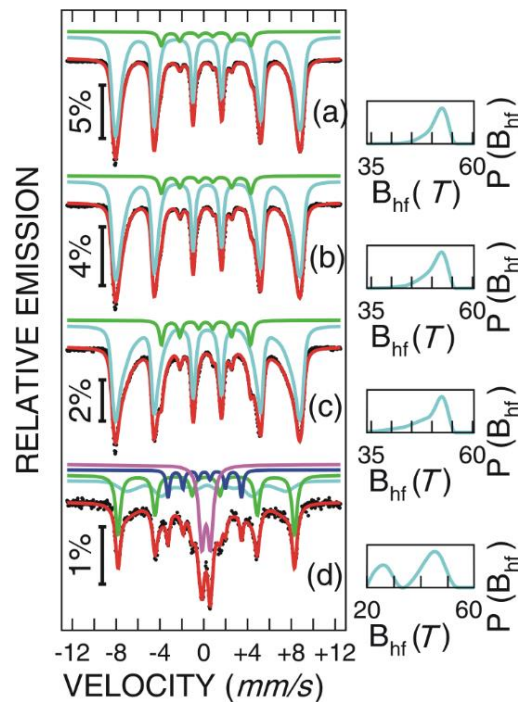


Figure 6 Mössbauer spectra of the sample A collected at 4.5 K (a), 25 K (b), 50 K (c), and RT (d).

Magnetic relaxation phenomena can be also evidenced in the Mössbauer spectra of a Fe-C composite sample denoted as A (prepared by laser pyrolysis), collected at temperatures from 4.5 K to room temperature (RT), presented in [figure 6](#). The spectra collected at low temperatures present a relatively wide sextet pattern and are mainly fitted using the probability distribution method. On the other hand, the spectrum collected at room temperature shows narrower patterns and was fitted by a superposition of discrete and distributed sub-spectra. The probability distribution of hyperfine magnetic fields is shown on the right side of each corresponding spectrum. The main hyperfine parameters (isomer shift, IS,

quadrupole splitting, QS, and magnetic hyperfine field, B_{Hf}), as well as relative area and phase composition, are given in [Table 2](#).

The Mössbauer spectra at low temperatures (< 50 K) of sample A ([figure 6](#)) are showing a main wide magnetic pattern attributed to iron oxide phases (maghemite or magnetite, or mixtures in distorted configuration). A secondary, less intense magnetic phase is assigned to iron carbide, with an average hyperfine magnetic field of about 25.4 T and isomer shift of 0.3 mm/s. To note that no traces of metallic Fe were observed in the Mossbauer spectrum of low temperature, and therefore iron carbide monophasic nanoparticles (with no Fe core/Fe-C shell) are formed. At room temperature (RT), maghemite/magnetite phases are still prevailing, corresponding to a well-formed crystalline sextet (S1), which accounts for large size nanoparticles with a blocking temperature much higher than room temperature. Also, a wide distribution of hyperfine magnetic fields (S_DIST) with two maxima at 26 T and 45 T accounts for maghemite/magnetite phases in distorted configurations of two different average sizes. In addition, a paramagnetic doublet (D, having a contribution of 27% to the spectrum) was considered, as belonging to Fe oxides in the superparamagnetic relaxation regime specific to very fine nanoparticles. Whereas all data concerning the Fe oxide nanoparticles support a very large size distribution (e.g. trilobar like), the Fe carbide nanoparticles presents a much narrower size distribution. At room temperature, the iron carbide phase is precisely identified as cementite, Fe_3C , with hyperfine parameters in accordance with Ref. [\[33\]](#).

Table 2 Hyperfine parameters (isomer shift, IS, quadrupole splitting, QS, magnetic hyperfine field, B_{Hf}) and spectral relative area (corresponding to magnetite/maghemite and cementatite phases, as discussed in the text) derived from the Mössbauer spectra of sample A at various temperatures.

| T (K) | Sublattice | IS (mm/s) | QS (mm/s) | B_{hf} (T) | R_A (%) |
|-------|------------|-----------|-----------|---------------------|-----------|
| 4.5 | S_DIST | 0.31 | 0.03 | 51.2 | 92 |
| | S | 0.3 | 0.04 | 25.4 | 8 |
| 25 | S_DIST | 0.37 | 0.03 | 50.6 | 91 |
| | S | 0.3 | 0.04 | 25.3 | 9 |
| 50 | S_DIST | 0.4 | 0.03 | 49.3 | 90 |
| | S | 0.3 | 0.03 | 25.2 | 10 |
| RT | S_DIST | 0.37 | -0.05 | - | 27 |
| | S1 | 0.33 | 0.02 | 50 | 35 |
| | S2 | 0.17 | 0.05 | 20.8 | 11 |
| | D | 0.32 | 0.78 | - | 27 |

In [figure 7](#) (left side), the evolution of the hyperfine magnetic field values (averaged for distributions) of each magnetic contribution is shown.

Also, the reduced hyperfine magnetic field values related to the hyperfine magnetic field at the lowest temperature, are shown in figure 7 (right side). Using eq. (4), the barrier energy KV can be obtained and the related values are: $4 * 10^{-20}$ J (Fe_3C) and $8.77 * 10^{-20}$ J ($\gamma\text{-Fe}_2\text{O}_3 / \text{Fe}_3\text{O}_4$).

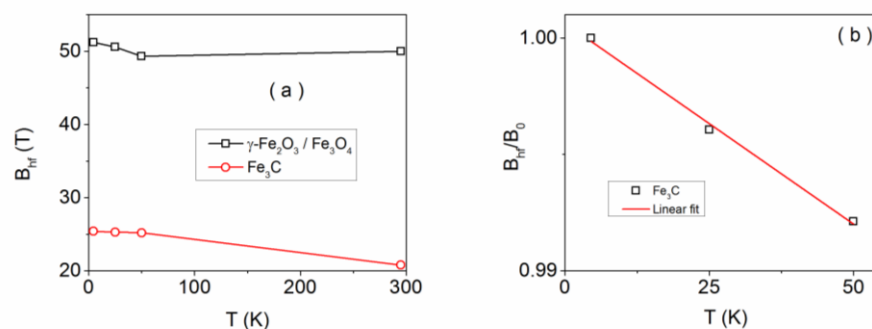


Figure 7 Temperature dependence of the average hyperfine magnetic field (all magnetic contributions) (a) and of the reduced average hyperfine magnetic field (B_{hf}/B_0) (only Fe-C phases) (b).

6. Concluding remarks and outlook

In summary, we have reviewed recent progress regarding C covered Fe nanoparticles, with use in various fields such as biomedicine, catalysis, microwave devices and sensors. Recent progresses in the preparation and processing techniques used for C encapsulated Fe nanoparticles are discussed. Issues related to the oxidation problem, core-shell interface, C/Fe ratio and control of magnetic properties are referred and methods to overcome the challenges regarding the optimization of the magnetic properties for different applications are proposed. Magnetic relaxation phenomena are detailed in relation to several experimental techniques, with the main focus on Fe-C nanoparticulate systems obtained by laser pyrolysis. Future work on the core-shell Fe-based nanoparticles should focus on controlling the size and composition of the nanoparticles in order to obtain high magnetic performances.

Acknowledgements: This work was supported by the Romanian Ministry of Research and Innovation through projects PN-III-P1-1.2-PCCDI-2017-0871 and the Core Program PN19-03 (contract no. 21 N/08.02.2019 at NIMP and 16 N /08.02.2019 at NILPRP).

References

[1] N. Aguiló-Aguayo, L. Maurizi, S. Galmarini, M.G. Ollivier-Beuzelin, G. Coullerez, E. Bertrana, H. Hofmann, Dalton Trans. 43 (2014) 13764.

- [2] I.P. Grudzinski, M. Bystrzejewski, M.A. Cywinska, A. Kosmider, M. Poplawska, A. Cieszanowski, Z. Fijalek, A. Ostrowska, *Colloids and Surfaces B: Biointerfaces* 117 (2014) 135–143.
- [3] Y. Xu, M. Mahmood, A. Fejleh, Z. Li, F. Watanabe, S. Trigwell, R.B. Little, V.P. Kunets, E. Dervishi, A.R. Biris, G.J. Salamo, A.S. Biris, *Int J Nanomedicine* 5 (2010) 167–176.
- [4] Z. Abdullaeva, E. Omurzak, C. Iwamoto, H.S. Ganapathy, S. Sulaimankulova, C. Liliang, T. Mashimo, *Carbon* 50 (2012) 1776–1785.
- [5] X. Fang, X. Cheng, Y. Zhang, L.G. Zhang, M. Keidar, *J Colloid Interface Sci* 509 (2018) 414–421.
- [6] J. Xue, H. Xiang, K. Wang, X. Zhang, S. Wang, X. Wang, H. Cao, *J Mater Sci* 47 (2012) 1737–1744.
- [7] Z. Cao, M. Qin, C. Zuo, Y. Gu, B. Jia, *J Colloid Interface Sci* 491 (2017) 55–63.
- [8] L. Jiang, Z. Wang, D. Geng, Y. Wang, J. An, J. He, D. Li, W. Liu, Z. Zhang, *J. Phys. Chem. C* 120 (2016) 28320–28329.
- [9] G. Li, L. Wang, W. Li, Y. Xu, *Microporous Mesoporous Mater* 211 (2015) 97–104.
- [10] R. Qiang, Y. Du, H. Zhao, Y. Wang, C. Tian, Z. Li, X. Han, P. Xu, *J. Mater. Chem. A* 3 (2015) 13426.
- [11] L.A. Arce-Saldaña, E. Espinoza-Mosso, B. Castro-Rodríguez, A. Portillo-López, F. Muñoz-Muñoz, D. Dominguez, M.H. Farías, G. Soto, *Advanced Powder Technology* 29 (2018) 1035–1041.
- [12] L. Su, Z. Zhou, P. Shen, *Electrochimica Acta* 87 (2013) 180–185.
- [13] C.T. Fleaca, I. Morjan, R. Alexandrescu, F. Dumitrache, I. Soare, L. Gavrilă-Florescu, F. Le Normand, A. Derory, *Appl Surf Sci* 255 (2009) 5386–5390.
- [14] C.T. Yavuz, J.T. Mayo, W.W. Yu, A. Prakash, J.C. Falkner, S. Yean, L. Cong, H.J. Shipley, A. Kan, M. Tomson, D. Natelson, V.L. Colvin, *Science* 314 (2006) 964–967.
- [15] G. Schinteie, V. Kuncser, P. Palade, F. Dumitrache, R. Alexandrescu, I. Morjan, G. Filoti, *J Alloy Compound* 564 (2013) 27–34.
- [16] F. Dumitrache, I. Morjan, C. Fleaca, R. Birjega, E. Vasile, V. Kuncser, R. Alexandrescu, *Appl Surf Sci* 257 (2011) 5265–5269.
- [17] I. Morjan, F. Dumitrache, R. Alexandrescu, C. Fleaca, R. Birjega, C.R. Luculescu, I. Soare, E. Dutu, G. Filoti, V. Kuncser, G. Prodan, N.C. Popa, L. Vékás, *Advanced Powder Technology* 23 (2012) 88–96.
- [18] C.T. Fleaca, F. Dumitrache, I. Morjan, A.-M. Niculescu, I. Sandu, A. Ilie, I. Stamatina, A. Iordache, E. Vasile, G. Prodan, *Applied Surface Science* 374 (2016) 213–221.
- [19] Z. Qian, Z. Zhang, Y.J. Chen, *Colloid Interface Sci.* 327 (2008) 354.
- [20] M. Stjerndahl, M. Andersson, H.E. Hall, D.M. Pajerowski, M.W. Meisel, R.S. Duran, *Langmuir* 24 (2008) 3532.
- [21] F. Bao, J. Yao, R. Gu, *Langmuir* 25 (2009) 10782.
- [22] J.S. Qiu, Y.F. Li, Y.P. Wang, Y.L. An, Z.B. Zhao, Y. Zhou, W. Li, *Fuel* 86 (2004) 267–274.
- [23] O. Khani, M.Z. Shoushtari, M. Farbod, *Physica B* 477 (2015) 33–39.
- [24] P.-Z. Si, Z.-D. Zhang, D.-Y. Geng, C.-Y. You, X.-G. Zhao, W.-S. Zhang, *Carbon* 41 (2003) 247–251.
- [25] R. Hu, T. Furukawa, X. Wang, M. Nagatsu, *Appl Surf Sci* 416 (2017) 731–741.
- [26] P. Wu, N. Du, H. Zhang, J. Yu, D. Yang, *J. Phys. Chem. C* 115 (2011) 3612–3620.
- [27] C. Cao, Z. Ma, C. Ma, W. Pan, Q. Liu, J. Wang, *Mater Lett* 88 (2012) 61–64.

- [28] A. Taylor, Y. Krupskaya, S. Costa, S. Oswald, K. Krmer, S. Fssel, R. Klingeler, B. Bchner, E. Borowiak-Palen, M. Wirth, J. Nanopart. Res. 12 (2010) 513–519.
- [29] M. Bystrzejewski, Z. Karoly, J. Szepvolgyi, A. Huczko, H. Lange, Mater Res Bulletin 46 (2011) 2408–2417.
- [30] F.G. Mendonça, J.D. Ardisson, M.G. Rosmaninho, R.M. Lago, J.C. Tristão, Hyperfine Interact 202 (2011) 123–129.
- [31] F. Dumitrache, I. Morjan, R. Alexandrescu, R.E. Morjan, I. Voicu, I. Sandu, I. Soare, M. Ploscaru, C. Fleaca, V. Ciupina, G. Prodan, B. Rand, R. Brydson, A. Woodward, Diamond Relat. Mater. 13 (2004) 362–370.
- [32] C. Jäger, H. Mutschke, F. Huisken, R. Alexandrescu, I. Morjan, F. Dumitrache, R. Barjega, I. Soare, B. David, O. Schneeweiss, Appl. Phys. A: Mater. Sci. Process. 85 (2006) 53–62.
- [33] N.N. Greenwood, T.C. Gibb, *Mössbauer Spectroscopy*, Chapman and Hall Ltd, London, 1971.

Dynamic hysteresis measurement in magnetic hyperthermia

Marija Perovic¹, Marko Boskovic¹, Viktor Cosic²

¹) Vinca Institute of Nuclear Sciences, Belgrade, Serbia

²) Custom Electronics Shack, Belgrade, Serbia

Abstract

This paper represents a very short introduction to hysteresis measurement in magnetic hyperthermia. Efficient use of magnetic hyperthermia in therapy demands knowledge of heating losses of the used material. Commonly, losses are determined using calorimetric setup. Here we present an overview of the setup and method based on measurement of fundamental properties of the system in high frequency region.

Hyperthermia implies elevation of tissue or body temperature above physiological limit [1]. Natural response of the body to infection, fever, serves as a defensive mechanism which hinders multiplication of viruses and bacteria. As is, the heat was recognized as powerful tool against illness centuries ago. Nowadays, local or total hyperthermia is regularly used in tumour therapy. Means of achieving hyperthermia differ widely - from hot baths and saunas to ultrasound, radiofrequency and microwave heating [1–3]. Conversion of externally applied field energy to heat often relies on tissue absorption, e.g., through generation of eddy currents in radiofrequency therapy. This approach, while common, has problems with nonspecific heating of the healthy tissue around tumour. Implants can help, either by focusing field in specified region, like antennas, or by acting directly as local heaters. Using implants raises overall efficacy of the method, but is often surgically demanding. Additionally, discrete distribution of implants gives rise to large temperature gradients inside the tissue [4].

Nanoparticles are regarded as promising replacement for bulky implants. They are easy to administer directly to tumour tissue by syringe, and can be localized at the targeted site only [4-7]. Homogenous distribution of nanoparticles is still something to desire for, so the temperature gradients have to be taken into account.

Magnetic hyperthermia relies on a fact that magnetic nanoparticles when subjected to AC magnetic field emit heat [1,2]. The underlying mechanism of this energy conversion depends on structural and magnetic properties of the nanoparticles [8–11]. Presently, the majority of papers are focused on iron oxide nanoparticles smaller than 30 nm - iron oxide because it's

approved material for medical uses, and nanoparticles in the range from 15 to 30 nm because they are most efficient as heat generators [1,12–14]. This type of nanoparticles dominantly heat by relaxation mechanism, either because of thermally induced jumps of particles' magnetic moment and, if the particles are suspended in liquid, because of random rotation of particles due to collision with molecules of the medium. Both of these mechanisms can be understood as some kind of "friction" which cause lag of the magnetization behind magnetic field and appearance of hysteresis [15,16].

Heating efficiency of magnetic nanoparticle is commonly measured by calorimetric type of setup [2,8,17]. Nanoparticle suspension is subjected to AC magnetic field (frequency ~ 100 kHz, field amplitude ~ 10 mT) and temperature of the suspension is measured (Figure 1, left). Heating power is proportional to the slope of the temperature curve, $P \propto dT/dt$ (Figure 1, right). [1,8,18]

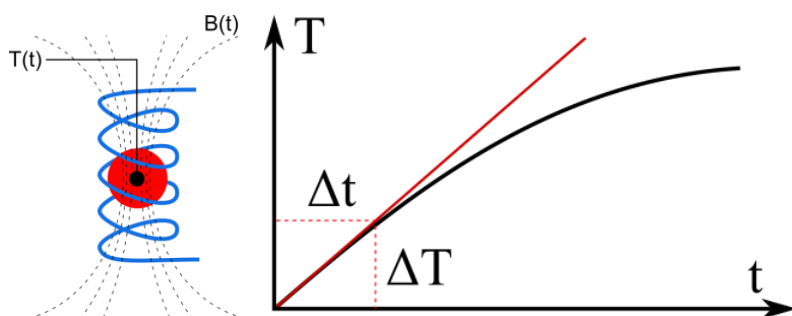


Figure 1. Left: Schematic representation of hyperthermia setup; Right: Sample temperature time dependence and maximum slope

Additionally, heating power can be deduced from magnetic measurements [19–21]. Any losses in the material subjected to cycling field cause appearance of open $M(H)$ loops, i.e. hysteresis (Figure 2) [22–24]. Area of the loop is equal to the work done by the AC field during one cycle. Total power loss can be then calculated as $P = f \oint M dH$, where f represents magnetic field frequency [15,25].

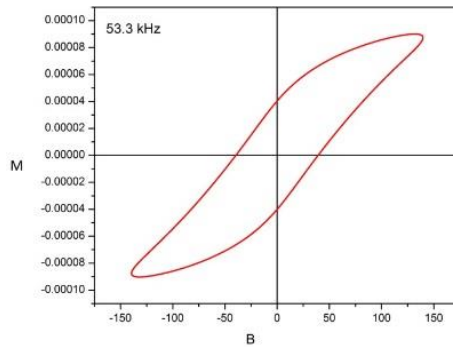


Figure 2. Dynamic hysteresis loop

Schematic presentation of the dynamic hysteresis measurement setup is shown in Figure 3. For the purpose of the experiment, AC magnetic fields with the frequency in the 100 kHz range and with field amplitude of several tens of mT are required. In order to create such fields, high frequency currents exceeding 100 A should be pumped through a field generating coil. Common way of achieving this is by using some kind of resonant circuit. In our lab-made magnetometer we are using parallel LC circuit. At the resonant frequency it behaves as current amplifier, so a relatively low current from linear amplifier maintains large current oscillating between capacitor and coil. Different resonant frequencies are achieved using different values of capacitance.

Detection of the magnetic sample response to external AC field is based on the law of induction. Sample is mounted inside the detection coil and any change of sample's magnetization induces voltage in the detection coil. The detection coil has a configuration of the first order gradiometer [26,27]. It consists of two equal spaced coils connected in series but wound in opposite direction. External field induces opposite currents inside the two coils which cancel each other. On the other hand, sample mounted inside one of the coils induces measurable signal only in that coil. An additional coil is used to measure field change (Figure 3). This allows us to reconstruct time dependence of magnetization and external field, and consequently dependence of magnetization on field, $M(H)$.

Signal acquisition is done by digital oscilloscope. Acquired response of the sample for two different field amplitudes can be seen in Figure 4. Saw tooth shape points to presence of higher harmonics when larger fields are applied. In the reconstructed hysteresis higher harmonics will be recognized as bending of the curve toward saturation.

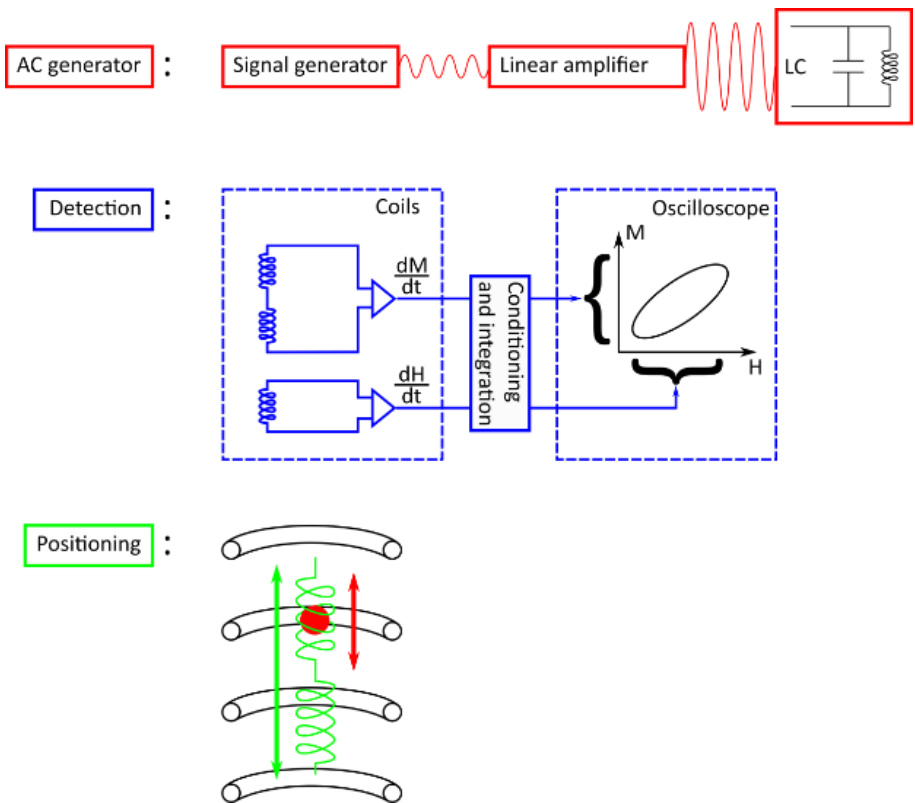


Figure 3. Block diagram of the dynamic hysteresis magnetometer

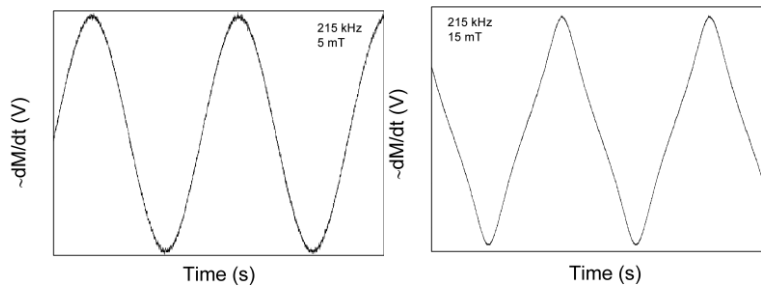


Figure 4. Raw signal from the detection coil for low amplitude – left and high amplitude – right

Numeric integration of signals gives us the $M(t)$ and $H(t)$ dependence. By elimination of t we finally acquire $M(H)$. Example of the hysteresis curves measured in different fields can be seen in Figure 5. Heating power of the sample is proportional to the area of the loop, and, as expected, grows the bigger the amplitude used.

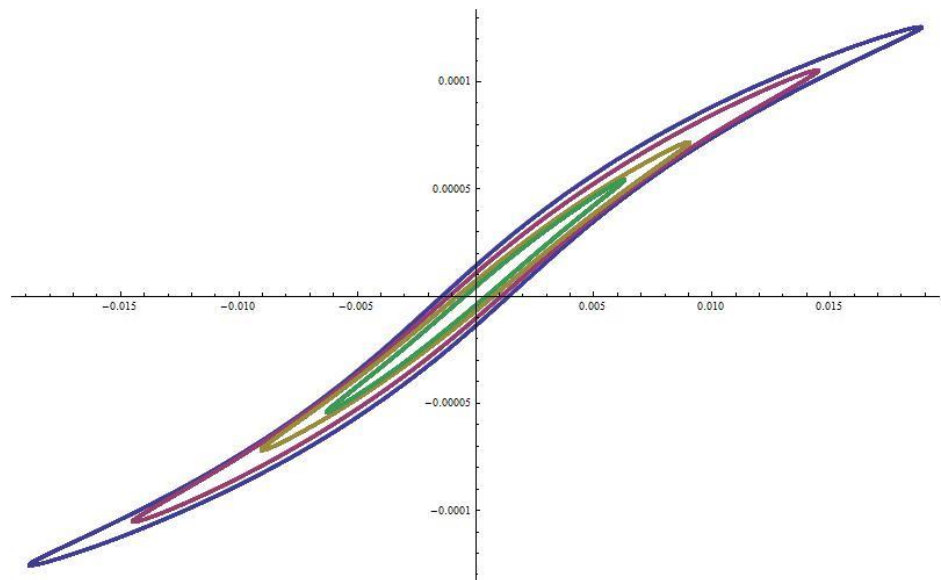


Figure 5. Dynamic hysteresis loops measured for different amplitudes at 215 kHz

Further analysis of the heating power behaviour with frequency and amplitude can reveal the mechanism behind heat generation [9,28]. On the other hand, higher harmonics appearing in the raw signal can be used to estimate temperature of the particles [29].

References

- [1] S. Dutz, R. Hergt, Magnetic particle hyperthermia—a promising tumour therapy?, *Nanotechnology*. 25 (2014) 452001. doi:10.1088/0957-4484/25/45/452001.
- [2] R. Hergt, S. Dutz, Magnetic particle hyperthermia—biophysical limitations of a visionary tumour therapy, *J. Magn. Magn. Mater.* 311 (2007) 187–192. doi:10.1016/j.jmmm.2006.10.1156.
- [3] I. Baker, Q. Zeng, W. Li, C.R. Sullivan, Heat deposition in iron oxide and iron nanoparticles for localized hyperthermia, *J. Appl. Phys.* 99 (2006) 1–4. doi:10.1063/1.2171960.
- [4] R.K. Gilchrist, R. Medal, W.D. Shorey, R.C. Hanselman, J.C. Parrott, C.B. Taylor, Selective Inuctive Heating of Lymph Nodes, *Ann. Surg.* 146 (1967).
- [5] A. Jordan, P. Wust, H. Fähling, W. John, a Hinz, R. Felix, Inductive heating of ferrimagnetic particles and magnetic fluids: physical evaluation of their potential for hyperthermia., *Int. J. Hyperthermia.* 9 (1993) 51–68. doi:10.3109/02656739309061478.
- [6] A. Jordan, R. Scholz, K. Maier-Hauff, F.K.H. van Landeghem, N. Waldoefner, U. Teichgraeber, J. Pinkernelle, H. Bruhn, F. Neumann, B. Thiesen, A. von Deimling, R. Felix, The effect of thermotherapy using magnetic nanoparticles on rat malignant glioma, *J. Neurooncol.* 78 (2006) 7–14. doi:10.1007/s11060-005-9059-z.

- [7] R. Ivkov, Magnetic nanoparticle hyperthermia: a new frontier in biology and medicine?, *Int. J. Hyperthermia*. 29 (2013) 703–5. doi:10.3109/02656736.2013.857434.
- [8] H. Mamiya, Recent Advances in Understanding Magnetic Nanoparticles in AC Magnetic Fields and Optimal Design for Targeted Hyperthermia, *J. Nanomater.* 2013 (2013) 1–17. doi:10.1155/2013/752973.
- [9] J. Carrey, B. Mehdaoui, M. Respaud, Simple models for dynamic hysteresis loop calculations of magnetic single-domain nanoparticles: Application to magnetic hyperthermia optimization, *J. Appl. Phys.* 109 (2011) 083921. doi:10.1063/1.3551582.
- [10] E. Lima, E. De Biasi, R.D. Zysler, M. Vasquez Mansilla, M.L. Mojica-Pisciotti, T.E. Torres, M.P. Calatayud, C. Marquina, M. Ricardo Ibarra, G.F. Goya, Relaxation time diagram for identifying heat generation mechanisms in magnetic fluid hyperthermia, *J. Nanoparticle Res.* 16 (2014) 2791. doi:10.1007/s11051-014-2791-6.
- [11] C.L. Dennis, R. Ivkov, Physics of heat generation using magnetic nanoparticles for hyperthermia, *Int. J. Hyperth.* 29 (2013) 715–729. doi:10.3109/02656736.2013.836758.
- [12] P. Tartaj, M.P. Morales, T. Gonzalez-Carreño, S. Veintemillas-Verdaguer, C.J. Serna, The Iron Oxides Strike Back: From Biomedical Applications to Energy Storage Devices and Photoelectrochemical Water Splitting, *Adv. Mater.* 23 (2011) 5243–5249. doi:10.1002/adma.201101368.
- [13] M.A. Gonzalez-Fernandez, T.E. Torres, M. Andrés-Vergés, R. Costo, P. de la Presa, C.J. Serna, M.P. Morales, C. Marquina, M.R. Ibarra, G.F. Goya, Magnetic nanoparticles for power absorption: Optimizing size, shape and magnetic properties, *J. Solid State Chem.* 182 (2009) 2779–2784. doi:10.1016/j.jssc.2009.07.047.
- [14] R. Tetean, R. Stiufiuc, C.M. Lucaciuc, Small versus Large Iron Oxide Magnetic Nanoparticles: Hyperthermia and Cell Uptake Properties, (n.d.) 1–21. doi:10.3390/molecules21101357.
- [15] G. Bertotti, *Hysteresis in Magnetism: For Physicists, Materials Scientists, and Engineers*, Academic Press, 1998.
- [16] E. Della Torre, *Magnetic Hysteresis*, IEE Press, 1999.
- [17] I. Andreu, E. Natividad, Accuracy of available methods for quantifying the heat power generation of nanoparticles for magnetic hyperthermia., *Int. J. Hyperthermia*. 29 (2013) 739–51. doi:10.3109/02656736.2013.826825.
- [18] N. Iacob, G. Schinteie, P. Palade, V. Kuncser, Approach for an improved experimental evaluation of the specific absorption rate in magnetic fluid hyperthermia, *J. Nanoparticle Res.* 17 (2015). doi:10.1007/s11051-015-2997-2.
- [19] H.W. Lord, Dynamic Hysteresis Loop Measuring Equipment, (1952) 269–272.
- [20] V. Connord, B. Mehdaoui, R.P. Tan, J. Carrey, M. Respaud, An air-cooled Litz wire coil for measuring the high frequency hysteresis loops of magnetic samples - A useful setup for magnetic hyperthermia applications, *Rev. Sci. Instrum.* 85 (2014). doi:10.1063/1.4895656.
- [21] E. Garaio, J.M. Collantes, F. Plazaola, J.A. Garcia, I. Castellanos-Rubio, A multifrequency electromagnetic applicator with an integrated AC magnetometer for magnetic hyperthermia experiments, *Meas. Sci. Technol.*

- 25 (2014) 115702. doi:10.1088/0957-0233/25/11/115702.
- [22] V.M. Chernyshev, Measurement of Energy Dissipation by Means of the Dynamic Hysteresis Loop, 60052 (1970) 553–557.
- [23] Y.L. Raikher, V.I. Stepanov, R. Perzynski, Dynamic hysteresis of a superparamagnetic nanoparticle, *Phys. B Condens. Matter.* 343 (2004) 262–266. doi:10.1016/j.physb.2003.08.105.
- [24] Y.P. Kalmykov, S. V. Titov, W.T. Coffey, Nonlinear ac stationary response and dynamic magnetic hysteresis of quantum uniaxial superparamagnets, *Phys. Rev. B - Condens. Matter Mater. Phys.* 92 (2015) 1–28. doi:10.1103/PhysRevB.92.174414.
- [25] M. Getzlaff, *Fundamentals of Magnetism*, Springer Berlin Heidelberg, Berlin, Heidelberg, 2008. doi:10.1007/978-3-540-31152-2.
- [26] A.C. Fraser-Smith, *The Magnetic Field Gradiometer*, 1983.
- [27] S. Tumanski, Induction coil sensors—a review, *Meas. Sci. Technol.* 18 (2007) R31–R46. doi:10.1088/0957-0233/18/3/R01.
- [28] R.E.E. Rosensweig, Heating magnetic fluid with alternating magnetic field, *J. Magn. Mater.* 252 (2002) 370–374. doi:10.1016/S0304-8853(02)00706-0.
- [29] E. Garaio, J.M. Collantes, J.A. Garcia, F. Plazaola, O. Sandre, Harmonic phases of the nanoparticle magnetization: An intrinsic temperature probe, *Appl. Phys. Lett.* 107 (2015) 3–8. doi:10.1063/1.4931457.

Spin configurations in RE-Fe and RE-Fe-B systems and related functionalities

A. E. Stanciu ⁽¹⁾, C. Locovei ^(1,2), G. Schinteie ⁽¹⁾, N. Iacob ⁽¹⁾, V. Kuncser ⁽¹⁾
¹*National Institute for Materials Physics, P.O.Box MG-7, 077125, Bucharest-Magurele, Romania*
²*Bucharest University, Faculty of Physics, 077125, Bucharest-Magurele, Romania*

Abstract: Different types of functionalities can be attributed to Fe-RE and Fe-RE-B systems with RE=Gd, Dy and Sm. Local spin configurations, magnetic behavior and magneto-functionalities have been studied in such systems prepared as thin films and ribbons. Morpho-structural and magnetic characterization have been performed by various techniques and the magnetic specificities have been correlated with local structure around Fe atoms investigated by ⁵⁷Fe Conversion Electron Mossbauer Spectroscopy. Concentration dependent magneto-optical behavior has been observed in Fe-Gd films. Direct or reversed MOKE loops were evidenced crossing the magnetization compensation point due mainly to the negligible rotational effect of Gd as compared to Fe. The magnetic anisotropy and the magnitude of the Fe magnetic moment depend strongly on the RE content, in different fashions for films and ribbons. Magnetostrictive effects were investigated in ribbons, in direct correlation with the atomic local structure and spin reorientation investigated by transmission Mössbauer spectroscopy at different temperatures.

Introduction

The distribution of the magnetic interaction strength specific to amorphous magnetic materials inspired many studies related to the magnetic, magneto-optical and magneto-transport properties of amorphous RE-TM alloys [1-3], with RE=Rare Earth and TM=Transition Metal elements. Structural disorder influences a variety of magnetic related functionalities, making these materials suitable for applications in magneto-optical recording [4], spintronics [5-6] and for magnetization switching without an external applied magnetic field [7-10].

Different local configurations lead to the occurrence of random crystal fields that modify the magnitude of the RE and TM magnetic moments. If the RE ion has non-zero orbital angular momentum, the orientation of the RE magnetic moments will be modified in addition to its magnitude. Thus, a random orientation of RE atomic magnetic moments is expected if their orbital angular momentum is non-zero, as a result of local

disorder. Structural disorder of amorphous materials generates three important effects: (i) an additional attenuation of the exchange integrals, (ii) a distribution of the exchange integrals linked to their interatomic distance dependence and (iii) a sign variation of the exchange integrals specific to their oscillatory character in intermetallic systems. These effects produce features specific to amorphous magnetic materials like percolation phenomena and spin frustration.

The magnetic properties depend strongly on the strength of the crystalline field acting on the TM and RE atoms. The crystalline fields are responsible for the magneto-crystalline anisotropy in the case of crystalline materials. Harris, Plische and Zukermann proposed that for amorphous RE elements with non-zero orbital angular momentum, the crystalline fields are uni-axial, with easy axis varying from atom to atom in the case of total disorder [11]. The local anisotropy originates in the interaction of the non-spherical charge distribution of “f” electrons with the electric field produced by neighboring ions. RE ions with non-zero orbital angular momentum are anisotropic, whereas those with null orbital angular momentum are isotropic. The magnetic behavior (for a single magnetic lattice) can be theoretically analyzed using the Harris - Plische - Zuckermann Hamiltonian, completed with a term corresponding to the coherent anisotropy [12]:

$$H = - \sum_{i,j} I_{i,j} \vec{J}_i \vec{J}_j - D \sum_i (\vec{n}_i \cdot \vec{J}_i)^2 - D_{ind} \sum_i (n \cdot \vec{J}_i)^2 - g\mu_B H \sum_i \vec{J}_i,$$

where the first term represents the exchange interactions, the second term corresponds to the local random anisotropy, the third term counts for the coherent anisotropy and the last one is the Zeeman energy. The coherent anisotropy is due to the tensile stresses that occur during the preparation process of amorphous ferromagnets.

Non-collinear spin structures are highlighted in the case of rare earth compounds due mainly to the competition between exchange interaction and magnetic anisotropy. The structural disorder specific to amorphous materials leads to the formation of particular spin configurations, classified for the first time by Coey [13-14]. A probability for a spin to form a ψ angle with a given direction was defined. In the case of a single magnetic lattice, the spin configuration can be either ferromagnetic or speromagnetic/asperomagnetic (transforming in random configurations, in particular cases). If the exchange interaction is much stronger than the ionic anisotropy, the magnetic moments will be coupled on a significant correlation length. Thus, the ferromagnetic coupling will be favored. If the ionic anisotropy is much greater than the exchange interaction, the spin correlation will disappear, the atomic spins being oriented along their easy axis of magnetization which varies from site to site. Hence, an overall random spin orientation is advantaged. If the exchange interaction competes with the ionic anisotropy, the correlation

length is enhanced with respect to the previous situation and a sperimagnetic/asperomagnetic configuration will form.

In the case of two magnetic lattices, A and B (with A=RE and B=TM), the magnetic Hamiltonian reads:

$$H = -\frac{1}{2} \sum_{\alpha,\beta} I_{\alpha,\beta} \vec{J}_\alpha \vec{J}_\beta - \sum_{\alpha>\alpha'} I_{\alpha,\alpha'} \vec{J}_\alpha \vec{J}_{\alpha'} - \sum_{\beta>\beta'} I_{\beta,\beta'} \vec{J}_\beta \vec{J}_{\beta'} - \sum_{\alpha} D_{\alpha} (\vec{n}_{\alpha} \vec{J}_{\alpha})^2 - \sum_{\beta} D_{\beta} (\vec{n}_{\beta} \vec{J}_{\beta})^2$$

where the first term refers to the A-B coupling, the second and the third term represent the A-A and B-B coupling, whereas the fourth and fifth term are related to the random anisotropy of the A and B sub-lattices, respectively (the coherent anisotropy and the Zeeman term were neglected). A RE-TM alloy exhibits two possible spin configurations: if the RE belongs to the light RE category (RE with less than half-filled f orbitals), the total local moment of RE atoms couples ferromagnetically to the TM local moments (The exchange integral, $I_{\alpha\beta}$, is positive). If the RE belongs to the heavy RE category (RE with more than half-filled f orbitals), the total local moment of RE atoms couples antiferromagnetically to the TM local moments (The exchange integral, $I_{\alpha\beta}$, is negative) [15]. An essential large local anisotropy could come only for the RE lattice (in case of anisotropic RE elements), the contribution of the TM sublattice (B), being negligible.

According to the interactions appearing in the Hamiltonian above, if the local anisotropy is small compared to the strength of the exchange interactions, the coupling between the two lattices can be either ferromagnetic or ferimagnetic/antiferromagnetic, depending on the sign of the exchange integral, $I_{\alpha\beta}$. If the strength of the local anisotropy of the RE (A) magnetic lattice is comparable to the exchange interaction, the angular distribution of magnetic moments belonging to the A lattice will be anisotropic, whereas the B lattice will lose its ferromagnetic character. The speromagnetic/asperomagnetic configuration is favored in different forms, depending on the sign of the exchange integral ($I_{\alpha\beta}$) and on the ratio between the exchange interaction and the local anisotropy.

Expressions for the angular orientations of the RE and TM spins relative to the direction of the applied field, in the molecular field approximation, were derived in ref. [16]. It was proved that in the case of a very low random anisotropy of the RE atoms, a ferro- or ferrimagnetic coupling occurs. In the opposite case, the RE spins are disposed in a cone along the applied field and show a linear dependence on it.

Generally, the random anisotropy of TM elements is negligible (as a result of orbital angular momentum quenching), whereas the RE-RE exchange interactions is weak due to the significant distance between RE ions in conditions of a small RE concentration in this type of alloys. A particular case is the one of Gd atoms, given their null orbital angular

momentum. They do not present random magnetic anisotropy and show a simple antiferromagnetic coupling with TM magnetic moments. Consequently, the anti-ferromagnetic alignment of TM and Gd magnetic moments introduces the possibility to establish a certain concentration for which the magnetization values corresponding to each sub-lattice would be almost equal.

One important feature of electron beam co-evaporated Fe-Gd thin films is the perpendicular easy axis of anisotropy causing a perpendicular to plane magnetization. This observation enabled their implementation in "bubble devices" [17-18]. Furthermore, it was observed that for this type of films, the preparation method could increase the saturation magnetization by an order of magnitude in the case of evaporated films with respect to their sputtered counterparts, but in both cases the same tendency of saturation magnetization decreasing until reaching a minimum at the compensation concentration, followed by an increase in saturation magnetization with increasing concentration is valid [3]. Also, the possibility to tune the perpendicular anisotropy by means of composition and temperature was reported in Gd-Fe-Co thin films with 50 nm thickness. Thus, the low Gd concentration range between 20 % and 34 % was found to exhibit perpendicular magnetic anisotropy and local ion anisotropy was proposed to explain its origin in this type of alloys [19].

Magnetic configurations and magnetic interactions in RE-TM systems, with or without an additional Boron content, prepared as both thin films and ribbons were previously studied using Mössbauer spectroscopy and magnetometry techniques. The effect of adding B is to ascertain the amorphous state of the systems [20-22]. Considering Fe-Gd-B, the data showed different local electron configuration of Fe: for a Gd concentration lower than 20%, the hyperfine field decreases with increasing Gd concentration in the ribbons case, whereas it has similar values in the film case at Gd concentrations lower than 8%. The overall magnetic moments in Fe-Gd-B ribbons do not prefer a certain orientation, whereas in the case of films the magnetization lies in the film plane at Gd concentrations lower than 8 % and it prefers the out of plane direction at concentrations higher than 8 %. Despite being known that light rare earth elements couple ferromagnetically with transition metal elements, magnetic data in ref. [23] demonstrated that in Fe-Sm-B films with Sm concentration less than 30 %, contrary to ribbons and Fe-Sm films, the magnetic moments of Fe and Sm are antiferromagnetically coupled.

The present work is intended to present disordered magnetism related features in isotropic and anisotropic RE-TM systems prepared as thin films and ribbons. In the ribbons case, the preparation technique allows adding B in the sample composition. Adding B in the ribbons composition is a prerequisite for obtaining non-collinear spin structures by ensuring the amorphous character of the samples. In this respect, we

propose for investigations Fe-Gd and Fe-Dy thin films systems and an Fe-Dy-B ribbons system. A good understanding of the magnetic behavior of the system requires extracting information about one of the two magnetic lattices. Mössbauer spectroscopy can be used in this respect due to its isotope specific nature. In the following examples, Mössbauer spectroscopy results provide information about local atomic structure, magnetic configurations and magnetic interactions at the TM (particularly Fe) site.

Experimental details

The Fe-Gd and Fe-Dy thin films were prepared by magnetron sputtering on Si substrate in Ar atmosphere (11.1 mbar) after reaching a main vacuum of $5 \cdot 10^{-9}$ mbar. The substrates were washed in acetone and ethyl alcohol, but the endemic Si oxide layer was not removed. The iron concentration in the two systems was varied by sputtering from two different targets: a high purity Fe target of 5 cm diameter partially covered with small plackets of metallic Fe enriched in the ^{57}Fe isotope and with eight Gd/Dy plackets of about 0.35 cm^2 surface and an additional Fe target. The deposition parameters of the Fe-Gd and Fe-Dy films are listed in table 1. The sample code indicates the Fe concentration found in each sample. The composition was obtained via Scanning Electron Microscopy coupled with Energy Dispersive Spectroscopy (data not shown here).

| Sample code | Deposition parameters (deposition power, discharge type, deposition time) |
|-------------|---|
| Fe74 | Si/ Fe + ^{57}Fe + Gd(100W, RF, 16') – Au (100W, RF, 16') |
| Fe79 | Si/ Fe (25W, DC, 24') - Fe + ^{57}Fe + Gd (100W, RF, 24') |
| Fe90 | Si/ Fe (25W, DC, 15') - Fe + ^{57}Fe + Gd(100W, RF, 15') |
| Fe83 | Si/Fe-Dy (100 W, RF, 15') - Fe (100 W, DC, 15') / Ag (50 W, 2' 30'') |
| Fe91 | Si/Fe-Dy (65W, RF, 17'30'')-Fe (140W, DC, 17'30'')/Ag(50W, 2'30'') |

Table 1. Sample codes and deposition parameters for the Fe-Gd and Fe-Dy films

The Fe-Dy-B ribbons system was prepared by pre-melting in induction furnace followed by melt spinning. The preparation parameters are shown in Table 2.

| Atomic composition | Crucible diameter (mm) | Overpressure Ar (MPa) | Rotational speed of the Cu wheel (rpm) | Working pressure (Atm) |
|---|------------------------|-----------------------|--|------------------------|
| Fe _{66.4} Dy _{13.6} B ₂₀ | 0.5 | 0.07 | 2000 | 0.9 |
| Fe _{72.8} Dy _{7.2} B ₂₀ | 0.5 | 0.07 | 2000 | 0.9 |

Table 2. Atomic composition and preparation parameters of the Fe-Dy-B ribbons

Except these samples, complex magnetic investigations have been done on films involving other RE ions, as for example Sm. Conversion Electron Mössbauer Spectroscopy (CEMS) was used in order to study local structure, magnetic configurations and magnetic interactions of the Fe-RE films. The measurements were performed at room temperature with the gamma radiation perpendicular to the sample plane, the sample being placed in a home-made gas flow proportional counter. A ^{57}Co source (Rh matrix) of about 35 mCi activity and a spectrometer working with sinusoidal waveform was used. Transmission Mossbauer Spectroscopy (TMS) was implemented to investigate the magnetic configurations in Fe-RE-B ribbons. A conventional Mössbauer spectrometer with a ^{57}Co (Rh matrix) source mounted on a drive unit working under the constant acceleration mode was used. The NORMOS computer program [24] was used for the least-squares fitting of the Mössbauer spectra.

Magnetometry measurements of the Fe-Gd and Fe-Dy films were performed on a SQUID (Superconducting Quantum Interference Device) magnetometer at room temperature (RT) in parallel geometry (the magnetic field was applied parallel to the sample plane).

Results and discussions

CEM spectra of Fe74 and Fe79 films and their corresponding hyperfine field distributions are presented in figure 1. The spectra were fitted with a hyperfine field distribution specific to amorphous phases (the amorphous character of the samples was also revealed by X-ray diffraction, but the results are not presented here). The quadrupole splitting was considered zero. The magnetic splitting increases, whereas the spectral linewidth becomes narrower with increasing Fe concentration. Thus, the observation of six distinct spectral lines is possible only for Fe79. The isomer shift values indicate the formation of amorphous phases for the two samples. The orientation of the hyperfine field with respect to the direction of γ radiation was estimated via the intensity ratio R . The R ratio is expressed with the following formula: $R = \frac{I_2}{I_1} = \frac{4\sin^2\beta}{3(1+\cos^2\beta)}$, where I_2 and I_1 are the intensities of spectral lines 2 and 1, and β is the angle between the direction of the hyperfine field and the direction of γ rays [25]. R shows an in-plane orientation of the mean magnetic moment of Fe in the case of Fe79 film and a perpendicular to plane component in the case of Fe74. An unexpected observation is the significant drop of the mean hyperfine field value registered for Fe74 sample (6.8 T) with respect to the value obtained in the case of Fe79 sample (17.5 T), given the small Fe concentration difference between them. This remark can be attributed either to an electron reconfiguration at the Fe site occurred due to an increased number of Gd neighbours in the case of Fe79 as compared to Fe74, or to the activation of magnetic relaxation processes for the Fe lattice, leading to the

reduction of the magnetic moment, and hence to a lower hyperfine field value. Ab-initio simulations (results not presented here) on crystalline counterpart systems of similar concentrations revealed not important variations of the magnetic moment with changing Fe concentration. Hence, the observed hyperfine field reduction should be attributed to the activated magnetization relaxation processes.

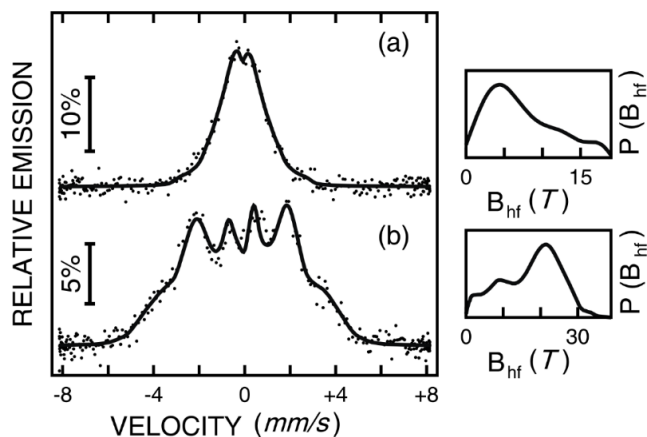


Figure 1. CEM spectra collected at room temperature of Fe74 (a) and Fe79 (b) films

Figure 2 presents CEM spectra of Fe83 and Fe91 films. The best fit of Fe83 spectrum was obtained considering a narrowed hyperfine field distribution centered in 1.2 T and a low value (close to 0) for R, indicating a perpendicular to plane orientation of Fe spins. An unique amorphous phase with a reduced magnetic moment of Fe was highlighted for this sample, the magnetic moment being much lower than in case of metallic Fe. The Fe91 spectrum was fitted with a crystalline sextet of narrow linewidths corresponding to Fe-bcc phase and with a second sextet with broader lines associated to locally disordered Fe positions with Dy neighbors, according to XRD data (not shown here). The relative intensities of the sextet lines 2 and 1 in both sextets prove also a strong perpendicular to plane component of the Fe spins.

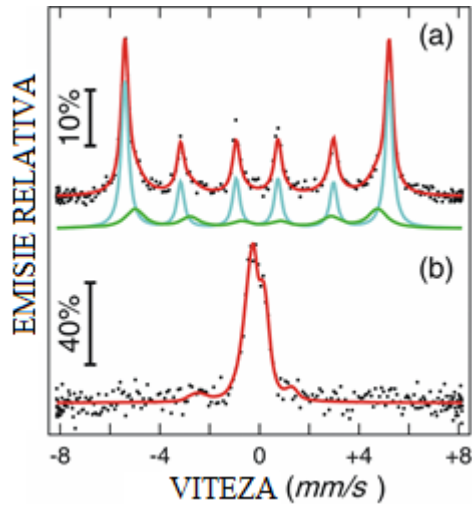


Figure 2. CEM spectra collected at room temperature of Fe91 (a) and Fe83 (b) films

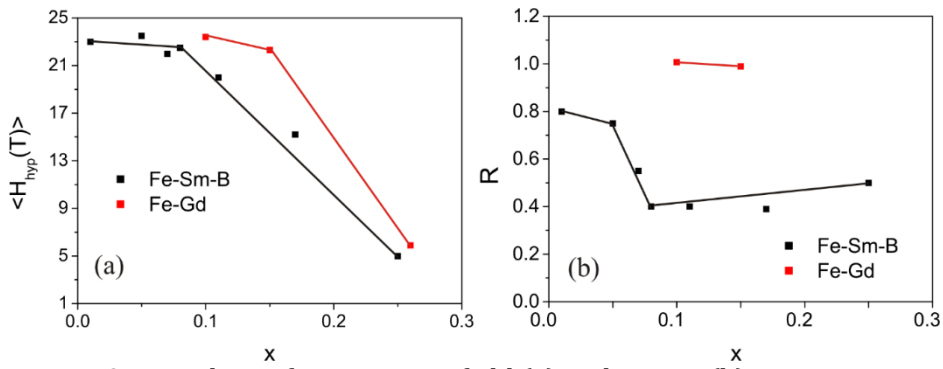


Figure 3. Mean hyperfine magnetic field (a) and R ratio (b) vs. RE content in Fe-Sm-B and Fe-Gd films collected at 300 K

The mean hyperfine field and R ratio dependences vs RE content, as derived from CEMS on Fe-Sm-B and Fe-Gd films of different compositions are illustrated in figure 3. The mean hyperfine field is constant for RE concentrations lower than 0.1 and decreases rapidly for RE concentrations higher than 0.1. A rapid decrease is also observed for R values corresponding to Sm-based films at concentrations higher than 0.05 as a sign of the spins rotation towards a more perpendicular to plane direction.

Room temperature hysteresis loops of Fe74 (in 250 Oe applied field) and of Fe79 (in 60 Oe applied field) collected on the SQUID magnetometer in parallel geometry (magnetic field applied along the film plane) are shown in figure 4. The hysteresis loop of Fe74 shows soft-magnetic features. Moreover, it is easily closed, suggesting the formation of

magnetic domains in this sample. Oppositely, the hysteresis loop of Fe79 prove the existence of two magnetic phases with different coercive field values, each one of them having a correspondent magnetic phase. It was previously concluded that in RE – TM amorphous compounds an exchange coupling between a ferrimagnetic region (with low net magnetic moment) and a “so-called” ferromagnetic region (with a significant magnetic moment) exists [25]. It is assumed that the regions with different concentrations are of nanometric size and are placed in contact. The two magnetic phases observed in the hysteresis loop may be attributed to the two exchange coupled phases presenting different magnetism.

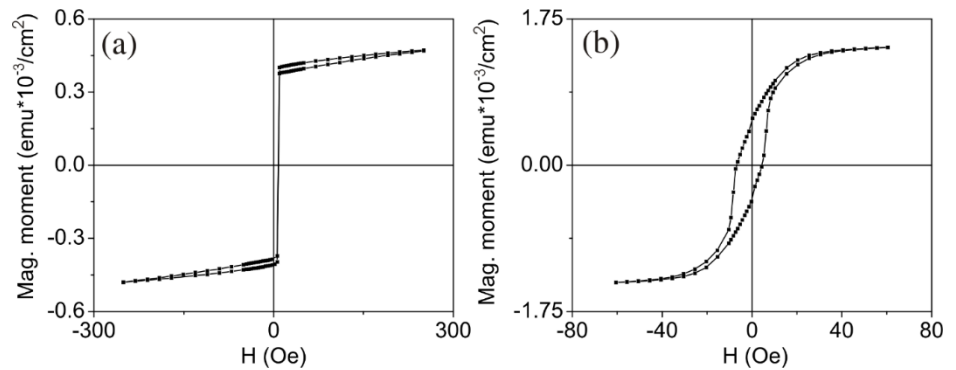


Figure 4. RT hysteresis loops collected on SQUID magnetometer in parallel geometry for Fe74 (a) and Fe79 (b) films

Figure 5 presents the saturation magnetization values vs. Fe content in Fe-Gd films. In the case of ferrimagnetic structures, a minimum net magnetization is expected for concentrations in the vicinity of the compensation point. Among the concentration values considered, the minimum magnetization saturation value was obtained for 85 % Fe, which can be considered as the closest concentration to the compensation point at RT.

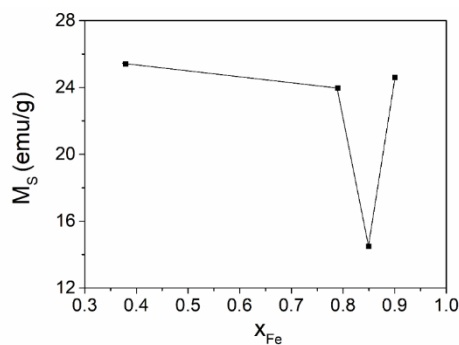


Figure 5. Saturation magnetization vs. Fe content in Fe-Gd thin films at 300 K

Magnetic hysteresis loops of Fe83 and Fe91 films in perpendicular geometry can be seen in figure 6. In both cases there are evidences for the presence of two coupled magnetic phases leading to both the multicomponent nature and different shifts of the overall hysteresis loop. The averaged coercive field of Fe91 of approximately 200 Oe is four times higher than that of Fe81. Both samples are hardly to be saturated in a direction perpendicular to the film plane, indicating non-collinearity of the spin structure. The shifts of the hysteresis loops along the magnetic field axis (negative, for Fe83 and positive for Fe91 film, respectively) field observed for the two samples is a hint for exchange-bias phenomena.

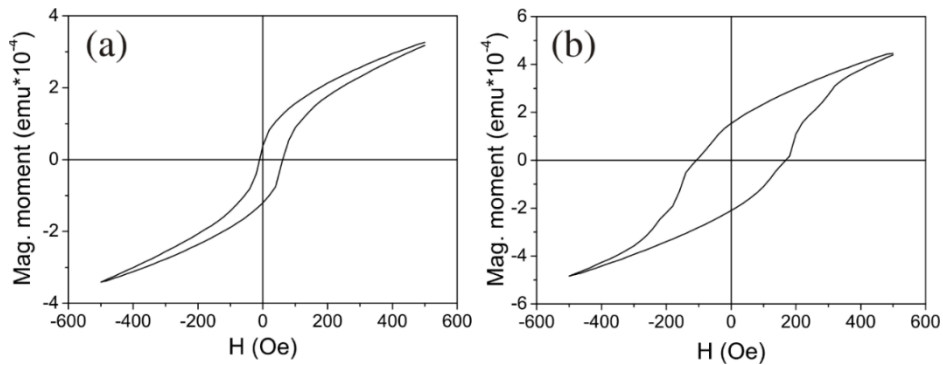


Figure 6. Magnetic hysteresis loops of Fe83 (a) and Fe91 (b) films, collected in perpendicular geometry, at room temperature

It is to be assumed that Fe-Dy films present, as well as Fe-Gd counterparts, an exchange coupling between “ferrimagnetic regions” with a concentration close to the compensation point and “ferromagnetic regions” with a concentration much different than the compensation point. The magnetic moments corresponding to atoms of the same type present parallel coupling. The regions with concentrations different than the compensation point are represented by Dy related magnetic moments and Fe related magnetic moments in the case of Fe83 and Fe91 films, respectively (e.g. the effective magnetic moment per formula unit of those phase with compositions different from the compensation point are due to either Dy or Fe magnetic moments). This affirmation is supported by CEM spectra (figure 2) presenting a reduced hyperfine field in the case of Fe83 and a hyperfine field close to that of α -Fe in the case of Fe91.

Decreasing Fe concentration from one side to the other of the compensation point produces different magneto-optical Kerr effects as can be seen in figure 7, where the MOKE loops of Fe79 and Fe90 films are represented. Relative higher coercive field is obtained for Fe90 (e.g. of 55(5) Oe) and the absence of magnetic anisotropy is observed. The coercive

field is well reduced in sample Fe79 (10(2) Oe), revealing a soft-magnetic character, at Fe concentration lower than the compensation point.

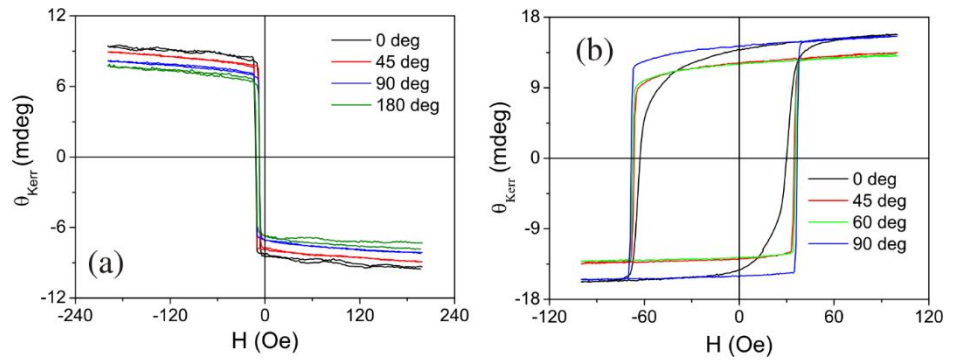


Figure 7. Magneto-optical Kerr effect loops of Fe79 (a) and Fe90 (b) films

Diminished MOKE effects are registered also with decreasing Fe concentration due to the fact that Gd, being an isotropic ion, with null orbital angular momentum and hence with null spin-orbit coupling, does not contribute to MOKE signal. A direct consequence of the null spin-orbit coupling of Gd is the MOKE loop reversal at Fe concentrations lower than the compensation point. It is the case of Fe79 film, where the MOKE signal is negative at positive applied fields and positive at negative applied fields. Changing MOKE signal sign appears as the Fe lattice (the minor lattice in the compound and the lattice creating magneto-optical effect) is oriented in the opposite direction of the applied field at both positive and negative values.

In order to investigate the influence of size effects and of the preparation method on the atomic structure and spin configuration of RE-TM systems, Mössbauer spectroscopy measurements of Fe-Dy-B and Fe-Sm-B ribbons were realized. Moreover, the ribbons preparation method allows the increase of B concentration in a higher amount than in the case of films. The TM spectra of $\text{Fe}_{72.8}\text{Dy}_{7.2}\text{B}_{20}$ and $\text{Fe}_{66.4}\text{Dy}_{13.6}\text{B}_{20}$ ribbons collected at 80 K and 300 K can be seen in figure 9.

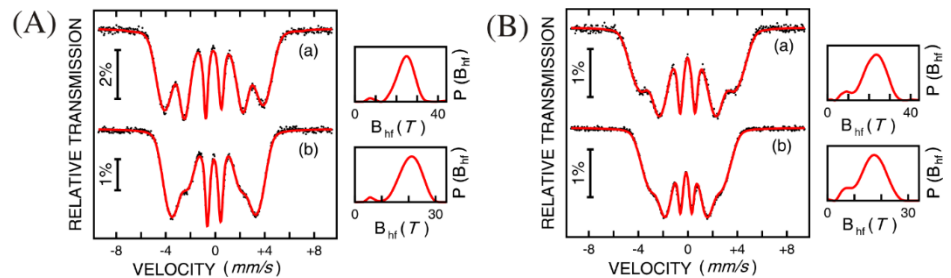


Figure 9. TM spectra collected at 80 K (a) and 300 K (b) of $\text{Fe}_{72.8}\text{Dy}_{7.2}\text{B}_{20}$ (A) and $\text{Fe}_{66.4}\text{Dy}_{13.6}\text{B}_{20}$ (B) ribbons

The best fit of the spectra was obtained via hyperfine magnetic field distributions. The spectral lines are more overlapped at 300 K, but can be well observed separately at 80 K. The width of spectral lines indicates clearly the formation of the desired amorphous phases in the case of both samples. The hyperfine field of Fe in this alloys is slightly higher than half of the metallic Fe hyperfine field. This reduction can be attributed to the polarization of s electrons of Fe by its magnetic moment or by the neighboring RE magnetic moments (e.g. in case of Dy, of opposite orientation as compared to Fe). The hyperfine field reduction is consistent with the existence of non-collinear spin structures. The hyperfine field values and the R ratio are represented in figures 10 and 11 for Fe-Sm-B, Fe-Dy-B and Fe-Gd-B ribbons, respectively.

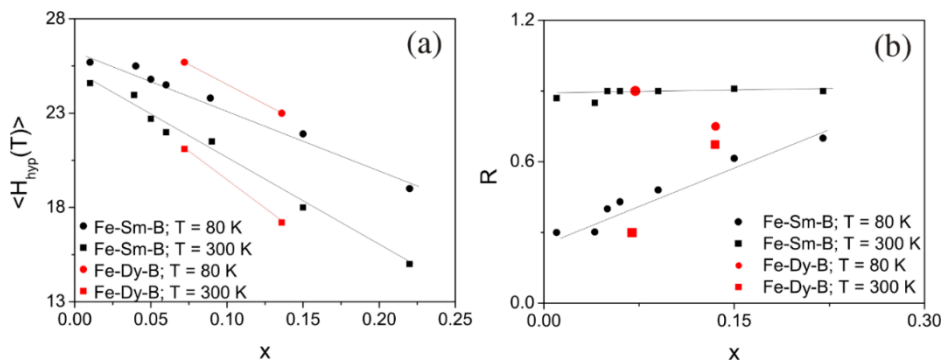


Figure 10. Mean hyperfine magnetic field (a) and R ratio (b) vs. RE content in Fe-Sm-B and Fe-Dy-B ribbons from Mössbauer spectra collected at 300 K and 80 K.

A decrease of the hyperfine field with increasing RE concentration is registered independent of temperature and of RE element, proving unexpectedly a same type of antiferromagnetic coupling between Fe and RE elements, in spite of fact that Sm is a light RE and Dy a heavy one. The variations of R at increased RE concentrations are much smaller in case of Sm as compared to the case of Dy. However, in both cases there is a sensible variation of R between the two considered temperatures (300 K and 80 K), proving the presence of magnetostrictive effects in both systems. In general, the spins tend to orient more in the out of plane direction as the temperature is increased, but the variation of R parameter is more accentuated in the case of the lowest RE content. A temperature increase of the ribbons that leads to their dilatation can be assimilated with applying an elongation stress (causing the same dilatation effect). The reorientation of the spins in the ribbons plane with changing temperature is equivalent with a spin reorientation under the sample dilatation or compression as effect of an axial applied stress. Based on this assumption, an estimation of

the magnetostrictive effect can be realized via Mossbauer measurements at different temperatures.

Conclusions

Particular magnetic characteristics were observed for RE-Fe and RE-Fe-B thin films and ribbons, induced by size effects and by the preparation method. Unusual spin configurations were observed in systems presenting random magnetic anisotropy. The existence of amorphous phases is necessary for the appearance of random magnetic anisotropy with the amorphous phases supported by appropriate B inclusions.

The coupling of Gd with Fe is a simple antiferromagnetic one, whereas the coupling of anisotropic RE elements (Dy and Sm) with Fe has been proven to be of sperimagnetic type in thin films, in spite of the fact that Sm and Dy are light and heavy RE elements, respectively. The simple antiferromagnetic coupling of Fe and Gd leads to the idea of magnetization compensation at a certain concentration which can be easily estimated if the magnetic moments of the elements is known. For the sperimagnetic systems with antiferromagnetic coupling of Fe and RE, it is also possible to define a compensation concentration, possible to be calculated only if the angular aperture of the cones in which the Fe and Dy magnetic moments are distributed is known.

The magnetic moment of these type of alloys is very sensitive at concentration changes, especially in Fe-Gd and Fe-Dy thin films, a concentration range of maximum 10 % being identified to be responsible for a strong variation of the magnetic moment of Fe.

Fe-Dy-B and Fe-Sm-B ribbons with the same concentration ratio of Fe to RE as in the thin film counterpart were studied. The reduction of the hyperfine field with respect to metallic Fe is also evidenced in these system, but it should be noted that in the case of B containing alloys, the charge transfer at the overlapped "4s" and "3d" orbitals of Fe comes mainly from B atoms. A new methodology to investigate magnetostrictive aspects was developed in the particular case of Fe-Dy-B ribbons. Magnetostrictive aspects were studied by measuring spins rotation at varying temperatures via Mossbauer spectroscopy. Such effects were found to depend strongly on the RE content.

Taking into account the diverse functionalities of these systems (magneto-optical, magnetoresistive and magnetostrictive), RE-Fe systems with isotropic and anisotropic RE elements are of interest with respect to fundamental and applied studies, especially due to a high ability to control the involved magnetic spin structures. For a full characterization of spin structures in RE-Fe systems, the angular aperture and the orientation of the spins dispersion cone should be determined.

Acknowledgements: This work was supported by the Romanian Ministry of Research via the Core Program PN21N, PN-III-P1-1.2-PCCDI-2017-0871, Core Program PN19-03 (contract no. 21 N/08.02.2019) and POC P_37_697 REBMAT (contract 28/01.09.2016).

References

- [1] D. H. Rhyan, L.X. Liao, Z. Altounian, *Solid State Commun.*, 66 339 (1988)
- [2] J. J. Rhyne, J. H. Schelleng, N. C. Koon, *Phys. Rev. B*, 10 11 (1974)
- [3] Y. Mimura, N. Imamura, T. Kobayashi, *Journal of Applied Physics* 47, 368 (1976)
- [4] P. Chaudhari, J.J. Cuomo, R. J. Gambino, *Appl. Phys. Lett.* 22, 337 (1973)
- [5] Y. Yang, R. B. Wilson, J. Gorchon, C.-H. Lambert, S. Salahuddin, J. Boko, *Sci. Adv.* 2017; 3:e1603117
- [6] R. Hasegawa, *Journal of Non-Crystalline Solids*, 287 (2001) 405-412
- [7] A. Chung, J. Deen, J. S. Lee, M. Meyyappan, *Nanotechnology* 21, 412001 (2010)
- [8] S. S. P. Parkin, M. Hayashi, L. Thomas, *Science* 320, 190 (2008)
- [9] S. Mangin et al., *Nature Materials*, 13 286–292 (2014)
- [10] V. N. Gridnev, *J. Phys.: Condens. Matter* 28 476007 (2016)
- [11] R. Harris, M. Plische, M. J. Zukermann, *Phys. Rev. Lett.*, 31, (1973) 160
- [12] Chudnovsky et al. *Phys. Rev. B*, 33 (1986) 251
- [13] J. M. D. Coey, P. W. Readmann, *Nature* 246 (1973)
- [14] J. M. D. Coey, *J. Appl. Phys.* 49, 3 (1978)
- [15] Y. Kakehashi, *Modern theory of magnetism in metals and alloys, Magnetism of amorphous metals and alloys*, (M. Cardona P. Fulde K. von Klitzing R. Merlin H.-J. Queisser H. Störmer, series editors) Springer-Verlag Berlin Heidelberg (2012)
- [16] V. Kuncser, Thesis, Inst. of Atomic Physics, Bucharest, Romania, (1995)
- [17] N. Ymamura, T. Kobayashi, *J. Phys. Soc. Japan, Letters*, 39, 3 (1975) 829-830
- [18] R.C. Taylor, *Journal of Applied Physics*, 47, 3 (1976) 1164-1167
- [19] M. Ding, S. J. Poon, *Journal of Magnetism and Magnetic Materials* 339 (2013) 51–55
- [20] G. Filoti, V. Kuncser, M.D. Serbanescu, A. Jianu, L. Cristea, M. Nogues, J. L. Dormann, J. Maknani, *IEEE TRANSACTIONS ON MAGNETICS*, 29, 6, (1993) 3123-3125
- [21] V. Kuncser, G. Filoti, M.D. Serbanescu, A. Jianu, L. Cristea, J.L. Dormann, M. Nogues, J. Maknani, *Hyperfine Interactions*, 94 (1994) 2323-2326
- [22] M. Morariu, D.P. Lazar, A. Galatanu, N. Plugaru, V. Kuncser, G. Filoti, G. Hilscher, A. Kottar, *Journal of Alloys and Compounds* 285 (1999) 37–47
- [23] M. Seqqat, M. Nogues, O. Crisan, V. Kuncser, L. Cristea, A. Jianu, G. Filoti, J.L. Dormann, D. Sayah, M. Godinho, *Journal of Magnetism and Magnetic Materials* 157/158 (1996) 225-226
- [24] R.A. Brand, *Nucl. Instruments Methods Phys. Res. Sect. B Beam Interact. with Mater. Atoms.* 28 (1987) 417–432
- [25] N. N. Greenwood, T. C. Gibb, *Mossbauer Spectroscopy*, Chapman and Hall Ltd, London (1971)
- [26] X. M. Cheng, S. Urazhdin, O. Tchernyshyov, C. L. Chien, *Phys. Rev. Letters*, 94, (2005) 017203 1-4

**Superposed Shape Memory and Magnetocaloric Effects of NiFeGa Heusler alloys.
Effects of thermal treatments and of Co and Al Substitutions.**

F. Tolea, M. Sofronie, A.D. Crisan, B. Popescu, M. Tolea

National Institute of Materials Physics, POB MG-7, 77125 Bucharest-Magurele, Romania

Abstract. NiFeGa alloys with Co and Al substitutions, prepared as melt-spun ribbons, subjected to thermal treatment, with sequential but close structural and magnetic phase transitions were obtained in order to study the superposed shape memory and magnetocaloric effects. X-ray diffraction, differential scanning calorimetry, magnetic characterizations and magnetocaloric effect evaluation have been performed in this respect. The results highlight the role of substitutions and thermal treatments on the shape memory and magnetocaloric effects.

1. Introduction

The functionality of ferromagnetic shape memory alloys (FSMA) is related to the simultaneous presence of structural thermo-elastic transition and the ferromagnetic one. The martensitic transformation (MT) and magnetic order-disorder transformations temperatures may be tailored by doping the alloys with other elements (to change the electronic concentration, e/a) or by suitable thermal treatments (to improve crystallinity) so that, alloys with concomitant or sequential structural and magnetic phase transition may be obtained. Recent studies [1, 2] have shown that the entropy change associated to the martensite transformation in FSMA increase as the temperature difference between T_c and T_M decreases. As effect of coupling between the structural and magnetic transitions (magnetostructural coupling) a giant magnetocaloric effect (MCE) is expected, promoting these alloys as potential performing magnetic refrigerant materials. Also, transport properties depending on crystal structure and phase transformations may offer another possibility for practical use of FSMAs: actuators, displacement/force sensors, and motion dampers. MCE in Ni-Fe-Ga alloys was also investigated because ductility is an important issue in the application of FSMA as magnetocaloric materials.

The magnetocaloric effect is an intrinsic property of some magnetic materials associated with the phonon and magnetic excitations. The MCE around room temperature is an environmentally friendly alternative to conventional refrigeration and the most significant effect occurs at temperatures near magnetic transitions, and strongly depends on the type

of transition being highest for first-order transitions [3], which motivated the quest for FSMA with identical –or close- magnetic and structural transformation temperatures. The martensitic phase in the ferromagnetic off-stoichiometric Heusler alloy Ni-Fe-Ga features structural twinning, with exceptional magnetoelastic properties which recommend it as a good candidate to replace the brittle Ni-Mn-Ga [4, 5, 6] in various applications.

Numerous substitutions have been tested on Ni-Fe-Ga alloys in order to increase the Curie temperature (T_c), magneto-crystalline anisotropy or the mechanical properties. Morito et al. [7], found that the addition of Co in Ni-Fe-Ga increases the magnetocrystalline anisotropy energy and the Curie temperature, while the MT is around room temperature. These findings motivated our study of different substitutions possibly of fundamental but also applicative interest.

In the present work we investigate the influence of Co and Al substitutions on the MT, magnetic properties and MCE characteristics of NiFeGa Heusler FSMA, in ribbons prepared by melt spinning method and subjected to different thermal treatments. X-ray, DSC, magnetocaloric characterizations have been performed. It is assumed that the thin melt-spun ribbons assure a more efficient heat transfer, which is another motivation of our study.

2. Experimental results

We selected alloys with different nominal composition: $\text{Ni}_{52}\text{Fe}_{20}\text{Co}_2\text{Ga}_{26}$, $\text{Ni}_{52}\text{Fe}_{20}\text{Co}_2\text{Ga}_{23}\text{Al}_3$, $\text{Ni}_{52}\text{Fe}_{20}\text{Co}_3\text{Ga}_{23}\text{Al}_2$ and $\text{Ni}_{52}\text{Fe}_{20}\text{Ga}_{23}\text{Al}_5$, denoted: **Co2**, **Co2Al3**, **Co3Al2** and respectively **Al5**, in order to highlight the role of magnetostructural coupling. Ingots were prepared from high purity elements, by arc melting under argon protective atmosphere. Subsequently, they were inductively melted in quartz tubes under argon atmosphere and rapidly quenched by melt spinning technique (Buhler Melt Spinning Device). Ribbons of about 30 μm thickness and 2-3mm width were obtained at a copper wheel velocity of 20m/s in conditions of 40 kPa Ar overpressure and nozzle diameter of crucible of 0.5 mm. The “as quenched” melt spun ribbons (denoted as AQ) were subsequently subjected to thermal annealing at relatively Low Temperature (LT) at 400°C for 10 minutes and High Temperature (HT) for 2minutes at 900 °C, in vacuum quartz ampoules followed by rapid cooling in ice water.

The crystalline structure investigations were done by X-ray diffraction (XRD) using a Bruker D8 Advantage diffractometer in Bragg-Brentano geometry with Cu $K\alpha$ radiation, at room temperature (RT). The phase transformation temperatures and the MT enthalpy were determined by using a differential scanning calorimeter (DSC) model 204 F1 Phoenix (Netzsch), within a scanning rate of 20 K/min, under He protective atmosphere. Magnetic measurements below 350 K were performed with a

3. Results and Discussions

3.1. Structural characterization

The XRD pattern recorded at RT on Co2_AQ ribbons is highlighting the coexistence of the martensitic phase highlighted by modulated tetragonal structure with austenitic phase, characterized by the disordered B2 structure. The Co2Al3_AQ ribbons shows only peaks belonging to austenite B2 structure, suggesting the martensitic transformation below RT. Co2_LT sample show the reflections corresponding to the ordered L2₁ cubic austenite-specific structure of Heusler alloys, while Co2Al3_LT remains austenitic with B2 structure. At RT the sample Co3Al2_AQ is in the martensitic state, and the main reflections may be indexed as a modulated 7M type orthorhombic structure, after LT treatment Co3Al2 has the same layered martensitic structure (Fig.1a). Except the Al5 alloy (which retains a body-centered-cubic (b.c.c.) structure even on thermally treated samples – Fig.1b), HT heat treatment causes segregation of the secondary γ phase with the face-centered-cubic (f.c.c.) structure. HT thermal treatment has also the effect of the decrease in MT temperatures. Therefore Co3Al2_ HT diffractogram performed at RT brings out coexistence of γ phase with B2 austenite.

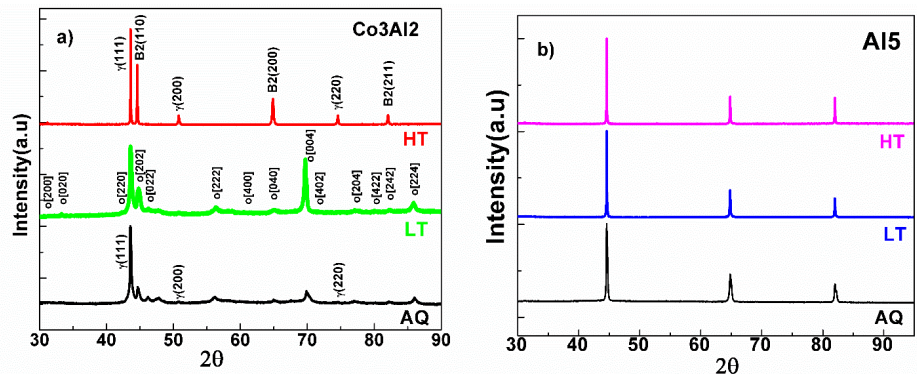


Fig.1 a) The XRD pattern recorded at RT of the Co3Al2 AQ, LT and HT thermally annealed ribbons. B) The same for the Al5 ribbons.

It can be seen that the precipitation of the γ phase is inherently found for Ni-Fe-Ga alloys with $Ga \leq 27\%$ at, because this composition is located in the $\beta+\gamma$ two phase zone. This phase is responsible for the improved ductility of Ni-Fe-Ga based alloys and is located mainly at the grain boundaries.

3.2. Calorimetric data

From the analysis of structural and DSC data (Fig.2) results that characteristic temperatures of martensitic transformation are strongly influenced by the substitutions. It is known that the valence electrons concentration (e/a) has a direct effect on the MT temperature, making it insightful to compare alloys in which the same e/a value is obtained by different substitutions. The general trend is to decrease martensitic transformation temperatures with decreasing the concentration of valence electrons. However, Co_2 and Co_2Al_3 ribbons shows the same 7.76 value for e/a (Fig.2a), but a significant decrease of the MT temperatures occurs replacing 3 Ga atoms with Al. This is probably an atomic size effect.

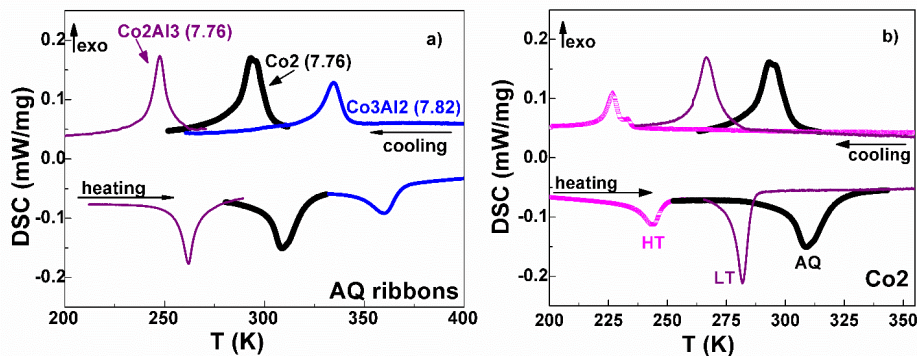


Fig.2 a) DSC data for AQ ribbons, and b) for Co_2 thermally treated ribbons.

The alloy Al_5 has $e/a=7.64$ (see the Table1), so a MT would be at very low temperatures and therefore was not registered by DSC. As it shows Fig.2b, the calorimetric scans reveal that TTs induce changes of the transformation heat (associated with the DSC peak area) and a decrease of the MT temperatures.

Table 1. The martensitic transformation characteristic temperatures - martensite start (Ms) and finish (Mf), austenite start (As) and finish, (Af) from DSC, the average transformation heat Q (calculated as average between the direct and reverse transformation) and the Curie temperature Tc for studied samples AQ, LT and HT thermal treated ribbons. Magnetic entropy variation ΔS .

| Sample | Ms (K) | Mf (K) | As (K) | Af (K) | Tc (K) | Q (J/g) | ΔS (J/KgK) in 4T |
|-----------|--------|--------|--------|--------|--------|---------|--------------------------|
| Co2_AQ | 308 | 277 | 296 | 326 | 360 | 3.6 | |
| Co2_LT | 282 | 252 | 268 | 287 | 370 | 2.6 | -2.2 |
| Co2_HT | 236 | 218 | 233 | 250 | 340 | 2.14 | |
| Co2Al3_AQ | 261 | 230 | 250 | 276 | 350 | 2.5 | -1.6 |
| Co2Al3_LT | 253 | 224 | 254 | 268 | 365 | 2.74 | -0.86 |
| Co2Al3_HT | 174 | 104 | 147 | 206 | 340 | 0.15 | |
| Co3Al2_AQ | 344 | 320 | 345 | 370 | 370 | 2.0 | -1.9 |
| Co3Al2_LT | 335 | 304 | 330 | 360 | 383 | 0.85 | |
| Co3Al2_HT | 162 | 98 | 154 | 191 | 365 | | |
| Al5_AQ | - | - | - | - | 295 | - | - |

3.3 Magnetic properties and MCE evaluation

The thermal hysteresis, specific for SMAS, shows in the thermo-magnetic curves in the range of MT. The temperatures characteristic of MT: martensite start (Ms), martensite final (Mf) austenite start (As) and austenite finish (Af) temperature were evaluated by the tangential method as shown in Fig 3a. The difference of the hysteresis shapes proves differences in magnetization and magnetocrystalline anisotropy of samples with different substitutions (Fig.3a). With respect to the magnetic behavior of Co3Al2 AQ and TT ribbons, Fig.3b shows the temperature dependence of magnetization, recorded in low magnetic field. Comparatively to the AQ alloys, the Curie temperature for annealed at LT ribbons is slightly higher reflecting a higher atomic order and the relaxation of the quench-in strains induced by the processing route. HT annealed samples show the thermal hysteresis accompanying the MT is sifted to lower temperatures.

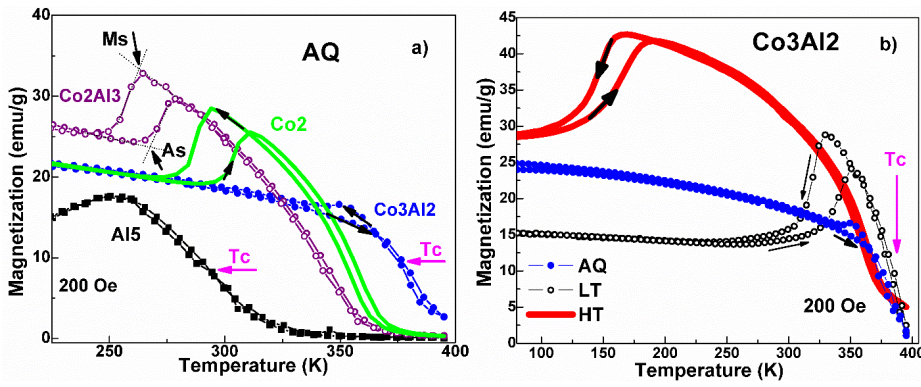


Fig.3 a) The Martensitic transformation reflected by the thermo-magnetic scans at low magnetic fields on AQ ribbons; b) the same for Co3Al2.

It is to be noted that the HT thermal treatment does not produce a further increase of the magnetic ordering temperature (T_c). The precipitation of the secondary γ phase counterwork the effect of further structural refinement and lattice relaxation and depletes the matrix in 3d elements, inducing also a decrease of T_c . Also, is observed on HT annealed sample a residual magnetization for $T > 400^\circ\text{C}$, proving a higher Curie temperature of the γ secondary phase.

By comparing DSC and thermo-magnetic results, the Co3Al2_AQ ribbons exhibit coupled magnetic and structural transitions. Also, Co2 ribbons seems to have consecutive and close magnetic and structural transitions. Materials with concomitant structural and magnetic transitions are expected to have a large entropy variation and be attractive by an important magnetocaloric effect.

In the following we will present the evaluation of the magnetocaloric effect on the discussed samples, less Al5 alloy not showing MT, in a range of temperature ($< 380\text{K}$) that allowed full characterization of magnetic alloy with SQUID device.

In order to quantitatively characterize the MCE, an indirect technique to evaluate the ΔS_m was used. According to Maxwell relation, ΔS_m can be calculated by means of magnetic measurements:

$$\Delta S_m(T, H) = \int_0^H (\partial M / \partial T)_H dH, \quad (1)$$

whose discrete data points version (for isotherms measured at certain field only) reads:

$$\Delta S_m = \sum_n \frac{(M_{n+1} - M_n)}{(T_{n+1} - T_n)} \Delta H_n \quad (2)$$

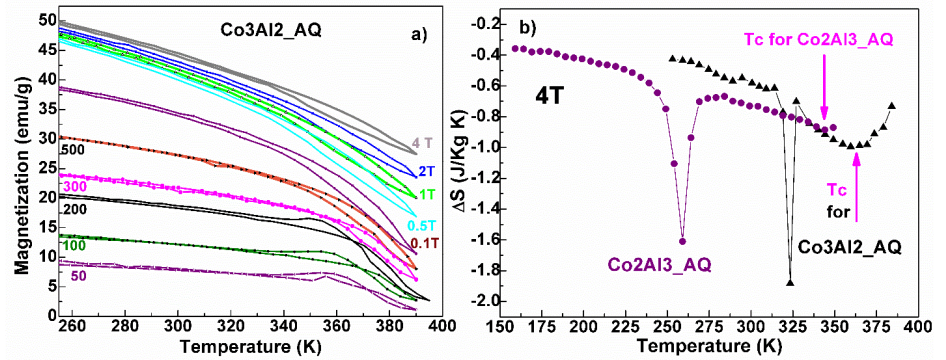


Fig.4 a) Isofield magnetization curves at different magnetic fields of Co3Al2_AQ ribbons. b) Entropy variations versus temperature for Co3Al2_AQ and Co2Al3_AQ ribbons.

The magnetization curves at different constant magnetic fields were used to evaluate the magnetocaloric effect of Co3Al2_AQ ribbons. Co3Al2_AQ ribbons seems to have, from thermos-magnetic measurements, a concomitant or sequential structural and magnetic phase transition. As shown in Fig. 4b, there are two peaks nearby in magnetic entropy variations versus temperature, so the transformations are very close, but we do not have a magneto-structural coupling. The change in entropy is higher in the MT area whereas the relative cooling power (RCP) (related to the peak area) is higher in Tc area (Fig.4b). For the structural transformation the AQ ribbons show $\Delta S = -1.9$ J/KgK. The entropy variations for Co3Al2_AQ throughout the MT is greater than value $\Delta S = -1.6$ J/KgK corresponding of Co2Al3_AQ, and this can be explained by the fact that MT and Tc are closer. In Fig.5a is represented the temperature dependence of the magnetic entropy change for Co2Al3_LT, in different constant fields. Although the contribution of magnetic transition to entropy variation consists of direct magnetocaloric effect ($\Delta S < 0$), a positive entropy change corresponding to the MT can be observed for applied magnetic field lower than 1 T. These non-conventional magnetocaloric effect is denoted as the inverse magnetocaloric effect (IMCE) and is highlighted in Fig.5b.

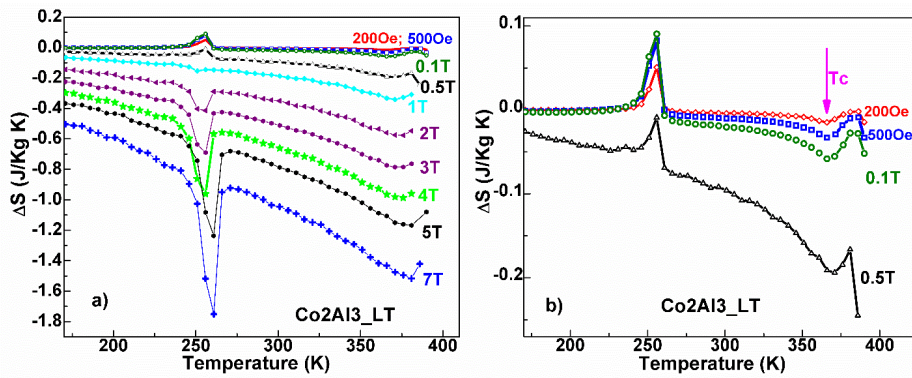


Fig.5a) Temperature dependence of the magnetic entropy change for Co₂Al₃_LT, in different constant fields. b) Inverse magnetic entropy change highlighted in small fields.

Inverse magnetocaloric effect often occur near phase transitions as a result of the strong interaction between magnetism and other degrees of freedom. The explanation of it was related to the strong uniaxial magnetocrystalline anisotropy of the martensitic phase. If the composition is varied so that the MT temperature approaches T_c temperature, the anisotropy is diminishing with a corresponding decrease of the inverse contribution and conventional behaviour becomes dominant. The magnetocaloric properties proved to be optimal when both martensitic and ferromagnetic transitions appear close to each other [8].

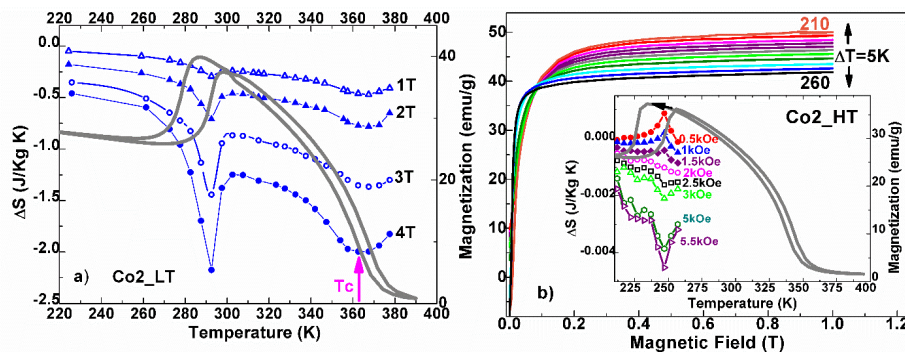


Fig.6 a) Temperature variation of magnetic entropy change and of magnetization measured in 200 Oe (with continuous line) on Co₂Al₃_LT. b) Magnetization curves at different constant temperatures (measured with 5K temperature increment). Insert: enlarged view of the thermomagnetic hysteresis and entropy variation versus temperature along the MT for Co₂_HT ribbons.

For annealed Co₂_LT sample, note the occurrence of two maximum magnetic contributions to entropy, the left one in the area of martensitic transformation and the second in the order-disorder magnetic transition temperature ranges (Fig.6a). And the Co₂_LT sample has the change in entropy higher in the MT area, whereas the refrigerant capacity (related to the peak area) is higher in T_c area. We have obtained a value of 2.2 J/KgK for the entropy change in Co₂ alloy, but estimate that by further tailoring the alloy composition and using proper thermal treatments to tune the magnetic and structural transition temperatures closer (or even concomitant) this value may be improved. Magnetization isotherms in 1T maximum applied field (measured with 5K temperature increment) (Fig.6b) were used to evaluate the magnetocaloric effect of Co₂_HT sample. Entropy variations versus temperature are shown in the inset of Figure 4b. In this case, the inverse magnetocaloric effect is also present in small magnetic fields.

We obtained rather small values of the magnetic entropy variation (due to the small variation of the magnetization with the temperature and the fact that the transition is not abrupt, there are magnetic and orderly fluctuations at short distance and after T_c) and therefore the main relevance of our results remains at the fundamental level, highlighting the importance of the magnetostructural coupling.

4. Conclusions

We have studied the effect of Co and Al substitutions on the magnetocaloric properties of NiFeGa ferromagnetic shape memory alloys. The alloys were prepared as melt-spun ribbons - an unconventional preparation route that also allows subsequent tuning of the stress release and crystallites growth by thermal treatment.

Co₂, Co₂Al₃ and Co₃Al₂ samples presented reversible thermo-elastic transformations. As a general rule, the martensitic transformation temperatures and the enthalpies decrease with increasing the temperature of the thermal treatments (on the melt-spun ribbons).

Al₅ sample does not undergo MT.

Importantly however, by tuning the alloys composition via substitutions, one can get close to a concomitant magnetic and structural transformation leading to an optimum magnetocaloric effect.

The highest magnetic field induced entropy variation was found for the Co₂_LT ($\Delta S_m = 2.2$ J/KgK), being associated with the fact that the magnetic and structural transitions are in the closest vicinity.

For Co₂_HT and Co₂Al₃_LT with the MT temperature much lower than T_c, a positive entropy change corresponding to the MT can be

observed for applied magnetic field lower than 1 T, meaning an inverse magnetocaloric effect (IMCE).

References

- [1] Recarte V, Perez-Landazabal J.I, Gomez-Polo C, Cesari E, Dutkiewicz J, J. Mag. Mat. **310** e999-e1001 (2007).
- [2] C. Seguí, E.Cesari, Intermetallics **19** 721-725 (2011).
- [3] Pecharsky V K, Gschneidner K A Jr.; Phys. Rev. Lett. **78**, 4494 (1997).
- [4] Okumura H, Uemura K, J. Appl. Phys **108**, 043910 (2010).
- [5] Recarte V, Pérez-Landazábal J I, Gómez-Polo C, Cesari E, Dutkiewicz J, Appl. Phys. Lett. **88**, 132503 (2006).
- [6] Sofronie M, Ţolea F, Kuncser V, Valeanu M, J. Appl. Phys. **107**, 113905 (2010).
- [7] H. Morito, K. Oikawa, A. Fujita, K. Fukamichi, R. Kainuma, K. Ishida, T. Takagi, J. Mag. Mat. **290-291**, 850 (2005).
- [8] Planes A, Mañosa L and Acet M, J. Phys.: Condens. Matter **21** 233201 (29pp) (2009).

Interface state densities in different heterojunctions

N. Novkovski^{1,2}, A. Paskaleva³, A. Skeparovski¹, and D. Spassov³

¹*Institute of Physics, Faculty of Natural Science and Mathematics, Ss. Cyril and Methodius University, Arhimedova 3, 1000 Skopje, Macedonia*

²*Research Center for Environment and Materials, Macedonian Academy of Sciences and Arts, Skopje, Macedonia*

³*Institute of Solid State Physics, Bulgarian Academy of Sciences, 72 Tzarigradsko Chaussee blvd., 1784 Sofia, Bulgaria*

Abstract: Interface states at the contact between the dielectric and semiconductor substrate substantially influence the characteristics of electron devices containing various metal-insulator-semiconductor (MIS) structures. Several methods of determination of the distribution of interface states through the bandgap are used in characterization of microelectronic devices. Downscaling of dielectric stacks required for novel technologies, introduces several effects causing the standard methods to be not enough efficient.

Here we pay particular attention to the Terman method, reconsidering its foundations in the case where quantum charge in silicon near the interface with dielectric has to be taken into account.

In this work we attempt to describe C - V characteristics of MIS structures using analytical expression containing parameters that can be empirically extracted from the measured C - V characteristics, and thus extract interface states density distributions excluding the effect of quantum charge.

Successful application of the method has been demonstrated on various MIS structures.

PACS: 73.20.-r, 73.40.Qv, 77.55.+f,

1. Introduction

Ultrathin dielectrics (of order of 10 nm or thinner) with outstanding dielectric properties are of particular importance for modern microelectronic devices, such as MOSFET, Dynamic Random Access Memories (DRAM) and charge trapping flash memories. Classically used silicon dioxide layers are nowadays replaced in majority of the applications by high permittivity (high- κ) dielectrics. Mixed and stacked layers are quite often used as optimized solutions for obtaining required properties of the stacked dielectric. For illustration, schematic presentation of charge trapping flash memory is shown in figure 1.

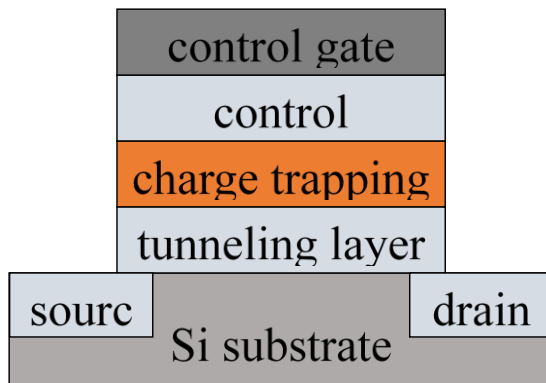


Figure 1. Schematic presentation of charge trapping flash memory.

Charges of various origins affect substantially the properties of the structures containing such ultrathin dielectrics. These charges can be ones initially existing in the structures, both as imperfections of the composed structures (i.e. lattice mismatch between two subsequent layers) or as defects created by the fabrication process. Other charges can be creation during the use of the structures, mainly as a result of electrical stresses or radiation (stress generated).

Particular attention is paid to the charges connected to the presence of localized energy states in the forbidden gap of the semiconductor substrate originating from defects in the dielectric close to the interface with the silicon substrate. They are named interface states and the charge captured on them usually known as interface charge. This charge varies with the applied voltage on the structure, thus resulting in some kind of instability. Therefore, the precise determination of the distribution of these states over the forbidden gap of the semiconductor (interface state density, D_{it}) is an important issue in the characterization of ultrathin dielectrics and devices including such films.

In this work we study the issue of location and character of interface states in various heterostructures used in contemporary microelectronic devices which include nanosized dielectrics.

2. Peculiarities of high permittivity dielectrics

High- κ materials are considered as efficient replacement of classically used SiO_2 in nanoelectronics. They have substantially higher value of relative permittivity (ϵ_r) than SiO_2 (3.9), thus allowing obtaining required capacitances of metal-insulator-semiconductor structures in the devices with substantially higher physical thickness than in the case of SiO_2 layers, thus limiting the leakage currents due to direct tunneling present in extremely thin SiO_2 films (<4 nm). Between the high- κ materials are: HfO_2 , Ta_2O_5 , Al_2O_3 , ZrO_2 , Al_2O_3 , La_2O_3 etc. Relative permittivity values for these

materials are dominantly between 10 and 30, while the bandgap values are higher than 4 eV and lower than 9 eV (the value for SiO₂). These values reside between the upper limit for wide bandgap semiconductors (from 2 eV to 4 eV) and that of the typical dielectric SiO₂. TiO₂ is also considered as high- κ **Error! Reference source not found.**, even if its bandgap value is only 3.2 eV.

While SiO₂ exhibits rather low density of defect, due to its particular structure, high- κ dielectrics have substantially larger defect densities, leading to dominant defect related conduction mechanisms, mainly Poole-Frenkel field enhanced thermal emission of electron from traps **Error! Reference source not found.**

Another feature of high- κ dielectrics is the presence of an interfacial layer (typically between 1 nm and 4 nm thick) between it and the semiconductor substrate **Error! Reference source not found.** **Error! Reference source not found.** Presence of such a layer substantially modifies the characteristics of the devices, as regard to the case of single dielectric layer. Dielectric stack high- κ /interfacial layer is to be considered instead of single dielectric layer. In the case of silicon substrate, an ultrathin SiO₂ layer is formed. Leakage currents for metal-insulator-semiconductor structures can be determined using the model that we described in details in **Error! Reference source not found.** It has been shown that interfacial layer plays important role in the determination of the properties **Error! Reference source not found.** of the stack, and optimization of the thicknesses ratios in the stack allows benefiting from the high effective dielectric permittivity simultaneously with low level of leakage currents.

3. Modified Terman method for determination of D_{it}

Several methods of determination of the distribution of interface states over the forbidden gap of the semiconductor have been developed and are in use for characterization of microelectronic devices **Error! Reference source not found.** **Error! Reference source not found.** **Error! Reference source not found.** In **Error! Reference source not found.** we discussed the issue of their applicability in the case of nanosized high- κ dielectrics. Based on our results for structures containing high- κ dielectric **Error! Reference source not found.**, it was concluded that serial C - R measurement mode is more convenient for characterization of such structures than the dominantly used parallel one. Further refinement of the results is obtained using correction method for measured C - V and G - V curves at a given frequency (f) for the effect of leakage currents and serial resistance **Error! Reference source not found.**

Terman method using single C - V curve has several advantages over the other methods considered for determination of the distribution of interface states. The main advantage is that the complicated effects of leakage currents on the characteristics at lower frequencies are avoided.

The main question arising in connection to the results obtained by this method is whether the results for nanosized dielectrics are equally correct as in the case of dielectrics with thicknesses > 10 nm. In this paper we discuss the issue of the effect of quantum charge in structures containing nanosized dielectrics. In addition, we attempt to clarify the known issue of the nature of exponential tails in the distribution towards the band edges. New results for nanosized dielectrics allow us to reconsider this issue from a new viewpoint. Based on all results, discussion on the origin and location of interface charges is provided.

When voltage is applied on the structure, bending of zones in semiconductor occurs, leading to the formation of a quantum well in semiconductor at the interface with the dielectric (figure 2). At positive gate electrons occupy states in the well, while at negative gate, holes. This results with presence of quantum charge (Q_q) in the structure located in semiconductor substrate near the interface with the dielectric.

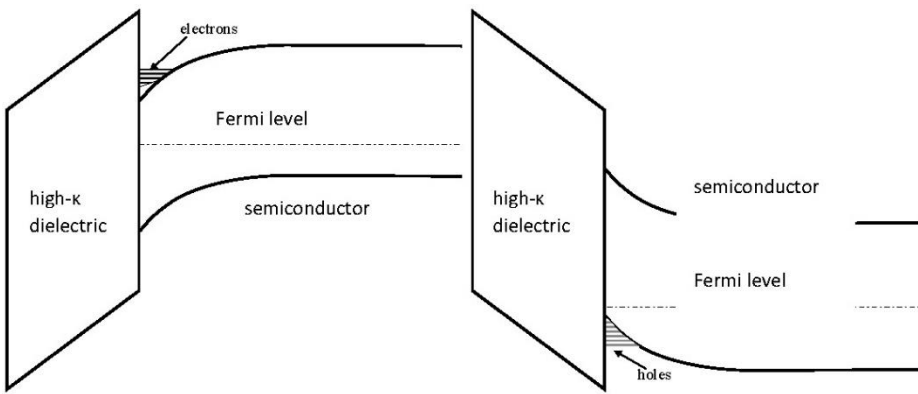


Figure 2. Quantum charge for positive (a) and negative gate (b).

As we shown in **Error! Reference source not found.**, the voltage on the structure (gate voltage) in the presence of a quantum charge ($V_{g,q}$) is:

$$V_{g,q} = V_{ox,q} + V_{fb} + V_s = V_{ox} + V_{fb} + V_s + \frac{d_{ox}}{\epsilon_{ox}} Q_q = V_g + \frac{d_{ox}}{\epsilon_{ox}} Q_q, \quad (1)$$

where $V_{ox,q}$ is the voltage on the dielectric layer along with the voltage drop on the quantum charge region, V_{fb} is the flatband voltage, V_{ox} is the voltage on the dielectric layer itself and V_s is the surface potential in the semiconductor substrate, d_{ox} is the dielectric layer thickness and ϵ_{ox} is its permittivity. V_g is the voltage that will be obtained on the structure in the absence of quantum charge:

$$V_g = V_{ox} + V_{fb} + V_s. \quad (2)$$

Surface potential is determined using following implicit relation **Error! Reference source not found.:**

$$V_s = V_g - V_{fb} - \frac{\epsilon_s}{\epsilon_{so}} \left(\frac{2kT}{q} \frac{p_0}{\epsilon_s} q \right)^{1/2} d_{eq} \left(\exp\left(\frac{-qV_s}{kT}\right) + \frac{qV_s}{kT} - 1 + \left(\frac{n_i}{p_0}\right)^2 \left(\exp\left(\frac{qV_s}{kT}\right) - \frac{qV_s}{kT} - 1 \right) \right)^{1/2} \quad (3)$$

where ϵ_s is the dielectric permittivity of the semiconductor substrate, p_0 is the majority carrier density (holes in p-type), n_i is the intrinsic carrier concentration in the semiconductor, k is the Boltzmann constant, q is the electron charge, T is the absolute temperature and d_{eq} is the equivalent oxide thickness determined as:

$$d_{eq} = \frac{\epsilon_{so}}{C_{ox}} S, \quad (4)$$

where S is the electrode area and C_{ox} is the capacitance of the insulating layer itself.

Energy position inside the semiconductor bandgap (E), corresponding to given V_s , is calculated as

$$E = qV_s + kT \ln\left(\frac{p_0}{n_i}\right). \quad (5)$$

As we found in **Error! Reference source not found.**, for high- κ dielectrics with equivalent thicknesses as low or lower than 6 nm, for the quantum charge an expression of the following type can be used:

$$Q_q = k_q \frac{\epsilon_{ox}}{d_{eq}} V_{ox}, \quad (6)$$

where k_q is a proportionality factor having value close to 1.

In the standard Terman method ideal C - V curve **Error! Reference source not found.** without taking into account quantum change (QC) is used as reference curve ($V_{g,id}$, figure 3, dotted line). Stretch-out of the measured (V_g , figure 3, solid line) compared to the ideal C - V curve (ΔV_g) is further determined for each measurement point.

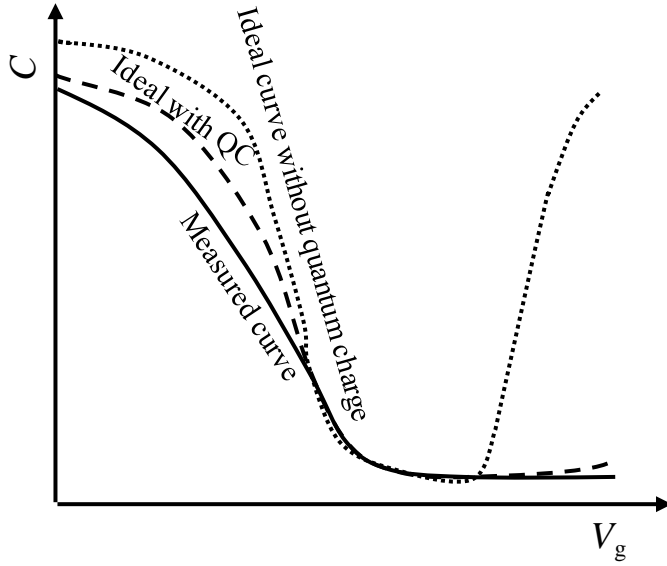


Figure 3. Curves used in Terman method.

In the standard method, following expression is used for determination of interface state densities:

$$D_{it} = D_{it}(V_s) = \frac{C_{ox}}{q^2 S} \frac{d(V_g - V_{g,id})}{dV_s} = \frac{C_{ox}}{q^2 S} \frac{d\Delta V_g}{dV_s}, \quad (7)$$

In our modified method, correction for the quantum charge is done using expression (1). Thus obtained C - V curve with QC is also shown in figure 3 (dashed line). Then, the interface state densities are determined as

$$D_{it} = D_{it}(V_s) = \frac{C_{ox}}{q^2 S} \frac{d(V_{g,q} - V_{g,id})}{dV_s} = \frac{C_{ox}}{q^2 S} \frac{d\delta\Delta V_g}{dV_s}, \quad (8)$$

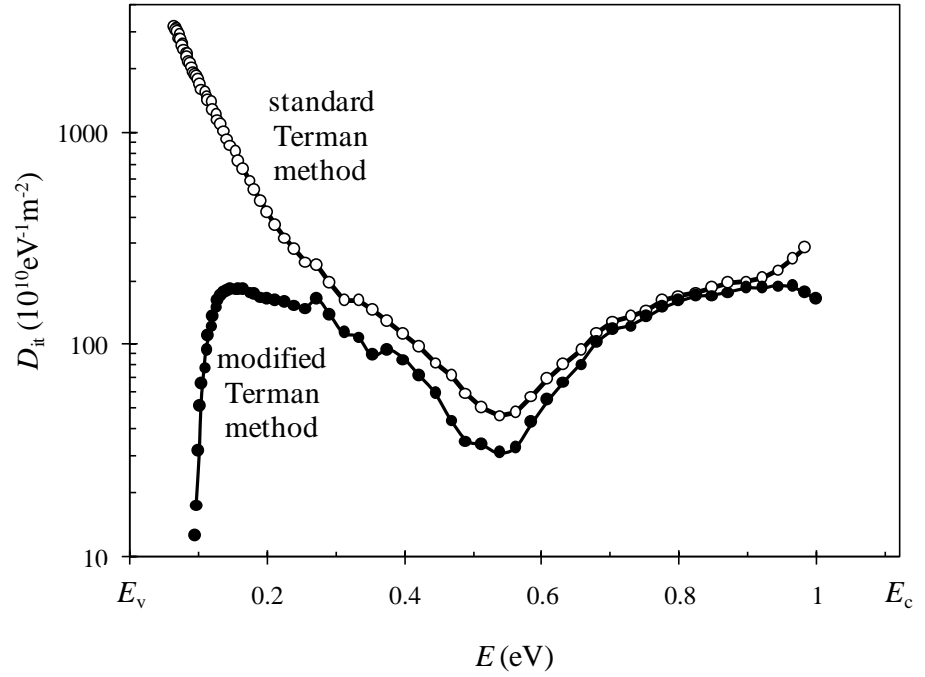


Figure 4. Distributions of interface state densities obtained by standard and by modified Terman method over the silicon forbidden gap, between the top of the valence band (E_v) and the bottom of the conduction band (E_c).

In figure 4 an example is shown with results obtained by standard and modified Terman method for metal-insulator-silicon structures containing atomic layer deposited multilayered $\text{HfO}_2/\text{Al}_2\text{O}_3$ stacks studied in **Error! Reference source not found.** Standard method results in appearance of exponential tails towards the band edges. In the middle of the forbidden gap, the results obtained by these methods are comparable. Therefore, for usually used value of the interface state density at midgap, standard Terman method gives relatively correct value. However, for determination of total density (integrated D_{it} over the bandgap) and the precise shape of the distribution, modified method has to be considered. This issue will be discussed in the next section.

3. Discussion on the origin of exponential tails in distribution obtained by standard Terman method

Tails in the D_{it} distribution towards the band edges obtained by standard Terman method have been in many cases matter of debate. Although similar features are obtained while using the high-low frequency method **Error! Reference source not found.** **Error! Reference source**

not found., other more refined methods, such as: deep level transient spectroscopy (DLTS), three-level charge pumping and spectroscopic charge pumping, do not show such tails **Error! Reference source not found.** Indeed, tails have been observed using electron spin resonance (ESR) **Error! Reference source not found.**, but they are rather narrow compared to the tails obtained by standard Terman method. In some works the tails were attributed to the presence of continuum of states located near the band edges **Error! Reference source not found.** Our results obtained using modified Terman method suggest that these tails are most probably due to the contribution of the quantum charge in the Fermi level difference across the metal-insulator-semiconductor structure, and hence on the value of the measured gate voltage. Namely, additional voltage drop on the quantum charge region gives a contribution proportional to the oxide voltage, as expressed by equation (6). Thus, the value of D_{it} obtained by standard method is higher than the real one by:

$$D_{it,sc} \sim \frac{dV_{ox}}{dV_s}. \quad (9)$$

Electric field in the dielectric at the contact with the substrate is determined as **Error! Reference source not found.:**

$$E_{ox} = \frac{\epsilon_{Si}}{\epsilon_{ox}} \left(\frac{2kT}{q} \frac{p_0}{\epsilon_{Si}} q \right)^{1/2} \left(\exp\left(\frac{-qV_s}{kT}\right) + \frac{qV_s}{kT} - 1 + \left(\frac{n_i}{p_0}\right)^2 \left(\exp\left(\frac{qV_s}{kT}\right) - \frac{qV_s}{kT} - 1 \right) \right)^{1/2} \quad (10)$$

Close to the band edges, the expression (10) for E_{ox} can be approximated as follows

$$E_{ox} \approx \frac{\epsilon_{Si}}{\epsilon_{ox}} \left(\frac{2kT}{q} \frac{p_0}{\epsilon_{Si}} q \right)^{1/2} \begin{cases} \left(\frac{n_i}{p_0}\right) \exp\left(\frac{qV_s}{2kT}\right) & V_s \gg \frac{2kT}{q} \\ \exp\left(\frac{-qV_s}{2kT}\right) & -V_s \gg \frac{2kT}{q} \end{cases} \quad (11)$$

Therefore, close the both band edges,

$$E_{ox} \sim \exp\left(\frac{q|V_s|}{2kT}\right), \quad (12)$$

and hence

$$D_{it,sc} \sim \frac{dV_{ox}}{dV_s} \sim \frac{dE_{ox}}{dV_s} \sim \frac{d}{dV_s} \exp\left(\frac{q|V_s|}{2kT}\right) \sim \exp\left(\frac{q|V_s|}{2kT}\right). \quad (13)$$

Based on above, it is expected in the semi-log plot V_s - $\ln(D_{it})$ the values of the slopes of the tangents close to the band edges to be $2kT/q \approx 50$ mV at room temperature. In the semi-log plot E - $\ln(D_{it})$ the values of the slopes of

the tangents close to the band edges will be about 50 meV. The value obtained from the figure 4 close to the top of the valence band of about 55 meV is in accordance with the expected one. This is an additional proof that the tails are due to the quantum charge, rather than to real exponential distributions of interface states close to the band edges (continuum of states).

3. Discussion on the nature and location of interface traps

Observed maxima in D_{it} distribution obtained by modified Terman method (figure 4) are close to the values reported for peaks in EPR spectra of SiO_2 , 0.32 eV and at 0.83 eV, which have been attributed to P_b defects at the SiO_2 -Si interface **Error! Reference source not found.** In the first works P_b defect at the Si(111)/ SiO_2 interface, was described as oriented silicon dangling bond pointing out of the silicon into the oxide **Error! Reference source not found.** **Error! Reference source not found.** In **Error! Reference source not found.** two type of P_b defects have been identified: P_{b1} (similar to P_b) and P_{b0} (chemically different from to P_b). In theoretical studies three possible structures for P_{b1} defects have been proposed: strained dimmer model, oxygen bridge model and asymmetrically oxidized dimmer model **Error! Reference source not found.** Positions of each of the peaks for P_{b1} and P_{b0} are close to each other **Error! Reference source not found.**, and hence their individual effects in the hardly identified. Thus, on the E - D_{it} curves only two separate peaks due to P_b defects are observed.

We have obtained similar results for various dielectric stacks **Error! Reference source not found.** **Error! Reference source not found.** on silicon. Mainly two picks at around 0.3 eV and 0.9 eV above the top of the valence band are observed. The above finding indicates that the origin of interface states in various stacks is merely the same: P_b defects in SiO_2 at the interface if the dielectric with the silicon substrate. The reason for this is that only defects close to the substrate can be charged and discharged at low voltages used in C - V measurements.

Conclusions

Modified Terman method using single high-frequency C - V curve accounting for the effect of the quantum charge allows precisely determining the distribution of the interface states over the entire forbidden energy gap of the semiconductor. Even if the structure of the dielectric stack can be rather complicated, it appears that the dominant contribution in the interface state density is that of the P_b defects located in the interfacial layer close to interface with semiconductor surface.

Exponential tails appearing in the results obtained by the standard method appear to be an artifact of the method due to the neglecting of the effects of the quantum charge.

References

- [1] Zellag S., Dehimi L, Asar T, Saadoun A, Fritah A and Özçelik S 2018 *Appl. Phys. A* **124** 84
- [2] Chiu F C, Wang J J, Lee J Y, Wu C 1997 *J. Appl. Phys.* **81** 8911
- [3] Park I-S, Jung Y C, Lee M, Seong S and Ahn J 2014 *IOP Conf. Series: Materials Science and Engineering* **54** 012004
- [4] Alers G B, Werder, D J, Chabal Y, Lu H C, Gusev E P, Garfunkel E, Gustafsson T and Urdahl R S 1998 *Appl. Phys. Lett.* **73** 1517
- [5] Novkovski N and Atanassova E. 2006. *Appl. Phys. A* **83** 435
- [6] Novkovski N 2007 *AIP Conf. Proc.* **899** 83
- [7] Nicollian E H, Brews J R 1982 *MOS (Metal Oxide Semiconductor) Physics and Technology* (New York: Wiley)
- [8] Sze S M, Ng K K 2007 *Physics of semiconductor devices* (New York: Wiley)
- [9] Schroder D K 2006 *Semiconductor Material and Device Characterization* 3rd edn (New York: Wiley-Interscience/IEEE) p350
- [10] Novkovski N 2015 *Mat. Sci. Semicond. Proc.* **39** 308
- [11] Novkovski N, Atanassova E 2017 *Adv. Mater. Sci. Eng.* **2017** 9745934
- [12] Novkovski N 2015 *Mat. Sci. Semicond. Proc.* **39** 308
- [13] Novkovski N 2017 *J. Phys. Commun.* **1** 035006
- [14] Novkovski N, Paskaleva A, Skeparovski A and Spassov D 2018 *Adv. Cond. Matter. Phys.* **2018** 3708901
- [15] Atanassova E, Novkovski N, Paskaleva A, Pecovska-Gjorgjevich M 2002 *Solid State Electron.* **46** 1887
- [16] Novkovski N 2006 *Semicond. Sci. Technol.* **21** 945
- [17] Autran J L, Seigneur F, Plossu C, Balland B 1993 *J. Appl. Phys.* **74** 3932
- [18] Jock R M, Shankar S, Tyryshkin A M, He J, Eng K, Childs K D, Tracy L A, Lilly M P, Carroll M S, Lyon S A 2012 *Appl. Phys. Lett.* **100** 023503
- [19] Poindexter E H, Gerardi, G J, Rueckel, M E, Caplan, P J, Johnson N M, Biegelsen D K 1984 *J. Appl. Phys.* **56** 2844
- [20] Caplan P, Poindexter E, Deal B Razouk R 1979 *J. Appl. Phys.* **50** 5847
- [21] Brower K 1983 *Appl. Phys. Lett.* **43** 1111
- [22] Stathis J H, Dori L 1998 *Appl. Phys. Lett.* **58**, 1641
- [23] Stirling A, Pasquarello A 2005 *J. Phys.: Condens. Matter.* **17** S2099
- [24] von Bardeleben H J, Cantin J L 1997 *Braz. J. Phys.* **27** 314

Critical behavior of an anharmonic nanoscopic solid

C. Popa

Horia Hulubei Foundation, Magurele - Bucharest, Romania

June 27, 2019

Abstract

This paper is devoted to the mean field theory of structural phase transition of a model of anharmonic solid, with applications in nanophysics. The model consists in a rectangular lattice, in an arbitrary number of dimensions, of quantum anharmonic (quartic) oscillators, interacting with their nearest neighbors by elastic forces. The critical equation of the transition is obtained using the theory of dielectric susceptibility. In order to use a mathematically tractable model, the quartic potential - initially, a symmetric two well potential - is replaced by a similar, but workable one - a rectangular symmetric two well potential. For the energies and wavefunctions corresponding to lowest states we obtain accurate analytical approximations, which make possible the evaluation of the dipolar matrix elements, essential ingredients of the critical equation. A simple expression is obtained for this equation; its classical limit is also deduced. Our result is similar, in particular cases, with those obtained analytically by Scalapino and his co-workers and numerically by Bishop and Krumhansl. The applications in nanophysics are discussed.

1 Introduction

The anharmonic solid - and, particularly, the solid with ψ^4 anharmonicities - is a system of utmost interest in condensed state physics, both for fundamental, and for practical reasons. One of the very interesting problems in the context of the anharmonic solid is the structural phase transition. It is important not only from the perspective of its applications in ferroelectricity, but from the more general perspective of the theory of phase transitions. Actually, it provides a relatively simple model of such a transition, with real order parameter.

There are at least two approaches of this kind of phase transitions. In one of them, the starting point is the Ginzburg - Landau functional of free energy [1]; in the other one - a polynomial Hamiltonian [2], [3]. The statistical behavior of a n -dimensional solid described by a Ginzburg-Landau functional can be obtained using the transfer matrix theory [4], from the calculation of the energy

of the first levels of a Hamiltonian of a quantum $n - 1$ -dimensional system, with quartic anharmonicities. So, a classical system, in n spatial dimensions, is equivalent with a quantum system, in $n - 1$ -dimensions. These two systems, sometimes called dual systems, describe quite similar objects - aggregates of classical, respective quantum oscillators. A well-known example of such aggregates is that studied by Stoeckly and Scalapino [5], [6], where the evaluation of the partition function of a planar system of coupled chains, composed by quartic oscillators, is reduced to the study of a chain of quantum anharmonic oscillators. If the coupling between quantum oscillators is weak, the 1D Hamiltonian can be transformed in a fermionic Hamiltonian, similar to that obtained by Schultz, Mattis and Lieb, in their study devoted to the Ising [7], in various variants of the Luttinger model or in other 1D [8], [9], [10], [11]. These 1D systems have interesting theoretical and experimental applications, and it is useful to compare them with other exactly solvable atomic [12] or magnetic models [13]. Consequently, the ψ^4 anharmonic solid can be linked to a large class of models intensively studied in the theory of condensed matter, including the Ising model.

After remarkable theoretical progress, which produces, in the '70s, a lot of exact results, the following decades were dominated by numerical investigations, for instance [16], [17], [18]. In more recent papers, some authors use both numerical methods, and analytical approximations [19], [20], in order to obtain a better understanding of such systems. A model which extends the Ginzburg-Landau theory beyond the linear chain approximation was proposed for systems where both the nearest neighbor interaction and the near next neighbor interaction is taken into account [21]. The transfer matrix theory was applied in the analytic study of thermal or quantum phase transitions in low dimensional systems, in with or without external fields [24]. A critical analysis of these results was be done by Lungu [29].

If the aforementioned analytical results mainly refer to low dimensional systems, the 3D anharmonic systems were investigated with less rigorous theoretical methods, the most frequently used being the mean-field ones; actually, this situation is quite common in solid state theory. As it is well known, the mean fields approximations give good results for the structural phase transitions [2], [3]. The model to be discussed in this paper is a d -rectangular lattice of quantum anharmonic (quartic) oscillators, interacting by elastic forces with their nearest neighbors. In principle, the model can be studied for any value of d , but for $d = 1$, it gives incorrect results, including a spurious phase transition. Even if the model is a quantum one, the classical case can be easily obtained, taking the limit $\hbar \rightarrow 0$.

In this paper, we shall consider only the case of the real order parameter. The physics described by such a model of anharmonic solid is quite simple. In an one-dimensional picture, the particle situated in a lattice point can be placed in one of the two wells of the anharmonic potential, "to the left" or "to the right", if the magnitude of the well - having the dimension of an energy - is large enough, compared to the energy of thermal fluctuations. If one of these position is "preferred" by the particle, the system is in an ordered state;

if the positions are equivalent, the state is disordered. For shallow wells, the system can become "polarized", in the sense that the particles can "slip" in the same direction. In this case, a "soft mode transition" occurs, at a certain temperature. For deep wells, the system undergoes an order-disorder transition, and is equivalent to an Ising model. The interplay between temperature, particle mass, dimensionality and potential strength define the critical equation.

The main goal of this paper is to obtain an analytical approximation for the critical equation describing a model of quantum anharmonic solid in 2D or 3D. We shall follow a mean-field approach [19], [20], and we shall use, in order to get the critical temperature, a formula which requests the finding of the electrical susceptibility of the model [30]. We can use this formula only if we know the wave functions and the eigenenergies of the bound states inside the wells of the anharmonic potential, which has two minima. It is well-known that, in spite of its apparent simplicity, the problem defies an exact solution; more than that, the Rayleigh - Schrodinger perturbation series, in the coupling constant of the quartic term, diverges, for any of the bound states [31]; a quite recent review of the results obtained in this domain can be found in [32].

In order to obtain an analytic approximation, the quartic potential must be replaced with another one, more suitable to a simple treatment; a reasonable candidate is the symmetric double rectangular well. Actually, even this simpler problem cannot be fully treated analytically: the wave functions have a simple form, being combinations of exponentials with imaginary or real argument ($\exp(\pm kx)$, $\exp(\pm i\kappa x)$), but the wave vectors cannot be obtained exactly; however, several semi-quantitative approaches have been proposed [33]. In this paper, we shall present analytical approximations for obtaining the eigenwavevectors, using an original method. We are, actually, in a fortunate situation, when the knowledge of the eigenvalues of the wave vectors allows the knowledge of eigenfunctions. The case of very deep wells generates a well studied model, equivalent to an Ising ansamblé of spins, and will not be treated here.

The structure of this paper is the following. In Section 2 we shall shortly introduce the anharmonic solid model. In Section 3, we shall obtain a formula for the dielectric susceptibility, which shall be used for the evaluation of the critical temperature. Section 4 is devoted to a detailed study of the double symmetric rectangular well; in Section 5, we shall obtain the critical equation. Section 6 contains final comments.

2 Models of anharmonic solids

There are, of course, many models of anharmonic solids - actually, as many as interatomic potentials can be imagined. One of the most appealing is a simple one, proposed in the pioneering age of the ferroelectricity theory [34], [35], [36]. It consists of a rectangular lattice of on-site quartic quantum oscillators, interacting with their nearest neighbors by elastic forces. It is described by the Hamiltonian:

$$H = \sum_n \frac{P_n^2}{2M} - \frac{A}{2} \sum_n X_n^2 + \frac{B}{4} \sum_n X_n^4 + \frac{C}{2} \sum_{n,n'} \sigma_{n,n'} (X_n - X_{n'})^2 \quad (1)$$

where $\sigma_{n,n'} = 1$ for nearest neighbors and 0 otherwise. The model can be used both in the classical, and in the quantum case. We shall study the quantum case, and we shall obtain the classical one in the limit $\hbar \rightarrow 0$. In order to avoid physically irrelevant complications, we shall consider the isotropic case; the anisotropy can be easily introduced, if needed. The system displays a phase transition, if its dimensionality is larger than 1, $d > 1$. For $d = 4$, the model gives the exact values of critical indices.

It is convenient to define dimensionless parameters of length, temperature and mass:

$$X = \sqrt{\frac{B}{A}}x, \quad t = \frac{B}{AC}T, \quad m = \frac{CA^2}{\hbar^2 B^2}M \quad (2)$$

as well as a parameter characterizing the ratio between the on-site and inter-site potential:

$$a = \frac{A}{C} \quad (3)$$

For small values of a , the wells are shallow. This is the most interesting situation, for physical point of view, and it will be investigated in the present paper. For larger values of the parameter a , there are several excellent analytic approximations for the deep levels of the wells, including WKB.

Both for deep and shallow wells, the area of the surface delimited by wells and bump, in the $x - V(x)$ plane, are comparable, for the usual choice of coordinate system; in the case described by (1),

$$V(x) = -\frac{A}{2}x^2 + \frac{B}{4}x^4$$

Taking into consideration this fact, we shall be able to make a realistic choice of the rectangular potential (double symmetric well), as an reasonable approximant of the potential $V(x)$ of the aforementioned formula.

3 The dielectric susceptibility

In this section, we shall obtain a formula for the dielectric susceptibility of the system, which will allow us to find, in the mean field approximation, the critical temperature of the phase transition underwent by the system described by the Hamiltonian (1).

For the beginning, let us consider that the Hamiltonian describing our system may be written as the sum of an exactly soluble Hamiltonian, \mathcal{H}_0 , and of a perturbation \mathcal{V} :

$$\mathcal{H} = \mathcal{H}_0 + \mathcal{V} \quad (4)$$

The eigenvectors and the eigenvalues of \mathcal{H}_0 satisfy the equation:

$$\mathcal{H}_0 |n\rangle = E_n^{(0)} |n\rangle \quad (5)$$

In the second order of the perturbation theory, the energy of an eigenstate of the Hamiltonian \mathcal{H} is:

$$E_n = E_n^{(0)} + \langle n | \mathcal{V} | n \rangle + \sum_{m \neq n} \frac{|\langle n | \mathcal{V} | m \rangle|^2}{E_n^{(0)} - E_m^{(0)}} \quad (6)$$

If

$$\mathcal{V} = -Fx \quad (7)$$

is the potential energy of a particle situated in an external field (which can be an electric field) F , the equation (6) can be put in the form:

$$E_n = E_n^{(0)} - F \langle n | x | n \rangle + F^2 \sum_{m \neq n} \frac{|\langle n | x | m \rangle|^2}{E_n^{(0)} - E_m^{(0)}} \quad (8)$$

and the quantum average of the dipolar momentum will be given by the expression:

$$P_n = -\frac{\partial E_n}{\partial F} \quad (9)$$

The dielectric susceptibility is given by:

$$\chi_n = \frac{\partial P_n}{\partial F} = -\frac{\partial^2 E_n}{\partial F^2} = -\sum_{m \neq n} \frac{2|\langle n | x | m \rangle|^2}{E_n^{(0)} - E_m^{(0)}} \quad (10)$$

Its statistical average is:

$$\chi = \frac{1}{Z_0} \sum_{m \neq n} \exp(-\beta E_n^{(0)}) \frac{2|\langle n | x | m \rangle|^2}{E_m^{(0)} - E_n^{(0)}} \quad (11)$$

where Z_0 is the partition sum corresponding to the Hamiltonian \mathcal{H}_0 :

$$Z_0 = \sum_n \exp(-\beta E_n^{(0)}) \quad (12)$$

At $T = 0$, formula (12) takes a simple form. If $T \rightarrow 0$, the canonical distribution function $\rho(E_n)$:

$$\rho(E_n) = \frac{1}{Z} \exp(-\beta E_n) = \exp[\beta(F - E_n)] \quad (13)$$

with $F = U - TS = -T \ln Z$ is the free energy, $U = \langle \mathcal{H} \rangle$ - the internal energy and S - the entropy, can be written as:

$$\rho(E_n) = \exp \left[-S(T) + \frac{U - E_0}{T} + \frac{E_0 - E_n}{T} \right] \quad (14)$$

Taking, in this expression, the limit $T \rightarrow 0$, noticing that $\lim_{T \rightarrow 0} U(T) = E_0$ and that, according to the third principle of thermodynamics, $S(0) = 0$, we get, for the distribution function, the following expression:

$$\lim_{T \rightarrow 0} \rho(E_n) = \rho(E_0) = C \delta_{E_0 - E_n, 0} \quad (15)$$

where $\delta_{E_0 - E_n, 0}$ is the Kronecker function:

$$\delta_{E_0 - E_n, 0} = \begin{cases} 1, & E_0 = E_n \\ 0, & E_0 \neq E_n \end{cases} \quad (16)$$

and C - a constant, which can be obtained from the normalization condition, $\sum_n \rho(E_n) = 1$. This gives $C = 1/g_0$, where g_0 is the degeneration of the ground state, which has always the value $g_0 = 1$. The physical meaning of the relation (15) is the following: if $T \rightarrow 0$, the canonical distribution tends to the microcanonical one, corresponding to the ground state.

Finally, we get the following formula for the susceptibility:

$$\chi(T=0) = \sum_m \frac{2 |\langle 0 | x | m \rangle|^2}{E_m^{(0)} - E_0^{(0)}} \quad (17)$$

It is, as expected, a positive quantity, as $E_m^{(0)} - E_0^{(0)} > 0$ for any $m > 0$.

3.1 The susceptibility and the phase transition

Let us presume that the Hamiltonian has the form:

$$\mathcal{H} \rightarrow H = -\frac{1}{2m} \sum_n \nabla_n^2 + \left(2d - \frac{a}{2} \right) \sum_n x_n^2 + \frac{a}{4} \sum_n x_n^4 - \sum_n \left(\sum_m x_n \sigma_{nm} \right) x_n \quad (18)$$

In the mean field approximation, we make the replacement:

$$\left(\sum_m x_n \sigma_{nm} \right) \rightarrow 4d \langle x \rangle \equiv F \quad (19)$$

where F is the effective field, which behaves as an external electric field. So, (15) becomes a sum of non-interacting Hamiltonians:

$$H = \sum_n \left[-\frac{1}{2m} \nabla_n^2 + \left(2d - \frac{a}{2} \right) x_n^2 + \frac{a}{4} x_n^4 - F x_n \right] = H_0 + V \quad (20)$$

with

$$H_0 = \sum_n \left[-\frac{1}{2m} \nabla_n^2 + \left(2d - \frac{\alpha}{2} \right) x_n^2 + \frac{\alpha}{4} x_n^4 \right] \quad (21)$$

and the physics of the system can be obtained from the one-particle Hamiltonian:

$$H_{MF} = -\frac{\nabla^2}{2m} + \left(2d - \frac{\alpha}{2} \right) x^2 + \frac{\alpha}{4} x^4 - Fx \equiv H_{MF}^{(0)} - Fx \quad (22)$$

where we put

$$H_{MF}^{(0)} = -\frac{\nabla^2}{2m} + \left(2d - \frac{\alpha}{2} \right) x^2 + \frac{\alpha}{4} x^4 \quad (23)$$

The average of the reduced coordinate x is given by:

$$\langle x \rangle = \frac{1}{Z} \text{Tr} [-\beta (H_0 - Fx)] = \frac{1}{\beta} \frac{\partial \ln Z}{\partial F} \quad (24)$$

with

$$Z = \sum_n \exp(-\beta E_n) \quad (25)$$

The condition (24) is a self-consistent equation for $\langle x \rangle$, as this expression enters also in the expression of Z . The phase transition is given by the condition $\langle x \rangle = 0$. It will be put in a more convenient form in the next paragraph.

Taking the derivative with respect to $\langle x \rangle$ in the both sides of equation (24), we get:

$$1 = \frac{1}{\beta_c} \frac{\partial^2 \ln Z}{\partial \langle x \rangle \partial F} \Big|_{\langle x \rangle=0} = \frac{4d}{\beta_c} \frac{\partial^2 \ln Z}{\partial F^2} \Big|_{\langle x \rangle=0} \quad (26)$$

where we put, according to (19),

$$F = 4d \langle x \rangle \quad (27)$$

In the same time:

$$\begin{aligned} \frac{\partial^2 \ln Z}{\partial F^2} \Big|_{\langle x \rangle=0} &= \beta^2 \left\{ \frac{1}{Z} \frac{\partial^2 Z}{\partial F^2} - \left(\frac{1}{Z} \frac{\partial Z}{\partial F} \right)^2 \right\} \Big|_{\langle x \rangle=0} = \\ &= \beta^2 \left[\langle x^2 \rangle - \langle x \rangle^2 \right] \Big|_{\langle x \rangle=0} = \beta^2 \langle x^2 \rangle \Big|_{\langle x \rangle=0} \end{aligned} \quad (28)$$

Consequently, the critical equation (24) can be written as:

$$1 = 4d\beta_c \langle x^2 \rangle \Big|_{\langle x \rangle=0} \quad (29)$$

Coming back now to factor AC/B , previously omitted for reasons of simplicity, and replacing the reduced coordinate x with the physical one X , we get:

$$1 = \frac{4d}{T_c} C \langle X^2 \rangle \Big|_{\langle X \rangle = 0} \quad (30)$$

where T_c is the critical temperature of the phase transition.

The susceptibility of this system can be obtained as derivative of $\langle X \rangle$ with respect to the effective field F . We get from (24):

$$\chi = \frac{\partial \langle X \rangle}{\partial F} \Big|_{F=0} = \beta_c \langle X^2 \rangle \Big|_{F=0} \quad (31)$$

As the condition $F = 0$ is equivalent with $\langle X \rangle = 0$, using (28) and (29), we obtain the condition:

$$4dC\chi = 1 \quad (32)$$

This relation is remarkable, because the phase transition in the system (18) can be obtained only the simpler, "unperturbed" Hamiltonian, H_0 , defined in the equation (20).

In spite of the simplification produced by the mean field approximation, even the problem of obtaining the eigenfunctions and the eigenvalues of this "simpler" Hamiltonian, necessary for the evaluation of the matrix elements entering in (11), is not very simple. Actually, there are no exact solutions, and the approximate ones refer to the very deep wells only. For shallow wells, which are essential for the understanding of the phase transitions in ψ^4 systems, the only way of obtaining analytical results which could be used in eq. (11) is to obtain an exactly solvable, two well potential, and the most convenient one is the two well rectangular symmetric potential.

4 The two well rectangular symmetric potential

We shall define the potential of the double rectangular symmetric well considering that the origin of the energy, i.e. the level $E = 0$, corresponds to the upper level of the two symmetric wells:

$$V(x) = -V, \quad V > 0 \quad (33)$$

for $-a - \frac{b}{2} < x < -\frac{b}{2} \cup \frac{b}{2} < x < \frac{b}{2} + a$, and zero for $-\frac{b}{2} < x < \frac{b}{2}$. For $|x| > \frac{b}{2} + a$, the wall is impenetrable, in other words $V(x > \frac{b}{2} + a) = V(x < -\frac{b}{2} - a) = \infty$. The potential is symmetric, so the eigenstates have well determined parity. Also, the states with negative energy ($E < 0$), in other words, the states "inside the wells" must be described separately from the states "outside the wells", which are the states with positive energy ($E > 0$). Much effort was invested recently in obtaining analytical approximations for symmetric and asymmetric square

wells, with homogenous heterostructures or with BenDaniel - Duke boundary conditions [37], [38], [38], [39], [40], [41].

4.1 $E < 0$: even states, the eigenfunctions and eigenenergies

The wave function for even states are:

$$\psi_e(x) = A_e \sin k_e \left(a + \frac{b}{2} - x \right), \quad \frac{b}{2} < x < a + \frac{b}{2}, \quad k_e^2 = \frac{2m(-|E| + V)}{\hbar^2} \quad (34)$$

$$\psi_e(x) = B_e \cosh q_e x, \quad 0 < x < \frac{b}{2}, \quad q_e^2 = \frac{2m|E|}{\hbar^2} \quad (35)$$

$$\psi_e(x) = \psi_e(-x) \quad (36)$$

It is convenient to use, for the potential, alternatively with the quantity V , the quantity v too, defined by the relation:

$$q_e^2 + k_e^2 = v^2 = \frac{2mV}{\hbar^2}, \quad V > 0 \quad (37)$$

This quantity has the dimension of a wave vector. The continuity of the wave function and of its derivative in $x = b/2$ gives the following relations:

$$A_e \sin k_e a = B_e \cosh q_e \frac{b}{2} \quad (38)$$

$$-A_e k_e \cos k_e a = q_e B_e \sinh q_e \frac{b}{2} \quad (39)$$

and the eigenvalue equation has the form:

$$\frac{1}{k_e} \tan k_e a = -\frac{1}{q_e} \coth \frac{q_e b}{2} \quad (40)$$

The wave function is normalized if:

$$\frac{1}{B_e^2} = \frac{a}{2} + \frac{b}{4} + \left(1 + \frac{q_e^2}{k_e^2} \right) \left(\frac{1}{4q_e} \sinh b q_e + \frac{a}{2} \sinh^2 \frac{b q_e}{2} \right) \quad (41)$$

and:

$$\begin{aligned} \frac{1}{A_e^2} &= \frac{1}{B_e^2} \frac{\sin^2 k_e a}{\cosh^2 \frac{q_e b}{2}} = \\ &= \frac{1}{B_e^2} \frac{k_e^2}{q_e^2 \sinh^2 \frac{b q_e}{2} + k_e^2 \cosh^2 \frac{b q_e}{2}} \end{aligned} \quad (42)$$

4.2 $E < 0$: odd states, the eigenfunctions and eigenenergies

Similarly to (34), we have, in the odd case:

$$\psi_o(x) = A_o \sin k_o \left(a + \frac{b}{2} - x \right), \quad \frac{b}{2} < x < a + \frac{b}{2} \quad (43)$$

$$\psi_o(x) = B_o \sinh q_o x, \quad 0 < x < \frac{b}{2} \quad (44)$$

$$\psi_o(-x) = -\psi_o(x) \quad (45)$$

The continuity conditions give:

$$A_o \sin k_o a = B_o \sinh \frac{q_o b}{2} \quad (46)$$

$$-k_o A_o \cos k_o a = q_o B_o \cosh \frac{q_o b}{2} \quad (47)$$

Consequently, the eigenvalue equation is:

$$\frac{1}{k_o} \tan k_o a = -\frac{1}{q_o} \tanh \frac{q_o b}{2} \quad (48)$$

The wave function is normalized if:

$$\frac{1}{B_o^2} = -\frac{a}{2} - \frac{b}{4} + \left(1 + \frac{q_o^2}{k_o^2} \right) \left(\frac{1}{4q_o} \sinh bq_o + \frac{a}{2} \cosh^2 \frac{bq_o}{2} \right) \quad (49)$$

$$\frac{1}{A_o^2} = \frac{k_o^2}{q_o^2 \cosh^2 \frac{q_o b}{2} + k_o^2 \sinh^2 \frac{bq_o}{2}} \frac{1}{B_o^2} \quad (50)$$

4.3 $E > 0$: even states, the eigenfunctions and the energies

In this case, instead of the relations (34) - (36) we shall have:

$$\psi_e(x) = A_e \sin k_e \left(a + \frac{b}{2} - x \right), \quad \frac{b}{2} < x < a + \frac{b}{2}, \quad (51)$$

$$k_e^2 = \frac{2m(E+V)}{\hbar^2}, \quad E > 0, \quad V > 0$$

$$\psi_e(x) = B_e \cos q_e x, \quad 0 < x < \frac{b}{2}, \quad q_e^2 = \frac{2mE}{\hbar^2} \quad (52)$$

$$\psi_e(-x) = \psi_e(x) \quad (53)$$

$$k_e^2 = \frac{2m(E+V)}{\hbar^2} = q_e^2 + v^2, \quad v^2 = \frac{2mV}{\hbar^2}$$

The continuity conditions give:

$$A_e \sin k_e a = B_e \cos \frac{q_e b}{2} \quad (54)$$

$$-k_e A_e \cos k_e a = -q_e B_e \sin \frac{q_e b}{2} \quad (55)$$

and the eigenvalue equation is:

$$\tan k_e a = \frac{k_e}{q_e} \cot \frac{q_e b}{2} \quad (56)$$

The wave function is normalized if:

$$\frac{1}{B_e^2} = \frac{b}{4} + \frac{a}{2} + \left[\frac{1}{4q_e} \sin q_e b - \frac{a}{2} \sin^2 \frac{q_e b}{2} \right] \left(1 - \frac{q_e^2}{k_e^2} \right) \quad (57)$$

$$\frac{1}{A_e^2} = \frac{1}{B_e^2 \cos^2 \frac{q_e b}{2}} \frac{1}{1 + \frac{q_e^2}{k_e^2} \tan^2 \frac{q_e b}{2}} = \frac{1}{B_e^2 \cos^2 \frac{q_e b}{2} + \frac{q_e^2}{k_e^2} \sin^2 \frac{q_e b}{2}} \quad (58)$$

4.4 $E > 0$: odd states, the wave functions and energies

We have, similarly to the previous formulas:

$$\psi_o(x) = A_o \sin k_o \left(a + \frac{b}{2} - x \right), \quad \frac{b}{2} < x < a + \frac{b}{2} \quad (59)$$

$$\psi_o(x) = B_o \sin q_o x, \quad 0 < x < \frac{b}{2} \quad (60)$$

$$\psi_o(-x) = -\psi_o(x) \quad (61)$$

The continuity conditions give:

$$A_o \sin k_o a = B_o \sin \frac{q_o b}{2} \quad (62)$$

$$-k_o A_o \cos k_o a = q_o B_o \cos \frac{q_o b}{2} \quad (63)$$

and the eigenvalue equation has the form:

$$\tan k_o a = -\frac{k_o}{q_o} \tan \frac{q_o b}{2} \quad (64)$$

The wave function is normalized if:

$$\frac{1}{B_o^2} = \frac{b}{4} + \frac{a}{2} + \left(-1 + \frac{q_o^2}{k_o^2} \right) \left(\frac{1}{4q_o} \sin q_o b + \frac{a}{2} \cos^2 \frac{q_o b}{2} \right) \quad (65)$$

$$A_o = B_o \frac{\sin \frac{q_o b}{2}}{\sin k_o a} \quad (66)$$

4.5 Approximate solutions for a shallow well

From the perspective of the applications into statistical mechanics, it is important to have a precise description of about the first bound state - i.e. how the first level of negative energy - shows up. We shall find, for this fact, analytical approximations for the energy eigenvalues. We shall investigate firstly the negative, and afterwards, the positive energy states.

4.5.1 Negative energy states

It is easy to check that the eigenvalue equation for negative energies have solutions only if:

$$v > v_{\min} = \frac{\pi}{2a} \quad (67)$$

With

$$z = \frac{q_e}{v} \quad (68)$$

and

$$v = \frac{\pi}{2a} + \varepsilon \quad (69)$$

the eigenvalue equation for negative energy is:

$$\tan a \left(\frac{\pi}{2a} + \varepsilon \right) \sqrt{1 - z^2} = -\frac{\sqrt{1 - z^2}}{z} \coth \frac{zb}{2} \left(\frac{\pi}{2a} + \varepsilon \right) \quad (70)$$

because the root of the equation corresponds to a very small value of z , and the value of the function \coth is quite insensitive in the vicinity of the value of $\frac{\pi}{2a}$:

$$\tan a \left(\frac{\pi}{2a} + \varepsilon \right) = -\cot a\varepsilon = -\frac{1}{z} \coth \frac{zb}{2} \frac{\pi}{2a} = -\frac{1}{z} \coth \frac{\pi b z}{4a}$$

Keeping only the first term of the series expansion, we get:

$$z^2 = \frac{4a^2}{\pi b} \varepsilon = \frac{q_e^2}{v^2}, \quad q_e^2 \simeq \frac{\pi}{b} \varepsilon$$

Consequently:

$$q_e^2 = \frac{\pi}{b} \varepsilon = \frac{\pi}{b} \left(v - \frac{\pi}{2a} \right), \quad v \gtrsim \frac{\pi}{2a}, \quad v = \frac{\pi}{2a} + \varepsilon \quad (71)$$

and:

$$q_e^2 = \frac{2m|E|}{\hbar^2}, \quad E = -\frac{\hbar^2}{2m} \frac{\pi}{b} \varepsilon = \frac{\pi^2 \hbar^2}{4abm} - \frac{\pi \hbar}{b\sqrt{2m}} \sqrt{V} < 0 \quad (72)$$

The minimum value of the potential V , beyond which the first state of negative energy shows up, is:

$$v_{\min} = \frac{\pi}{2a}, \quad V_{\min} = \frac{\hbar^2 v_{\min}^2}{2m} = \frac{\hbar^2 \pi^2}{8ma^2} \quad (73)$$

It is interesting to compare this minimal value with the energy of the first level of an infinite rectangular well of width $L = 2a + b$:

$$E_1^{(\infty)} = \frac{\hbar^2 \pi^2}{2m (2a + b)^2}$$

Consequently:

$$\frac{V_{\min}}{E_1^{(\infty)}} = \frac{\hbar^2 \pi^2}{2m 4a^2} \frac{2m (2a + b)^2}{\hbar^2 \pi^2} = \left(\frac{2a + b}{2a} \right)^2 = \left(1 + \frac{b}{2a} \right)^2 \quad (74)$$

So, the potential which produces the first state of negative energy is comparable with (actually, slightly larger than) the energy of the first level of the infinite rectangular well of identical width.

4.5.2 Positive energy states

Even states In the new variable z , the eigenvalue equation (56) is:

$$\tan av \sqrt{1 + z^2} = \frac{\sqrt{1 + z^2}}{z} \cot \frac{vzb}{2} \quad (75)$$

Numerical considerations concerning this equation show that it can be replaced, with minor consequences on the accuracy of the solutions, by its "asymptotic" form, i.e. the form reached by the approximation:

$$\frac{\sqrt{1 + z^2}}{z} \simeq 1 \quad (76)$$

so, the eq. (75) can be replaced by:

$$\tan av \sqrt{1 + z^2} = \cot \frac{vzb}{2} \quad (77)$$

Looking for solution in the neighborhood of $v_{\min} = \frac{\pi}{2a}$, we have:

$$\tan \frac{\pi}{2} \sqrt{1 + z^2} = \cot \frac{\pi zb}{2a} = \tan \frac{\pi}{2} \left(1 - \frac{zb}{2a} \right) \quad (78)$$

Consequently, we obtain the following quantization condition:

$$\frac{\pi}{2} \sqrt{1 + z^2} - \frac{\pi}{2} \left(1 - \frac{zb}{2a} \right) = \frac{\pi}{2} \sqrt{1 + z^2} - \frac{\pi}{2} + \frac{\pi zb}{2a} = n\pi \quad (79)$$

or:

$$\sqrt{1 + z^2} = (2n + 1) - \frac{zb}{2a} \quad (80)$$

The equation can be also written as:

$$\left(1 - \frac{b^2}{4a^2}\right) z^2 + 2z(2n+1) \frac{b}{2a} - 4n^2 - 4n = 0 \quad (81)$$

The root relevant for our problem is:

$$z_n = (2n+1) \frac{b}{2a} \frac{\sqrt{1 + \frac{4n(n+1)}{(2n+1)^2} \frac{4a^2 - b^2}{b^2}} - 1}{\left(1 - \frac{b^2}{4a^2}\right)} \quad (82)$$

The factor

$$f(n) = \frac{4n(n+1)}{(2n+1)^2} \quad (83)$$

is very closed to 1, even for small values of n :

$$f(1) = \frac{8}{9}; \quad f(2) = \frac{24}{25}; \quad f(3) = \frac{48}{49}$$

and the expression (82) for z_n can be put in a simpler form:

$$z_n = (2n+1) \frac{2a}{(2a+b)}, \quad q_n = vz; \quad E_n = z_n^2 V = (2n+1)^2 \frac{4a^2}{(2a+b)^2} V \quad (84)$$

$$E_n = (2n+1)^2 \frac{4a^2}{(2a+b)^2} V$$

$$k_e^2 = \frac{2m(E+V)}{\hbar^2} = q_e^2 + v^2, \quad v^2 = \frac{\pi^2}{4a^2} + \varepsilon \frac{\pi}{a}; \quad V = \frac{\pi^2 \hbar^2}{8ma^2} + \varepsilon \frac{\pi \hbar^2}{a 2m}$$

Odd states Following the same steps as for the even states, we get, instead of (84), the following result:

$$z_n = \frac{2n}{1 + \frac{b}{2a}} - \frac{1}{4n} = 2n \frac{2a}{2a+b} - \frac{1}{4n} \quad (85)$$

4.6 The symmetric rectangular well and the physics of quantum wells and quantum dots

We shall discuss now another application of the symmetric rectangular well, which can be developed using the method outlined in the previous subsections. Actually, we shall describe some applications in nanophysics of the simple quantum mechanical problems, where various types of rectangular potentials are involved. The simplest example is provided by the finite rectangular well, which is a useful starting point for understanding the physics of quantum wells and quantum dots.

A quantum dot can be sometimes described as an atomic cluster, of quasi-spherical shape. Such clusters are stable for some "Magical numbers", taking the values 55, 147, 309, 567 etc. Elementary considerations - similar to those used in nuclear models - shows that the radius of a cluster is proportional to the cubic root of the number of atoms:

$$R = aN^{1/3}$$

where a is close to the atomic radius, of order $\sim 0.1nm$. So, a cluster of about 10^3 atoms has a radius of about $1nm$.

From these dimensions we can speak, at least in the central part of the cluster, about a regular pattern of atoms, which becomes, if the number of constituents increases, a lattice with a certain symmetry. Of course, for a cluster the quantum size effects are very important, and strongly influence the band structure of the nano-object. These effects are important when the cluster dimension is comparable with λ the electron wave length, or smaller. For electrons in metals, $\lambda \sim 0.5nm$, but in semiconductors, where the effective mass can be much smaller, l can be much larger, $\lambda \sim 1\mu m$. The semiconductor clusters are particular cases of quantum dots. As the electrons are confined in a small space, their energy is affected by quantum size effects.

Other examples of quantum dots are cubic - or rectangular - cavities. In spite of the differences between spherical or rectangular cavities, the mathematical methods for obtaining the wave functions and wave vectors are quite similar. The similarity between the 1D cartesian wave equation in a rectangular geometry, and the radial equation in a spherical geometry, are more pronounced for low values of quantum radial number l , and almost identical for $l = 0$. So, the results obtained for rectangular wells can be easily transferred to spherical cavities of zero angular momentum.

The double quantum dots are aggregates composed by two quantum dots, used as constitutive components of a large number of electronic or opto-electronic devices. If the shape of each quantum dot can be approximated with a parallelepiped, the "artificial molecule" formed in this way can be studied using the model of the rectangular symmetric two well potential. So, the methods used to get analytical approximations for the particle energy in such potentials have interesting applications in the physics of quantum dots.

5 The critical equation

5.1 Dipolar matrix elements

For symmetry (or, better saying, parity) reasons, only the matrix elements of the coordinate x between the ground state (which is an even state) and odd states of positive energy are non-zero, so we have to evaluate integrals having the form:

$$\langle x \rangle_{e,n} = 2 \int_0^{a+b/2} x \psi^{(e)}(x) \psi_n^{(o)}(x) dx \quad (86)$$

where n refers to odd states. The previous notation (57) is slightly modified, being replaced with:

$$\psi_n^{(o)}(x) = A_n \sin k_n \left(a + \frac{b}{2} - x \right), \quad \frac{b}{2} < x < a + \frac{b}{2} \quad (87)$$

$$\psi_n^{(o)}(x) = B_n \sin q_n x, \quad 0 < x < \frac{b}{2} \quad (88)$$

Also, for even states:

$$\psi^{(e)}(x) = A \sin k \left(a + \frac{b}{2} - x \right), \quad \frac{b}{2} < x < a + \frac{b}{2} \quad (89)$$

$$\psi^{(e)}(x) = B \cosh qx, \quad 0 < x < \frac{b}{2} \quad (90)$$

In the lowest order in ε ,

$$q^2 = \frac{\pi}{b} \varepsilon; \quad k^2 = v^2 - q^2 = v^2 - \frac{\pi}{b} \varepsilon = \left(\frac{\pi}{2a} \right)^2 + \varepsilon \pi \left(\frac{1}{a} - \frac{1}{b} \right) \quad (91)$$

$$k = \sqrt{\left(\frac{\pi}{2a} \right)^2 + \varepsilon \pi \left(\frac{1}{a} - \frac{1}{b} \right)} = \quad (92)$$

$$= \frac{\pi}{2a} \left[1 + 2a\varepsilon \left(\frac{1}{a} - \frac{1}{b} \right) \right] = \frac{\pi}{2a} + \varepsilon \pi \left(\frac{1}{a} - \frac{1}{b} \right) \quad (93)$$

Also, in the lowest order in ε , we can use the following approximations:

$$\cosh qx = 1 + \frac{1}{2} \frac{\pi}{b} \varepsilon x^2 \quad (94)$$

$$\sin k \left(a + \frac{b}{2} - x \right) = \quad (95)$$

$$= \cos \left(\frac{\pi}{2a} \frac{b}{2} - \frac{\pi}{2a} x \right) + \varepsilon \pi \left(\frac{1}{a} - \frac{1}{b} \right) \left(a + \frac{b}{2} - x \right) \sin \left(\frac{\pi}{2a} x - \frac{\pi}{2a} \frac{b}{2} \right)$$

However, the ε -dependence of the matrix elements is irrelevant, compared to the exponential factors, so the matrix element can be written as:

$$\frac{1}{2} \langle x \rangle_{e,n} = BB_n I_b + \check{\alpha}_n I_a \quad (96)$$

with:

$$I_b = \int_0^{b/2} x \sin q_n^0 x \, dx \quad (97)$$

and:

$$I_a = \int_{b/2}^{a+b/2} x \cos \left(\frac{\pi b}{2a} - \frac{\pi}{2a} x \right) \sin k_n^0 \left(a + \frac{b}{2} - x \right) dx \quad (98)$$

As the quantities $q_n^0 = q_n(\varepsilon = 0)$ and $k_n^0 = k_n(\varepsilon = 0)$ depend only on well geometry, more exactly on a and b , not on the mass m , they are just numbers, playing a peripheric role in the expression of the susceptibility. However, these formulas are not taken into consideration in the present paper, where only the dominant term in the susceptibility formula will be considered.

5.1.1 The critical temperature

The susceptibility is given by the formula:

$$\chi = \frac{1}{Z} \left\{ \sum_{n=1}^{\infty} \frac{2d_{no,\varepsilon}^2}{E_n^{(o)} - E_\varepsilon} \exp(-\beta E_n^{(o)}) + \sum_{n=2}^{\infty} \frac{2d_{no,1\varepsilon}^2}{E_{no} - E_{1\varepsilon}} \exp(-\beta E_n^{(o)}) + \dots \right\} \quad (99)$$

where the upper index (o) refers to odd levels. The first term:

$$\frac{2d_{no,\varepsilon}^2}{E_n^{(o)} - E_\varepsilon} \exp(-\beta E_1^{(o)}) \quad (100)$$

is always the dominant one.

The statistical sum can be approximated by the expression:

$$Z = \frac{1}{2} \left[\vartheta_3 \left(0, \frac{4a^2}{(2a+b)^2} \beta V \right) - 1 \right] \quad (101)$$

where ϑ_3 is the Jacobi elliptic function. In the lowest approximation:

$$\frac{1}{Z} \simeq \exp \frac{4a^2}{(2a+b)^2} \beta V \quad (102)$$

Concerning the critical equation, we are specially interested in the connection between temperature, mass and potential - in our case, V . It is close to the value $\pi/2a$, so it can be written as: $v = \pi/2a + \varepsilon$. The elements of the dipolar matrix depend on the well geometry, more exactly on the parameters a and b , but not on mass or temperature; these quantities enter in the expressions of the energy eigenvalues. Finally, we get the following expression for the critical equation:

$$dC \frac{\exp \left(-\frac{32a^2}{L^2} \beta V \right)}{\frac{36a^2}{L^2} V + \frac{\pi \hbar}{b\sqrt{2m}} \sqrt{V} - \frac{\pi^2 \hbar^2}{4abm}} = \text{const.} \quad (103)$$

It gives the connection between temperature, through β , mass m and potential V . The result is correct for $d = 2$ and $d = 3$, but cannot be taken into consideration for $d = 1$, because, as is well known, the mean field approximation gives incorrect predictions for 1D systems.

In the classical limit, $\hbar \rightarrow 0$ and $m \rightarrow \infty$, so eq. (103) becomes:

$$\frac{1}{T} \sim \left| \frac{\ln V}{V} \right| \quad (104)$$

It is quite similar to another result, also obtained in the mean field approximation, for a planar aggregate of coupled Ginzburg - Landau chains ([27], eq. (43)). A formula similar to (104) was firstly obtained by Scalapino, Imry and Pincus [42], using another approach. Numerically, the result was been previously reported by Bishop and Krumhansl [43]: the dependence between T and V obtained numerically by these authors, is fitted by a law similar to (104). The result is also in qualitative agreement with Monte Carlo simulation, worked out with a polynomial potential [16], [17], [18].

6 Conclusions

The critical equation of the structural phase transition, taking place in a rectangular lattice of quartic quantum oscillators, interacting by elastic forces with their nearest neighbors, is obtained in a mean field approximation. In order to get analytical results, the quartic, on-site potential must be replaced with a similar, but simpler one - the symmetric rectangular double well. We propose original methods for obtaining the energy eigenvalues, using an approach described in [44], [45]. A convenient property of the aforementioned potential is that, if the energy eigenvalues are known, the eigenfunctions are also known. In this way, it was possible to evaluate the electrical susceptibility of the model, and to obtain the critical equation. A similar exercise could be repeated with another simple model of two minima potential - the so-called two center harmonic oscillator.

The similarity between the result obtained in this paper and other results, obtained using mean field theory or numerical approaches [46], suggests that the approach developed here is useful and efficient. It provides, at the best of author's knowledge, the first analytical approximation of the bound states energy in a shallow double well, which also allows to obtain the analytic form of the wave functions. In this way, this approach can be immediately transferred in nanophysics [47]. Our results are in accordance with Monte Carlo simulations.

References

- [1] L.D. Landau, E.M. Lifshitz: Physique statistique, Ed. Mir, Moscou, 1972
- [2] R.A. Cowley, Adv.Phys. **29**, 1 (1980)
- [3] A.D. Bruce, Adv.Phys. **29**, 111 (1980)
- [4] D.J. Scalapino, M. Sears, R.A. Ferrell, Phys.Rev. **B6**, 3409 (1972)
- [5] B. Stoeckly, D.J. Scalapino, Phys.Rev. **B11** 205 (1975)
- [6] B. Stoeckly, Phys.Rev. **B14**, 1271 (1976)
- [7] T.D. Schultz, D.C. Mattis, E.H. Lieb, Rev.Mod.Phys. **36**, 856 (1964)
- [8] G.D. Mahan: Many-particle physics, Plenum Press (1990)
- [9] V.Barsan, Rev.Roum.Phys. **30**, 775 (1985); J.Phys.:Cond.Matter **1**, 7961 (1989); **2**, 4815 (1990)
- [10] V. Barsan, J.Phys.:Cond.Matter **1**, 7961 (1989)
- [11] V. Barsan, J.Phys.:Cond.Matter **2**, 4815 (1990)
- [12] V.Barsan, S.Cojocaru, Rom.Rep.Phys. **58**, 123 (2006)
- [13] S.Cojocaru, V. Barsan, A.Ceulemans, physica status solidi **B 243** 1963 (2006)
- [14] S.Cojocaru, V. Barsan, A.Ceulemans, J.Mag.Magn.Mat. **307**, 62 (2006)
- [15] S.Cojocaru, V. Barsan, A.Ceulemans, Philos.Mag. **86**, 4983 (2006)
- [16] R. Toral, A. Chakrabarti, Phys.Rev. **B42**, 2445 (1990)
- [17] W. Janke, T. Sauer, J.Stat.Phys. **78**, 759 (1995)
- [18] W. Loinaz, R.S. Willey, Phys.Rev. **D58** 076003 (1998)
- [19] V.V. Savkin, A.N. Rubtsov, T. Jasen, Phys.Rev. **B65**, 214103 (2002)
- [20] V.V. Savkin, A.N. Rubtsov, J.Exp.Theor.Phys. **91**, 1204 (2000); arXiv:cond-mat/0112429v2 (2002)
- [21] V.Barsan, J.Phys.:Condensed Matter **18**, 9275 (2006)
- [22] V. Barsan, J.Phys.:Condensed Matter **20**, 019701 (2008)
- [23] V. Barsan, The Ramanujan Journal, **20**, 153 (2009)
- [24] V.Barsan, Philos. Mag. **87**, 1043 (2007)
- [25] V.Barsan, Philos. Mag. **88**, 121 (2008)

- [26] V. Barsan, *Philos. Mag.* **91**, 477 (2011)
- [27] V. Barsan, *Rom.Rep.Phys.* **60**, 205 (2008)
- [28] V. Barsan, *Rom.Rep.Phys.* **62**, 219 (2010)
- [29] R. Lungu, *Optoel.Adv.Mat.-Rapid Comm.* **5**, 1223 (2011)
- [30] Yu. Ilinskii, L. V. Keldysh, *Electromagnetic response of material media*, Plenum Press (1994)
- [31] C.M. Bender, T.T. Wu, *Phys.Rev.* **184**, 1231 (1969); *Phys.Rev.* **D7**, 1620 (1973)
- [32] G. Ciobanu, V. Barsan, A. T. Mincu, *Rom.J.Phys.* **55**, 539 (2010)
- [33] E. A. Johnson, H. T. Williams, *Amer.J.Phys.* **50**, 239 (1982)
- [34] R. Blinc, B. Zeks: *Soft modes in ferroelectrics and antiferroelectrics*, North Holland Publishing Company (1974)
- [35] A. Strukov, A.P. Levanyuk: *Ferroelectric phenomena in crystals*, Springer (1998)
- [36] K. Rabe, C. H. Ahn, J.-M. Triscone (Eds.): *Physics of ferroelectrics*, Springer (2007)
- [37] V. Barsan: Square wells, quantum wells and ultra-thin metallic films, *Philos. Mag.* **94** (2014) 190-207
- [38] V. Barsan, M.-C. Ciornei: Semiconductor quantum wells with BenDaniel-Duke boundary conditions, *Eur.J.Phys.* **38** (2017) 015407
- [39] V. Barsan: Garrett approximation for asymmetric rectangular potentials and its applications to quantum well infrared photodetectors arXiv:1805.05804v1 (2018) [physics.gen-physics]; DOI: 10.13140/RG.2.2.18395.87843
- [40] V. Barsan: Quantum Wells and Ultrathin Metallic Films, in *Heterojunctions and Nanostructures*, Ed.: V. Stavrou, InTech, (2018)
- [41] V. Barsan: Semiconductor QWs with BenDaniel-Duke boundary conditions, in: R. Inguanta (Ed.): *Semiconductors*, InTech, (2018)
- [42] D.J. Scalapino, Y. Imry, P. Pincus, *Phys.Rev.* **B11**, 2042 (1975)
- [43] A.R. Bishop, J.A. Krumhansl, *Phys.Rev.* **B12**, 2824 (1975)
- [44] V. Barsan, *Rom.Rep.Phys.* **64**, 685 (2012)
- [45] V. Barsan, R. Dragomir, *Optoel.Adv.Mat. - Rapid Comm.*, **6**, 917 (2012)
- [46] E. Van der Straeten, J. Naudts, *J.Phys.* **A39**, 933 (2006)
- [47] V. V. Mitin, D. I. Sementsov, N. Z. Vagidov, *Quantum mechanics for nanostructures*, Cambridge University Press (2012)

Exact and approximate analytical solutions of Weiss equation of ferromagnetism. Theoretical aspects (I)

Victor Barsan

IFIN-HH, Str. Reactorului 30 and CIFRA, Str. Atomostilor 105bis
Magurele 077125, Romania

Abstract

The recent progress in the theory of generalized Lambert functions makes possible to solve exactly the Weiss equation of ferromagnetism. However, this solution is quite inconvenient for practical purposes. Precise approximations are obtained, giving the temperature dependence of the spontaneous magnetization, and also the dependence of the magnetization on both temperature and external magnetic field. Exact results and approximants for the inverse Brillouin functions are obtained.

1 Introduction

The Weiss theory of ferromagnetism - sometimes called mean-field theory of ferromagnetism - is an exactly solvable model "that allows one to study thermodynamic functions in detail, in particular their properties near the critical temperature"[1]. The only element which hampers the possibility of calculating analytically any thermodynamic quantity is the fact that the equation of state, which is a transcendental equation involving the magnetization, the temperature and the external magnetic field, cannot be solved analytically. Recently, this obstacle has been formally removed, as, due to work of Mezö, Baricz [2] and Mugnaini [3], the equation of state was in principle solved, using generalized Lambert functions.

However, these solutions are quite cumbersome and difficult to handle, at least in the context of experimental magnetism. This is why it is also important to have, besides the exact solutions, some simpler analytical approximations, more convenient in practical situations. In the last decades, several analytical approximations have been obtained for the Brillouin and Langevin functions or their inverses, with applications in the mean field theory of ferromagnetism [4], hysteresis [5], [6], polymers (strong polymer deformation and flow), see [7], [8], [9], [10], [11], [12], [13] or solar energy conversion (daily clearness index), see [14], [15], [16].

A precise description of the Weiss theory is important not only for theoretical, but also for experimental physics. Even if Weiss theory is a very simple one, it is still largely used in order to obtain important material parameters of ferromagnets, like the critical temperature and the Curie constant. The present paper (I) is devoted to the theoretical aspects of the Weiss model, developed from the perspective of new results obtained in the theory of generalized Lambert functions and of their approximants. The next one (II), in these Proceedings, is devoted to the application in the experimental physics of ferromagnetism of the results exposed in (I).

The structure of the present paper is as follows. In Section 2, we shall expose the main elements of the Weiss theory and the attempts of solving - exactly or approximately - the equation of state. The exact solutions, in terms of generalized Lambert functions, are presented. In Section 3, we obtain an approximate but very precise expression of the magnetization as a function of temperature, in zero magnetic field, involving elementary functions only. In Section 4, a similar result is produced, for the case of a non-zero external magnetic field. The next section is devoted to the inverse Brillouin functions of arbitrary spin index. Besides exact results, a simple expression for an approximant, more accurate than the approximant used in literature, is obtained. A numerical result is discussed in Section 6. The last section is devoted to conclusions.

2 An outline of Weiss theory of ferromagnetism

The main equation of this theory is the equation of state, see, for example, [17], [18], [19], [20]:

$$M(T, H) = M_0 B_S \left(\frac{\bar{\mu} S}{kT} (H + \lambda M) \right), \quad \bar{\mu} = g \mu_B \quad (1)$$

describing the dependence of magnetization M on temperature T and on external magnetic field H . Also,

$$M_0 = N \bar{\mu} S = N S g \mu_B. \quad (2)$$

So, M_0 is the maximum value of the spontaneous magnetization.

The parameter λ is the molecular field parameter, introduced by Pierre Weiss in 1907, and B_S is the Brillouin function:

$$B_S(x) = \frac{2S+1}{2S} \coth \left(\frac{2S+1}{2S} x \right) - \frac{1}{2S} \coth \left(\frac{1}{2S} x \right) \quad (3)$$

If $S = 1/2$:

$$B_{1/2}(x) = \tanh x \quad (4)$$

So, if $S = 1/2$ and the external field is zero, $H = 0$, eq. (1) becomes:

$$M = M_0 \tanh \left(\frac{\bar{\mu}}{2kT} \lambda M \right) \quad (5)$$

This equation has a non-zero solution, and, equivalently, the system has a spontaneous magnetization $M \neq 0$, if the temperature T is under a critical value, namely under the critical temperature T_c , given by the following relation (see [17], eqs. (6.18), (6.19)):

$$T_c = \lambda \frac{N\bar{\mu}^2}{4k} \quad (6)$$

It is convenient to introduce the reduced parameters:

$$t = \frac{T}{T_c}, \quad h = \frac{\bar{\mu}H}{2kT_c}, \quad m = \frac{M}{M_0} \quad (7)$$

as the equation of state (1) can be put now in a simpler form:

$$m(t, h) = \tanh \frac{m(t, h) + h}{t} \quad (8)$$

If we write the reduced magnetization in zero magnetic field as

$$m(t, 0) = m(t) \quad (9)$$

the equation (1) becomes:

$$m(t) = \tanh \frac{m(t)}{t} \quad (10)$$

Because eq. (10) is sometimes called Weiss equation, we shall also adopt this terminology in the present paper. It is a transcendental equation, as its solution cannot be written as a finite combination of elementary functions.

The "Weiss equation" is present in many other domains of physics, not only in ferromagnetism. In hydrodynamics, it describes the phase velocity of water waves [21]. In quantum mechanics, it gives the eigenvalue of the wavevector of a bound state, in several potentials: a δ -function in the middle of an infinite rectangular square well ([22], problem 3.11) or an attractive δ -potential with Dirichlet boundary conditions [23]. In quantum statistical mechanics, it gives the similar eigenvector, for a Weyl semimetal ([24], eq. (8)), and the gap in the Meissner effect in gauge-invariant, self-consistent pairing theories ([25], eq. (5.5)), included also in an open access volume [26]). In heat transfer, it describes the conductivity of a cooled thin fin [27].

There are several attempts of solving, exactly or approximately, this equation. An interesting approach is due to Siewert and Essing [28]; it is based on the theory of complex functions, mainly on the theory of singular integral equations [29]. It has been systematically applied by Siewert and his co-workers in order to solve a large number of transcendental equations, involving hyperbolic (or trigonometric) and algebraic functions. However, the results obtained

in this way are not explicit and can be hardly used in practical calculations. An inventory of problems solved by Siewert and his co-workers, together with several approximants of their exact solutions, was given recently in [30].

Another approach, invented and re-invented by several authors [31], [32], puts the transcendental equation in a differential form and writes its solution as a series expansion. If we define the function $\zeta(t)$ by

$$m(t) = t\zeta(t) \tag{11}$$

the Weiss equation (10) takes the form:

$$\tanh \zeta(t) = t\zeta(t) \tag{12}$$

We easily find that $\zeta'(t)$ can be expressed in terms of the function $\zeta(t)$ and of t :

$$\zeta'(t) = \frac{\zeta(t)}{1 - t - t^2\zeta^2(t)} \tag{13}$$

As any higher order derivative of $\zeta(t)$ has the same property, we can write down the series expansion of $\zeta(t)$ near an arbitrary point t_0 as:

$$\zeta(t) = \zeta(t_0) + \zeta'(t_0)(t - t_0) + \frac{1}{2}\zeta''(t_0)(t - t_0)^2 + \dots \tag{14}$$

This approach has two inconveniences: (1) we have to check that the series exists in the neighborhood of t_0 (this is not the case, for instance, if t_0 is an essential singularity of $\zeta(t)$); (2) the radius of convergence of the series (14) is quite small, and the expansion must be repeated in the neighborhood of several points t_0 , in order to maintain a reasonable accuracy.

Recently, a crucial progress was achieved in solving a large class of transcendental equations, namely using generalized Lambert functions [2], [3], with applications to magnetism and other branches of physics [21], [33]. Let us mention that the Lambert function $W(a)$ is the solution in x of the transcendental equation:

$$xe^x = a. \tag{15}$$

In other words, the Lambert function is the inverse of the function appearing in the left hand side of (15). Similarly, the solution in x of the transcendental equation:

$$e^x \frac{(x - t_1)(x - t_2) \dots (x - t_n)}{(x - s_1)(x - s_2) \dots (x - s_m)} = a \tag{16}$$

is the generalized Lambert function

$$W(t_1, \dots, t_n; s_1, \dots, s_m; a) \tag{17}$$

One of the beneficiaries of the progress made in the study of generalized Lambert functions is the Weiss equation. Actually, eq. (12) takes the form:

$$e^{2\zeta(t)} \frac{\zeta(t) - \frac{1}{t}}{\zeta(t) + \frac{1}{t}} = 1 \quad (18)$$

whose solution can be written as [33]:

$$m(t) = t\zeta(t) = \frac{t}{2} W\left(\frac{2}{t}; -\frac{2}{t}; -1\right) \quad (19)$$

where $W\left(\frac{2}{t}; -\frac{2}{t}; -1\right)$ is a particular case of (17), namely of $W(t; s; a)$. Clearly, the parameters t, s in $W(t; s; a)$ are particular cases of the parameters $t_1, \dots, t_n, s_1, \dots, s_m$ from (16), (17) and have nothing to do with any physical quantity, like temperature or spin. At its turn, $W(t; s; a)$ can be expressed in terms of a simpler, but similar function, the r -Lambert function, W_r . $W_r(a)$ is defined as the solution of the equation:

$$xe^x + rx = a \quad (20)$$

and can be expressed as a series expansion in terms of Mezö - Baricz polynomials, $M_k^{(n)}(1/(r+1))$ [2]. Also,

$$W(t; s; a) = t + W_{-a \exp(-t)}(a(t-s)e^{-t}) \quad (21)$$

So, even if eq. (19) provides a direct and exact solution of the Weiss equation for $h = 0$ and $S = 1/2$ (e.g. the dependence of the spontaneous magnetization of a magnetic monodomain system with $S = 1/2$ versus temperature), it is quite inconvenient for practical applications. This is why a simpler analytical approximation of (19) might still be useful.

An interesting approach in finding approximate analytical solutions of transcendental equations is to approximate the non-algebraic functions involved in such equations with algebraic ones. In this way, the equation becomes algebraic, see [34], [35]. For instance, eq. (45) of [34] suggests the following approximation for the exponential function:

$$\frac{1}{2}(1 - e^{-2z}) \simeq z \frac{1 + az}{1 + cz}, \quad a = -0.0572, \quad c = 1.286, \quad 0 < z < 5 \quad (22)$$

Even if such an approximation might give useful results when applied to certain quantum mechanical problems, it is inappropriate for the Weiss equation, as it cannot reproduce the critical behavior of the magnetization on a large enough interval.

In the following section, we shall propose a precise approximate analytical solution of the Weiss equation, inspired from the standard ways of obtaining physically convenient solutions of the Schroedinger equation.

3 A precise approximate analytical solution of Weiss equation

In order to find a convenient solution of the Weiss equation (10) on the interval $(0, 1)$, we shall find out firstly the behavior of $m(t)$ for $m(t) \gtrsim 0$ and $m(t) \lesssim 1$.

So, for $t \gtrsim 0$:

$$m(t) = \tanh \frac{m(t)}{t} \simeq 1 - 2 \exp \left(-\frac{2m(t)}{t} \right) \quad (23)$$

which can be written as:

$$2 \exp \left(-\frac{2m(t)}{t} \right) = 1 - m(t) \quad (24)$$

If we put:

$$\frac{m}{t} = u, \quad m = ut \quad (25)$$

eq. (24) can be written as:

$$\exp(-2u) = -\frac{t}{2} \left(u - \frac{1}{t} \right) \quad (26)$$

The most general form of an equation which can be solved using the Lambert W function is similar to (26):

$$\exp(-cx) = a(x - r) \quad (27)$$

and its solution is given by:

$$x = r + \frac{1}{c} W \left(\frac{c}{a} \exp(-cr) \right) \quad (28)$$

So, comparing (26) and (27), we have to identify:

$$c = 2, \quad a = -\frac{t}{2}, \quad r = \frac{1}{t} \quad (29)$$

and we find the solution of eq. (26) as:

$$u = \frac{1}{t} + \frac{1}{2} W \left(-\frac{4}{t} \exp \left(-\frac{2}{t} \right) \right) \quad (30)$$

Consequently:

$$m = ut = 1 + \frac{t}{2} W \left(-\frac{4}{t} \exp \left(-\frac{2}{t} \right) \right) \quad (31)$$

For $t \gtrsim 0$:

$$W \left(-\frac{4}{t} \exp \left(-\frac{2}{t} \right) \right) = -\frac{4}{t} \exp \left(-\frac{2}{t} \right) + \dots \quad (32)$$

where the higher order terms in the expression of W can be neglected [36]. Hence, we get:

$$m(t \gtrsim 0) \simeq 1 - 2 \exp\left(-\frac{2}{t}\right) \quad (33)$$

So, $m(t)$ cannot be written as a series expansion near the origin, as $t = 0$ is an essential singular point for this function. This mathematical aspect is unimportant for the physicist, as the correct low temperature dependence of the magnetization is not exponential, but power-like; it obeys the well-known "3/2 Bloch law" (see also the eqs. (10), (11) in Ch. 15 of [18], where the previous result, (33) of this preprint, was obtained under the implicit assumption that $m(0)$ is finite; the only advantage of the approach just described is that it does not make any assumption on $m(0)$).

Near the critical temperature $t_c = 1$, the magnetization behaves as

$$m(t \lesssim 1) \sim \sqrt{1-t} \quad (34)$$

So, for the whole interval $(0, 1)$, it seems convenient to write the magnetization in the form:

$$m(t) = \left(1 - 2 \exp\left(-\frac{2}{t}\right)\right) P_{1/2}^{(n)}(t) \sqrt{1-t} \quad (35)$$

where $P_{1/2}^{(n)}(t)$ can be approximated, as precisely as we want, with a polynomial of degree n . As

$$m(0) = 1 \rightarrow P_{1/2}^{(n)}(0) = 1 \quad (36)$$

we can presume for $P_{1/2}^{(n)}(t)$ the following form:

$$\begin{aligned} P_{1/2}^{(n)}(t) &= (1 + a_1 t + \dots + a_n t^n) = \\ &= \frac{m(t)}{\left(1 - 2 \exp\left(-\frac{2}{t}\right)\right) \sqrt{1-t}} \end{aligned} \quad (37)$$

The coefficients a_1, \dots, a_n can be obtained by solving a linear system of n equations, obtained for n couples of values $(t_0, m(t_0))$. The numerical value of $m(t_0)$ for a given t_0 can be obtained solving numerically the equation:

$$m(t_0) = \tanh \frac{m(t_0)}{t_0} \quad (38)$$

using (for instance) the FindRoot command of Mathematica. For $n = 7$, the aforementioned pairs of values $(t_0, m(t_0))$ might be those included in the following table:

| t_0 | $m(t_0)$ |
|-------|---------------------|
| 0.2 | 0.9999091217152326 |
| 0.4 | 0.9856238716346567 |
| 0.6 | 0.9073323166453099 |
| 0.8 | 0.7104117834878704 |
| 0.85 | 0.6295014763911393 |
| 0.9 | 0.525429512658009 |
| 0.95 | 0.37948520667808994 |

Solving the system of 7 linear equations generated by eq. (37) applied to each from the 7 above pairs, the polynomial $P_{1/2}^{(7)}(t)$ can be expressed as:

$$P_{1/2}(t) = 1 + 0.60683t - 0.90480t^2 + 5.9531t^3 - 11.705t^4 + \quad (39)$$

$$+ 13.950t^5 - 8.8174t^6 + 2.2928t^7$$

Finally, the reduced magnetization is:

$$m(t) = \left(1 - 2 \exp\left(-\frac{2}{t}\right)\right) \sqrt{1-t}. \quad (40)$$

$$\cdot (1 + 0.60683t - 0.90480t^2 + 5.9531t^3 - 11.705t^4 + 13.950t^5 -$$

$$- 8.8174t^6 + 2.2928t^7)$$

Let us remind ourselves that, looking for the form (35) of the solution of eq. (10), we applied actually an approach systematically used in order to find a physically acceptable solution of the Schroedinger equation. A wellknown example of such an approach might be the following: when we are solving the Schroedinger equation in a Coulombian field, we are looking for a solution which "behaves well" near origin and at the infinity. It is, in fact, similar to what we have done here, isolating the behaviour of $m(t)$ near $t = 0$ and $t = 1$.

The plot of the reduced magnetization $m(t)$ given by eq. (40) is given in Fig. 1.

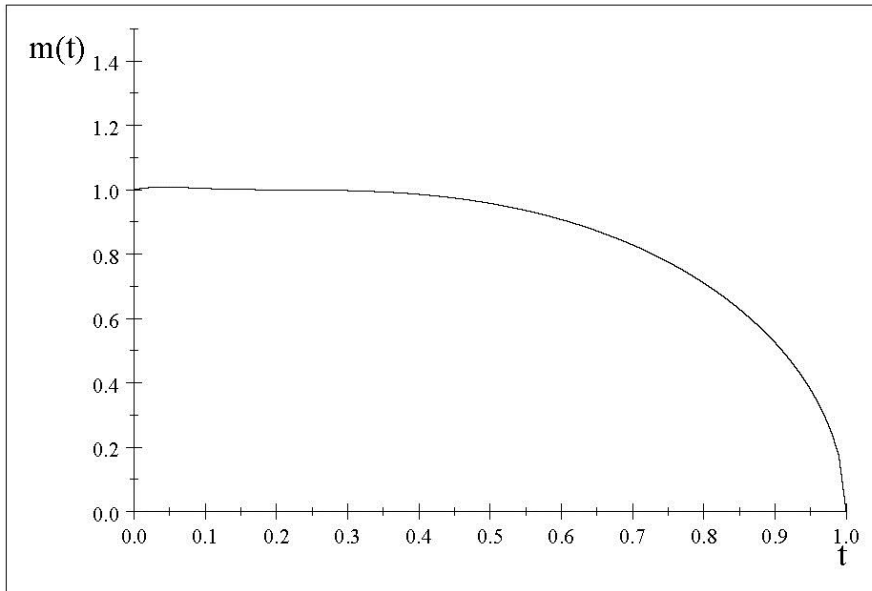


Fig. 1. The plot of $m(t)$ according to eq. (39).

If $m(t)$ satisfies (with a good approximation) the equation:

$$m(t) = \tanh \frac{m(t)}{t} \quad (41)$$

it will satisfy (with an equally good approximation) the equation:

$$m(t) \coth \frac{m(t)}{t} = 1 \quad (42)$$

The function $f(t) = m(t) \coth(m(t)/t)$, with $m(t)$ given by eq. (40) and the function $g(t) = 1$ are plotted in Fig. 2, for comparison.

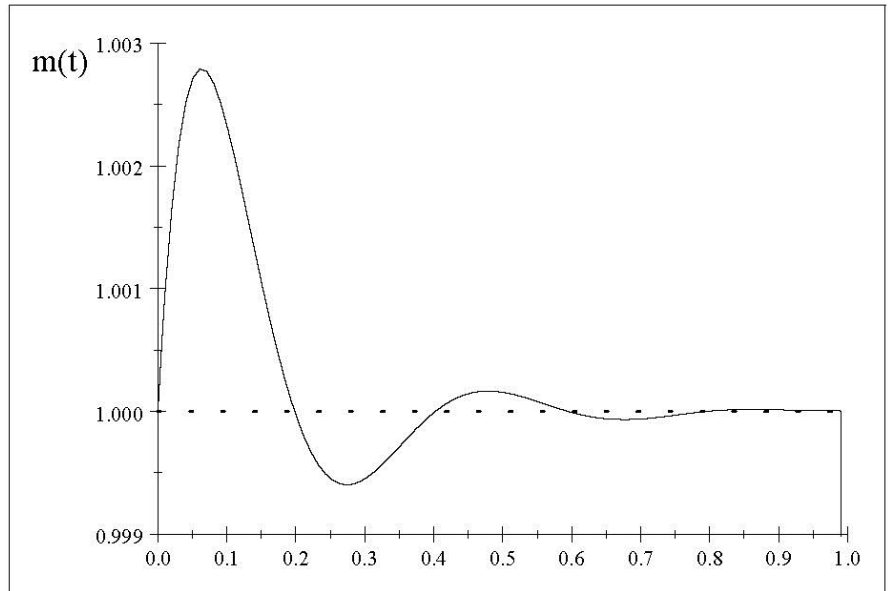


Fig. 2. The plot of $f(t) = m(t) \coth \frac{m(t)}{t}$ given by eq. (39) (solid) and $g(t) = 1$ (dotted).

It is easy to see that the approximation of $f(t)$ by $g(t)$ is excellent. The largest relative deviation, less than $3 \cdot 10^{-3}$, corresponds to a region of little physical interest, being far away from the critical point of the transition temperature, where the superposition with experimental values should be the most relevant.

In applications to experimental physics involving temperatures of hundred of Kelvins, the exponential factor in the expression of magnetization plays no role and instead of (35) we can look for a solution of the Weiss equation (10) of the form:

$$m(t) = Q_{1/2}^{(n)}(t) \sqrt{1-t} \quad (43)$$

where $Q_{1/2}^{(n)}(t)$ is a polynomial (of the same degree as $P_{1/2}^{(n)}(t)$).

Applying the same approach, outlined after eq. (37), we get the following expression for $Q_{1/2}(t)$:

$$Q_{1/2}(t) = 1 + 0.48248t + 0.377693t^2 + 1.66343t^3 - \quad (44)$$

$$-5.58315t^4 + 6.87009t^5 - 3.99752t^6 + 0.91907t^7$$

The precision of this simpler expression is still higher than the previous one: the error is less than 10^{-3} , for $t \simeq 0.1$.

Even more interesting is the fact that this approach can be applied to any Brillouin function B_S defined in (3), not only for $S = 1/2$. For an arbitrary S , the Weiss equation in zero magnetic field is given by the formula:

$$m(t) = B_S \left(\frac{m(t)}{t} \frac{3S}{S+1} \right) \quad (45)$$

and the reduced magnetization can be approximated by:

$$m(t) = Q_S(t) \sqrt{1-t} \quad (46)$$

For instance

$$Q_1^{(7)}(t) = (1 + 0.410582t + 1.40536t^2 - 3.36245t^3 + 4.34284t^4 - \\ -3.28348t^5 + 1.35735t^6 - 0.237194t^7) \quad (47)$$

$$Q_{3/2}^{(7)}(t) = (1 + 0.410721t + 1.65224t^2 - 5.60792t^3 + 9.67475t^4 - \\ -9.30572t^5 + 4.74404t^6 - 1.00258t^7) \quad (48)$$

$$Q_2^{(7)}(t) = (1 + 0.453772t + 1.34346t^2 - 5.51081t^3 + 10.5506t^4 - \\ -10.8288t^5 + 5.77001t^6 - 1.25923t^7) \quad (49)$$

$$Q_{5/2}^{(7)}(t) = (1 + 0.508037t + 0.813671t^2 - 4.26886t^3 + 9.01576t^4 - \\ -9.75394t^5 + 5.36827t^6 - 1.19731t^7) \quad (50)$$

with a maximum relative deviation smaller than $1.5 \cdot 10^{-3}$, also for $t \simeq 0.1$; for larger values of t , the approximation is much better. For instance, if $t > 0.4$, the maximum relative deviation is at least two orders of magnitude better.

4 The magnetization in the presence of an external magnetic field

If the magnetic field is non-zero, eq. (8) can be written as:

$$\tanh \left(\frac{m(t_0, h)}{t_0} + h \right) = t_0 \left(\frac{m(t_0, h)}{t_0} + h \right) - t_0 h \quad (51)$$

or, putting

$$u = \frac{m(t_0, h)}{t_0} + h \quad (52)$$

as:

$$\tanh u = t_0 (u - h) \quad (53)$$

or, equivalently:

$$e^{2u} \frac{u - h - \frac{1}{t_0}}{u - h + \frac{1}{t_0}} = -1 \quad (54)$$

According to (16), (17) the solution of this equation is:

$$u = \frac{1}{2} W \left(2h + \frac{2}{t_0}; 2h - \frac{2}{t_0}; -1 \right) \quad (55)$$

so, finally we get:

$$m(t_0, h) = \frac{t_0}{2} W \left(2h + \frac{2}{t_0}; 2h - \frac{2}{t_0}; -1 \right) - h \quad (56)$$

or, using the r -Lambert function and eq. (21):

$$m(t_0, h) = W_{\exp(-2h-2/t_0)} \left(\frac{4}{t_0} e^{-2h-2/t_0} \right) - h(1-t_0) + 1 \quad (57)$$

The critical isotherm is obtained making in the previous formula the replacement $t_0 \rightarrow 1$:

$$m(1, h) = W_{\exp(-2(h-1))} \left(4e^{-2(h-1)} \right) + 1 \quad (58)$$

For reasons explained in the previous section, these solution are quite inconvenient for practical purposes. So, our next goal is to obtain an alternative expression for $m(t, h)$, using simpler functions - actually, a series expansion in powers of h , whose coefficients are known, being expressed as elementary functions of t .

With:

$$\zeta(t, h) = \frac{m(t, h)}{t}, \quad m(t, h) = t\zeta(t, h) \quad (59)$$

the equation of state (8) becomes:

$$t\zeta(t, h) = \tanh \left(\zeta(t, h) + \frac{h}{t} \right) \quad (60)$$

A closed form of $m(t, 0)$ was obtained in the previous section, eq. (35), so an accurate analytic approximation of the function $\zeta(t, 0)$ is known, at least down to enough low t . Differentiating (60) with respect to h , and putting

$$\zeta(t, h) + \frac{h}{t} = \xi \quad (61)$$

we get:

$$t \frac{\partial \zeta(t, h)}{\partial h} = (1 - t^2 \zeta^2(t, h)) \left(\frac{\partial \zeta(t, h)}{\partial h} + \frac{1}{t} \right)$$

and:

$$\frac{\partial \zeta(t, h)}{\partial h} = \frac{1}{t} \frac{(1 - t^2 \zeta^2(t, h))}{(-1 + t + t^2 \zeta^2(t, h))} \quad (62)$$

Consequently:

$$\left. \frac{\partial \zeta(t, h)}{\partial h} \right|_{h=0} = \frac{1}{t} \frac{(1 - t^2 \zeta^2(t, 0))}{(-1 + t + t^2 \zeta^2(t, 0))} \quad (63)$$

So, the value of the previous expression is known, as the function $\zeta(t, 0)$ is known, e.g. via $m(t, 0)$ provided by (40). This property of the derivative remains valid in any order; consequently, we can write

$$\zeta(t, h) = \zeta(t, 0) + \left. \frac{\partial \zeta(t, h)}{\partial h} \right|_{h=0} h + \frac{1}{2} \left. \frac{\partial^2 \zeta(t, h)}{\partial h^2} \right|_{h=0} h^2 + \dots \quad (64)$$

In this way, we obtain a series expansion for $m(t, h)$, according to (52), valid for small values of h . It should have in mind, however, that we did not investigate the convergence of this series.

5 Weiss equation and inverse Brillouin functions

As is easy to see, applying the inverse Brillouin function B_S^{-1} in the both sides of the equation of state (1), the thermodynamic variables can be separated [4]:

$$H = \frac{k_B}{\bar{\mu}J} T \cdot B_S^{-1} \left(\frac{M}{M_0} \right) - \lambda M \quad (65)$$

This is the simplest illustration of the usefulness of the inverse Brillouin functions; other examples can be found in [37].

Coming back to the mathematical aspects, the inverse function is singular, $B_\sigma^{-1}(x) \rightarrow \infty$, in the asymptotic limit, when $x \rightarrow 1$, as we shall see. With the substitutions:

$$z = e^{\frac{x}{\sigma}}, \quad x = \sigma \ln z \quad (66)$$

the direct functions B_σ become algebraic expressions:

$$B_\sigma(z) = \frac{1}{2\sigma} \frac{(2\sigma + 1)(z^{2\sigma+1} + 1)(z - 1) - (z^{2\sigma+1} - 1)(z + 1)}{(z^{2\sigma+1} - 1)(z - 1)} \quad (67)$$

where we wrote (abusively) $B_\sigma(z)$ instead of $B_\sigma(\sigma \ln z)$, to avoid too complicate notations.

To invert the Brillouin function $B_\sigma(z)$ means essentially to find the convenient root $z_\sigma(y)$ of the equation:

$$B_\sigma(z) = y \quad (68)$$

Actually, the inverse Brillouin function is:

$$B_\sigma^{-1}(y) = \sigma \ln z_\sigma(y) \quad (69)$$

With (67), (68), the equation satisfied by z_σ is:

$$\sigma(1-y)z^{2\sigma+2} - (1+\sigma(1-y))z^{2\sigma+1} + (1+\sigma(1+y))z - \sigma(1+y) = 0 \quad (70)$$

so a tetranomial equation (i.e. containing only four terms) with quite simple coefficients. Although the roots of tetranomial equations can be, in principle, obtained exactly [37], [38], no formula for solving eq. (70), in the general case, is available in literature. So, in practical cases, it is unavoidable to look for approximants of B_σ^{-1} , and the first step to be done is to obtain its asymptotic expression, i.e. the value of $z(y)$ for $y \rightarrow 1$. Actually, we shall put $y = 1$ in the coefficients of (70), excepting the dominant term:

$$2\sigma(1-y)z^{2\sigma+2} - 2z^{2\sigma+1} + (4\sigma+2)z - 4\sigma = 0 \quad (71)$$

Substituting:

$$z = \frac{a}{1-y} \quad (72)$$

we get:

$$z_\sigma(y \rightarrow 1) = \frac{1}{\sigma(1-y)} \quad (73)$$

So, the asymptotic form of the inverse Brillouin function is:

$$B_\sigma^{-1}(y \rightarrow 1) = \sigma \ln z_\sigma(y) = \sigma \ln \frac{1}{\sigma(1-y)} \rightarrow \sigma \ln \frac{1}{1-y} \quad (74)$$

as the constant term $-\sigma \ln \sigma$ is negligible, compared to the singular one. The same result has been obtained by Kröger [8], using a different approach. It is compatible with the well-known exact result:

$$B_{1/2}^{-1}(y) = \tanh^{-1}(y) = \frac{1}{2} \ln \frac{1+y}{1-y} \quad (75)$$

(we shall use, in the rest of the paper, the logarithmic expression of the inverse hyperbolic tangent, to avoid confusions) and to the other simple exact result, given by Kröger [8]:

$$B_1^{-1}(y) = \ln \left(\frac{y + \sqrt{4 - 3y^2}}{2(1 - y)} \right) \quad (76)$$

where we removed a typo in eq. (D.7) of [8]; see also [39].

We shall define, for the rest of this paper, the asymptotic form of the inverse Brillouin function by:

$$B_\sigma^{-1}(y)|_{\text{asympt}} = \sigma \ln \frac{1}{1 - y} \quad (77)$$

Kröger [8] produced an elegant, detailed and systematic study of the inverse Brillouin functions, showing that they must satisfy several conditions. One of them is:

$$B_\sigma^{-1}(y \rightarrow 1) = \sigma \ln \frac{1 + y}{1 - y} \quad (78)$$

This formula gives the asymptotic behavior. Near the origin:

$$B_\sigma^{-1}(y \rightarrow 0) = \frac{3\sigma}{1 + \sigma} y + O(y^3) \quad (79)$$

The symmetry condition means:

$$B_\sigma^{-1}(-y) = -B_\sigma^{-1}(y) \quad (80)$$

Another relation is a constraint, concerning the integrability, eq. (3) of [8].

A conclusion of Kröger's analysis is that the most convenient approximant of the inverse Brillouin function is:

$$\widetilde{B}_\sigma^{-1}(y) = \frac{1}{2} \frac{15 - 11(1 - \varepsilon)(1 + 2\varepsilon)y^2}{5 + 10\varepsilon - (1 - \varepsilon)[5 + 11\varepsilon(1 + 2\varepsilon)]y^2} \ln \frac{1 + y}{1 - y}, \quad \varepsilon = \frac{1}{2\sigma} \quad (81)$$

This is a remarkably simple and accurate result (maximum relative errors from 1.5% for $\sigma = 3/2$ to 0.6% for $\sigma = 5$ and to 0.35% for $\sigma = 10$), with increasing precision for larger indices. The accuracy of this formula can be, in principle, increased, replacing the quadratic polynomials in (81) with quartic ones; the odd powers are excluded for symmetry reasons, see eq. (80). However, the expression of approximants modified in this way becomes quite complicated.

With the goal of further increasing the accuracy of the approximants of the inverse Brillouin functions, we shall propose now an alternative, more pragmatic approach, to Kröger's one. The essential step is to choose for $\widetilde{B}_\sigma^{-1}(y > 0)$ the simplest form, and to satisfy the symmetry condition (80) defining

$$\widetilde{B}_\sigma^{-1}(y < 0) = -\widetilde{B}_\sigma^{-1}(-y)$$

Consequently, we shall consider that the function (77) is the most convenient asymptotic form of B_σ^{-1} . Actually, (78) was adopted by Kröger because its

symmetry property, but we avoided this restriction, by introducing the definition (??). Let us notice that

$$B_{\sigma}^{-1}(y \simeq 0)|_{\text{asympt}} \simeq \sigma y + \dots$$

The slope of the inverse Brillouin function in the origin is (see (79)):

$$\frac{3\sigma}{1+\sigma}$$

consequently:

$$B_{\sigma}^{-1}(y \simeq 0) = \frac{3}{1+\sigma} B_{\sigma}^{-1}(y \simeq 0)|_{\text{asympt}}$$

So, we can presume that a reasonable approximant of the inverse Brillouin function is:

$$\widetilde{B_{\sigma}^{-1}}(y) = \frac{3}{1+\sigma} P_{\sigma}(y) B_{\sigma}^{-1}(y)|_{\text{asympt}} \quad (82)$$

with P_{σ} is a smooth function, whose values at the ends of the interval of definition can be obtained as follows:

$$B_{\sigma}^{-1}(y \simeq 0) = \frac{3}{1+\sigma} P_{\sigma}(0) \sigma y = \frac{3\sigma}{1+\sigma} y$$

consequently:

$$P_{\sigma}(0) = 1 \quad (83)$$

Also:

$$B_{\sigma}^{-1}(y \simeq 1) = \frac{3}{1+\sigma} P_{\sigma}(1) B_{\sigma}^{-1}(y \simeq 1)|_{\text{asympt}}$$

consequently:

$$P_{\sigma}(1) = \frac{1+\sigma}{3} \quad (84)$$

In other words:

$$\widetilde{B_{\sigma}^{-1}}(y) = \frac{3\sigma}{1+\sigma} P_{\sigma}(y) \ln\left(\frac{1}{1-y}\right), \quad (85)$$

with $P_{\sigma}(x)$ satisfying the conditions (84), (85).

If $\sigma = 2$, $P_2(0) = P_2(1) = 1$ and it seems interesting to check the brutal approximation $P_2(x) \simeq 1$; this gives:

$$\widetilde{B_2^{-1}}(y) \simeq 2 \ln\left(\frac{1}{1-y}\right) \quad (86)$$

For the exact functions,

$$B_2(B_2^{-1}(y)) = y \quad (87)$$

and

$$\frac{1}{y}B_2(B_2^{-1}(y)) - 1 = 0 \quad (88)$$

If $B_2^{-1}(y)$ is replaced in (88) by the approximation (86), one gets:

$$\frac{1}{y}B_2(\widetilde{B_2^{-1}}(y)) - 1 = \frac{1}{2}y - 1.1y^2 + 0.8y^3 - 0.2y^4 \lesssim 0.05 \text{ if } 0 < y < 1 \quad (89)$$

so we can conclude that the error of the approximation (87) is about 5%, so comparable with Arrott's approximation [4].

The eq. (89) illustrates the meaning of the expression "error of an approximant", as used in the present paper. If $B_2^{-1}(y)$ in (88) or (89) is an approximant, the error in fulfilling the identity (88) is considered to be the error of this approximant.

Encouraged by this result, we shall presume that P_σ is a smooth function, which can be approximated by a polynomial. For any y_j , $B_\sigma^{-1}(y_j)$ can be obtained solving numerically (for instance, with *FindRoot* in Mathematica) the equation in x_j :

$$B_\sigma(x_j) = y_j \rightarrow x_j = B_\sigma^{-1}(y_j) \quad (90)$$

In this way, we can find the values of P_σ in an arbitrary number of points y_j , $j = 1, 2, \dots, n$

$$P_\sigma(y_j) = \frac{1 + \sigma B_\sigma^{-1}(y_j)}{3\sigma \ln\left(\frac{1}{1-y_j}\right)} \quad (91)$$

A polynomial fitting the points $(y_j, P_\sigma(y_j))$ can be easily obtained using the *Fitting curves to data* command in Mathematica. Choosing a large enough number of points $(y_j, P_\sigma(y_j))$, we can obtain a good enough accuracy for the approximant (85), according to our specific goal.

The main advantages of this method are the accuracy, and the availability of an analytical formula, for each σ separately. Actually, its accuracy can be increased as much as needed, increasing the number of intermediate points y_j . Its main disadvantage might be that the specific expression of the polynomial $P_\sigma(y)$ changes if the distribution of points $(y_j, P_\sigma(y_j))$ changes. The problem of the stability of the polynomial $P_\sigma(y)$ when the distribution of points changes is not discussed this paper; however, it was studied by Tolea, who demonstrated that, if the number of interpolation points increases (until several millions, in the cases studied by Tolea), the first digits of the coefficients of the polynomial P_σ (the first four, in the aforementioned cases) do not change, if the interpolation becomes more dense [40].

6 Numerical example

To illustrate how this approach works, we shall obtain explicitly an approximant for $B_{3/2}^{-1}$. It can be calculated exactly, solving a cubic equation, but the expression got in this way is too complicated to be used in practical applications. To start, we shall choose only 10 points y_j inside the interval $(0, 1)$, namely $y_1 = 0.1, y_2 = 0.2, \dots, y_9 = 0.9, y_{10} = 0.95$ and shall calculate the corresponding values $P_{3/2}(y_j)$ according to (90), (91)

For instance, using (90), $B_{3/2}^{-1}(0.1)$ is the root of the equation $B_{3/2}(x_1) = 0.1$, i.e. 0.180739, so $B_{3/2}^{-1}(0.1) = 0.180739$, and, according to (91), $P_{3/2}(y_j) = 0.953$; the point $(0.1, 0.953)$ belongs to the graph of $P_{3/2}(y)$. Similarly, we find the values $P_{3/2}(y_j)$, corresponding to points $y_j = 0.2, \dots, 0.95$. The points $(0, 1)$ and $(1, 0.033)$ are obtained using equations 84 and 85, respectively.

After that, using the "Fit" command in Mathematica:

```
Fit[{{0, 1}, {0.1, 0.953}, {0.2, 0.91133}, {0.3, 0.874}, {0.4,
0.84042}, {0.5, 0.81032}, {0.6, 0.78348}, {0.7, 0.7604}, {0.8,
0.74249}, {0.9, 0.73468}, {0.95, 0.74033}, {1, 0.83333}},
Table[x^n, {n, 0, 30}], y]
```

we get the following expression for the polynomial $P_{3/2}(y) = 1 + \sum a_n y^n$:

$$P_{3/2}(y) = 1 - 0.499043y + \dots + \mathcal{O}(y^{31}) \quad (92)$$

where the values of the coefficients a_n , $2 \leq n \leq 30$, given by the previous command, has been omitted, in order to save space. However, the omitted coefficients can be obtained via the last command in the Appendix, with $\sigma = 3/2$.

The error of this approximation is less than 0.03% for $0 < y < 0.8$, less than 0.015% for $0.8 < y < 0.95$ and less than 0.2% for $0.95 < y < 1$. It is an order of magnitude smaller than the error of any approximant in use and it can be further reduced by increasing the number of points (x_j, y_j) .

It is important to notice that the pairs of values (y_j, x_j) similar to those obtained using (90), for instance $(0.1, 0.180739)$ can be also obtained using Kroger's formula (81) for the approximant of the inverse Brillouin function. So, with (81), $\widetilde{B_{3/2}^{-1}}(0.1) = 0.1807386\dots$ (the exact value is 0.1807393...), and $B_{3/2}(0.1807386) = 0.09999957\dots$. So, instead of using the pair $(0.1, 0.180739)$, we can use the pair $(0.09999957, 0.1807386)$, in order to obtain the interpolation points for the polynomial $P_{3/2}$. In this last example, we used a larger number of decimals than in the others calculations, in order to make visible the excellent accuracy of Kroger's approximant (81).

7 Conclusions

Using recent results of the theory of generalized Lambert functions, exact expressions for the magnetization of a Weiss ferromagnet, with zero or non-zero

external magnetic field, are obtained. Accurate and simple approximants for the exact expressions are provided, for any value of the spin indices. The analysis was extended to inverse Brillouin functions, where a simpler and more precise approximant (compared to those used in literature) was proposed.

Acknowledgement 1 *The author acknowledges the financial support of IFIN-HH - ANCSI project PN 16 42 01 01/2016 and to the IFIN-HH - JINR Dubna grant 04-4-1121-2015/17.*

References

- [1] M. Kochmanski, T. Paszkiewicz, S. Wolski, *Currie-Weiss magnet - a simple model of phase transition*, Eur. J. Phys. 34 (2013) pp.1555-1573
- [2] Mezö, I. and Baricz, A., *On the generalization of the Lambert W function*, arXiv: 1408.3999v2 (2014)
- [3] Mugnaini, G., *Generalization of Lambert W-function, Bessel polynomials and transcendental equations*, arXiv:1501.00138v2 (2015)
- [4] A. S. Arrott, *Approximations to Brillouin functions for analytic descriptions of ferromagnetism*, J. Appl. Phys. 103 (2008) 07C715 (2pp)
- [5] J.Takacs: *Mathematics of Hysteretic Phenomena: The T(x) Model for the Description of Hysteresis*, COMPEL International J of Comp and Math in Electrical and Electronic Engineering, v20 n4, 2001, pp 1002-1014
- [6] J.Takacs: *Approximations for Brillouin and its reverse function*, COMPEL International J of Comp and Math in Electrical and Electronic Engineering, v35 n6, 2016, pp 2095-2099
- [7] A. S. Johal and D. J. Dunstan: *Energy functions for rubber from microscopic potentials*, J. Appl. Phys. 101 (2007) 084917 (8pp)
- [8] M. Kröger: *Simple, admissible, and accurate approximants of the inverse Langevin and Brillouin functions, relevant for strong polymer deformations and flows*, J. Non-Newtonian Fluid Mech. 223 (2015) pp. 77-87
- [9] R. Jedynek, *Approximation of the inverse Langevin function revisited*, Rheol. Acta 54, (2015) pp. 29-39
- [10] R. Jedynek, *New facts concerning the approximation of the inverse Langevin function*, J. Non-Newtonian Fluid Mech. (2017), <https://doi.org/10.1016/j.jnnfm.2017.09.003>
- [11] R. Jedynek, J. Gilewicz, *Magic efficiency of approximation of smooth functions by weighted means of two $\frac{1}{N}$ -point Padé approximants*, Ukr. Mat. J. **70**, 1192 (2018)

- [12] R. Jedynak, A comprehensive study of the mathematical methods used to approximate the inverse Langevin function, *Math. Mech. Solids*, 1–25, DOI: 10.1177/1081286518811395
- [13] R. Petrosyan, *Improved approximations for some polymer extension models*, *Rheol. Acta* 56 (2017) pp. 21-26
- [14] Suehrcke, H., McCormick, P.G., 1987. An approximation for of the fractional time distribution of daily clearness index, *J. Solar Energy* 39 (1987) pp. 369-370
- [15] G. Keady, *The Langevin function and truncated exponential distributions*, arXiv:1501.02535v1 (2015)
- [16] V. Barsan, New results concerning the generalized Lambert functions and their applications to solar energy conversion and nanophysics, poster presentation at the workshop Spectroscopy and Dynamics of Photoinduced Electronic Excitations, ICTP Trieste, Italy, May 8-12, 2017, DOI: 10.13140/RG.2.2.15123.89124
- [17] H. E. Stanley, *Introduction to phase transitions and critical phenomena*, Oxford University Press, Oxford, 1971
- [18] Ch. Kittel, *Introduction to solid state physics*, John Wiley & Sons, New York, 8th edition, 2005
- [19] K. H. J. Buschow and F. R. de Boer, *Physics of Magnetism and Magnetic Materials*, Kluwer Academic Publishers, New York, Boston, Dordrecht, London, Moscow, 2004
- [20] V. Kuncser, P. Palade, A. Kuncser, S. Greculeasa, and G. Schinteie, *Engineering Magnetic Properties of Nanostructures via Size Effects and Interphase Interactions*, in *Size effects in nanostructures, Basics and Applications*, V. Kuncser and L. Miu, eds., Springer Verlag, Berlin, Heidelberg, 2014, pp. 169-237
- [21] I. Mezö and G. Keady, *Some physical applications of generalized Lambert functions*, *Eur.J.Phys.* 37 (2016) 065802 (10pp)
- [22] Tamvakis, K.: *Problems of quantum mechanics*, Cambridge University Press (2005)
- [23] Rabinovitch, A., Negative energy states of "inverted" delta potentials: influence of boundary conditions, *Am.J.Phys.*, **53**, 768 (1985)
- [24] N. Bovenzi, M. Breitzkreiz, T. E. O'Brien, J. Tworzyd and C. W. J. Beenakker: Twisted Fermi surface of a thin- lm Weyl semimetal, arXiv:1707.01038v2, 19 Sept. 2017
- [25] L. Bányai, P. Gartner: Meissner effect in gauge-invariant, self-consistent pairing theories, *Phys.Rev.* **B29**, p. 4992, 1984

- [26] Ladislaus Bányai: Profile in motion (Ed.: V. Barsan), Horia Hulubei Publishing House, 2018, p. 179
- [27] R. A. Leathers, N. J. McCormick, Closed-Form Solutions for Transcendental Equations of Heat Transfer, *J. Heat transfer*, vol 118 1996 pp. 970-973
- [28] C. E. Siewert, C. J. Essig: An Exact solution of a molecular Field Equation in the Theory of Ferromagnetism, *ZAMP*, vol. 24, p. 281
- [29] N. I. Muskhelishvili: Singular integral equations, Noordhoff, Groningen, 1953
- [30] V. Barsan: Siewert solutions of transcendental equations, generalized Lambert functions and physical applications, *Open Physics (former Central European Journal of Physics)* 2018
- [31] V.V. Pogosov, V.P. Kurbatsky and E.V. Vasyutin: Energetics of metal slabs and clusters: The rectangular box model, *Phys. Rev. B* 71 (2005) p.195410
- [32] V. Barsan: Square wells, quantum wells and ultra-thin metallic films, *Philos. Mag.*, 2014, Vol. 94, No. 2, 190-207, <http://dx.doi.org/10.1080/14786435.2013.845313>
- [33] V. Barsan, New applications of the Lambert and generalized Lambert functions to ferromagnetism and quantum mechanics, arXiv:1611.01014v2
- [34] O. F. de Alcantara Bonfim, D. J. Griffiths: Exact and approximate energy spectrum for the finite square well and related potentials, *Am. J. Phys.* **74**, 43 (2006)
- [35] V. Barsan: Algebraic approximations for transcendental equations with applications in nanophysics, *Philos. Mag.* **95** 3023-38 (2015)
- [36] R. M. Corless, D. J. Jeffrey: On the Wright ω function, <http://www.orcca.on.ca/TechReports/2000/TR-00-12.pdf> (2000)
- [37] I. Katriel, Continued-fraction approximation for the Brillouin function, *Phys.Stat. Sol.* 189 (1987) 307
- [38] Passare, M., Tsikh, A., in: O.A. Laudal, R.Piene: The legacy of Niels Henrik Abel - The Abel Bicentennial, Oslo, Springer (2002)
- [39] V. Barsan: Simple and accurate approximants of inverse Brillouin functions, *J. Magn. Magn. Mat.*, <https://doi.org/10.1016/j.jmmm.2018.10.058>, 2018
- [40] M. Tolea, to be published

Exact and approximate analytical solutions of Weiss equation of ferromagnetism. Experimental aspects (II)

Victor Kuncser
INFM, Str. Atomistilor 105, 077125 Magurele, Romania

Abstract

The experimental relevance of theoretical results obtained in the previous paper, (I), mainly for the determination of the Curie temperature, is discussed.

1 Introduction

This paper is the second one of a pair of studies devoted to the applications of the new results of the generalized Lambert function in ferromagnetism. The previous paper (I), is devoted to theoretical aspects [1]. This one, paper (II), is devoted to experimental aspects.

2 Discussion on experimental implications

From the experimental point of view, a direct expression of the magnetization versus temperature and field might be of high interest for getting material dependent parameters of ferromagnetic materials (magnetic moment and spontaneous magnetization, Curie temperature, molecular field constant and exchange integral, etc.) through a suitable fitting of the experimental data. It is worth to mention that case of ferrimagnetic (or even no completely compensated antiferromagnets, e.g. due to structural/interfacial/surficial defects) can be treated in a similar manner by a simple association of a finite magnetic moment to a formula unit. Some real (and very often defect) magnetic systems could present an enough high magnetic disorder temperature, in order to be completely analyzed within the temperature range of sensitive magnetometers (e.g. SQUIDS). Mainly these are the cases where a complete estimation of the material parameters can become effective by fitting the experimental data obtained over a narrower range of field and temperature via the above discussed theoretical expressions.

A proof of concept on how this procedure can be experimentally implemented for magnetization measurements versus temperature will be provided for one of

the above analyzed cases, corresponding to a solid state system with $S = 1/2$ (a quenching of the orbital magnetic moment is assumed). To note that the local magnetic moment of the magnetic entity (atom, molecule, formula unit) can be verified from the saturation magnetization at very low temperatures which also approaches the spontaneous magnetization M_0 . Hence, the experimental function $m(t, h)$ can be obtained if T, H and T_c are known. The first two are experimental parameters, whereas the last one can be obtained via specific magnetization measurements versus temperature, e.g. as the temperature where the spontaneous magnetization drops to zero. Very often, such measurements have to be done at temperatures much higher than the room temperature, involving therefore additional higher temperature options for usual magnetometers. Instead, the Curie temperature can be obtained by fitting the experimental dependence $M(T)$, as collected under a low enough applied magnetic field, over a much reduced range of temperatures. The aforementioned general relation (11) of (I), written under the form $m(t, h) = t\zeta(t, h)$ should be used in this respect.

However, in order to achieve this task, a series of experimental conditions should be fulfilled. As a first condition, the system might respect the overall Brillouin dependence of magnetization versus temperature, that is, size or anisotropy related magnetization relaxation phenomena (e.g. superparamagnetic behavior) should be avoided. A second condition is related to the removal of magnetic domains in the system, condition which might be fulfilled by measuring the magnetization versus temperature under convenient constant applied magnetic fields. In the case of quite soft magnetic materials the measurements can be done in low enough magnetic fields (e.g. of magnetic induction as low as $0.1T$), in order to keep only the term proportional to h in relation (11) of (I). Accordingly, the following experimental steps are proposed. The $M(H)$ curve at the lowest temperature (e.g. $2K$) should be initially obtained for estimating the saturation field and the saturation magnetization M_0 . Then, the dependence $M(T)$ can be obtained under an applied field higher than the saturation field and up to the maximum temperature of the device (e.g. $400K$ for a SQUID). According to Figs. 1 and 2, the most reliable values for T_c might be obtained if the maximum experimental temperature will overpass at least 60% from T_c . That is, for a maximum measuring temperature of $400K$, a Curie temperature of about $700K$ may be determined with acceptable accuracy.

The procedure of determining the transition temperature is the following. The experimental ratio $M(T, H)/M_0$ will be represented versus $t = T/T_c$ for a set of T_c values (e.g. $500K, 550K, 600K, 750K, 800K$). In this way, the experimental representations of $m(t, h)$ versus t will be obtained for different values of T_c . The theoretical representations of $m(t, h)$ via the relation $m(t, h) = t\zeta(t, h)$ with $\zeta(t, h)$ given by eq. (64) of (I) will be obtained for the same set of T_c values. In a first approximation, T_c is estimated as that temperature value in the considered set corresponding to the best superposition between the experimental and the theoretical $m(t, h)$ curves. The procedure can be repeated for a new set of T_c values (with a better temperature discretization, e.g. of $10K$) around the first approximation until the desired precision of T_c is obtained.

It is also to mention that actually there are experimental techniques providing parameters proportional to the spontaneous magnetization. Among them, the local techniques of ^{57}Fe Mossbauer spectroscopy is extremely powerful in following the temperature variation of the Fe magnetic moment on each Fe phase (the hyperfine magnetic field, B_{hf} as specific parameter is proportional in certain circumstances to the magnitude of the Fe magnetic moment and hence with the spontaneous magnetization attributed to that Fe phase). Being a local techniques seeing directly the magnitude of the magnetic moment, it does not involve any applied magnetic field and therefore, the simplest equation (43) can be used as reflecting the experimental temperature dependence of the ratio $m(t) = B_{hf}(T)/B_{hf}(T = 0)$.

3 Conclusions

A proof of concept for direct series-expansion solutions of the Weiss equation of ferromagnetism is provided. Even the concept is exemplified in case of non-zero magnetic field for a magnetic system with $S = 1/2$, it works in principle also for systems with enhanced S values, with the mention that in that case the Brillouin function will replace the tanh function, with direct implications on its derivatives. Also the spontaneous magnetization and Curie temperature will depend specifically on S , which might become an additional fitting parameter in the final expression of magnetization. The general solution of the reduced magnetization in applied field is always expressed as function of the temperature dependent solution of the spontaneous magnetization in the absence of the applied field. Specific procedures to use the developed expressions in case of magnetization or Mossbauer spectroscopy measurements are also mentioned.

Acknowledgement 1

The author acknowledges the financial support of PN16-480102 Project.

References

- [1] V. Barsan, Exact and approximate analytical solutions of Weiss equation of ferromagnetism. Theoretical aspects (I), *previous paper of this volume*.

Part II. Abstracts of other presentations

Heterostructures realized on surfaces of ferroelectric thin films

Nicoleta G. Apostol, Liviu C. Tănase, Laura E. Abramiuc, Dana G. Popescu, Marius A. Hușanu, Ioana C. Bucur, Ruxandra M. Costescu, George A. Lungu, Cristian A. Tache, Ana-Maria Trandafir, Cristina F. Chirilă, Luminița M. Hrib, Lucian Trupină, Raluca F. Negrea, Lucian Pintilie, and Cristian M. Teodorescu

*National Institute of Materials Physics, Atomîștilor 405A, 077125 Măgurele
– Ilfov, Romania*

This contribution will discuss special features exhibited by heterostructures realized on ferroelectric surfaces, when thin metal layers or carbon graphene-like layers are deposited by molecular beam epitaxy. We will introduce photoelectron spectroscopy as a principle tool [1], allowing one to evaluate the substrate quality (composition), the contamination degree, the amount of deposited material, and the surface or interface band bending [2,3]. Special attention will be given to the need to work on atomically clean substrates [4], and to the need to use complementary *in situ* characterization methods, such as low energy electron diffraction (LEED) [5]. For a clean ferroelectric thin film, the single domain state is realized when sufficient charge (mobile or ionized impurities) may be accommodated near its surface or bottom interface to compensate the depolarization field, a phenomenon which will be denoted henceforth as *intrinsic screening* [6–8]. When a conductive layer is deposited on top, the screening may be partly or totally realized using charges from this conductive layer, which will be denoted as *extrinsic screening* [6,9]. Indeed, some evolution of the core levels with metal deposition may nowadays be interpreted within this model [10]. Moreover, deposition on metal films may induce out-of-plane polarization due, again, to additional electrons contributing to the screening [11].

In the case of graphene layers, due to the zero bandgap character of this material, the carriers used for screening may be easily switched from electrons to holes. This induces a hysteretic variation of the in-plane resistance of graphene-like layers as function on the polarization of the substrate, adjustable by a gate voltage [9]. In fact, the first experiments performed under air with transferred graphene, without any chemical characterization of the surfaces involved, exhibited rather a ‘anti-hysteresis’ behaviour, in which the sense of the hysteresis is covered in the opposite sense with respect to what is expected from basic considerations [12–14] (only at ultralow temperature a correct ‘hysteresis’ was reported [14]). The explanation pointed on the influence of adsorbate molecules,

which may be cyclically be adsorbed or desorbed, as function of the gate voltage. Only recently, graphene-like layers were synthesized in ultrahigh vacuum, without contaminants [15]. In this contribution we will also present the very first results of *in situ* conduction measurements on these heterostructures, where both 'hysteretic' and 'anti-hysteretic' behaviour are recorded, depending on the carbon coverage. A qualitative model will be introduced to explain these new data, taking into account, for ultrathin layers, conduction occurring both in graphene (carriers induced to realize *extrinsic compensation* of depolarization fields) and on the surface of the ferroelectric film (using mobile carriers which realize the *intrinsic compensation*). This also demonstrates indirectly that the detected 'anti-hysteresis' in Refs. [12–14] was due to contaminant molecules.

Hence, new correlations may be foreseen between the ferroelectric state of a thin film and in-plane conduction or sensing properties, which may be used in applications. Also, the stabilization of the ferroelectric state by some metals must be taken into account for applications where the robustness of the ferroelectric state is important.

References

- [1] S. Hüfner, Photoelectron Spectroscopy: Principles and Applications, 3rd Ed., Springer, Berlin, 2003.
- [2] H. Sezen and S. Suzer, XPS for chemical- and charge-sensitive analyses, *Thin Solid Films* **534**, 1–11 (2013).
- [3] N. G. Apostol, L. E. Stoflea, G. A. Lungu, C. Chirila, L. Trupina, R. F. Negrea, C. Ghica, L. Pintilie, and C. M. Teodorescu, Charge transfer and band bending at Au/Pb(Zr,Ti)O₃ interfaces investigated by photoelectron spectroscopy, *Applied Surface Science* **273**, 415–425 (2013).
- [4] L.C. Tănase, N.G. Apostol, L.E. Abramiuc, C.A. Tache, L. Hrib, L. Trupină, L. Pintilie, and C.M. Teodorescu, Ferroelectric triggering of carbon monoxide adsorption on lead zirco-titanate (001) surfaces, *Scientific Reports* **6**, 35301(18 pp.) (2016).
- [5] C. M. Teodorescu, L. Pintilie, N. G. Apostol, R. M. Costescu, G. A. Lungu, L. Hrib, L. Trupină, L. C. Tănase, I. C. Bucur, and A.E. Bocîrnea, Low energy electron diffraction from ferroelectric surfaces. Dead layers and surface dipoles in ultraclean Pb(Zr,Ti)O₃(001), *Physical Review B* **96**, 115438(15 pp.) (2017).
- [6] L. C. Tănase, L. E. Abramiuc, D. G. Popescu, A.-M. Trandafir, N. G. Apostol, I. C. Bucur, L. Hrib, L. Pintilie, I. Pasuk, L. Trupină, and C. M. Teodorescu, Polarization orientation in lead zirco-titanate (001) thin films driven by the interface with the substrate, *Physical Review Applied*, accepted (2018).
<https://journals.aps.org/prapplied/accepted/f3071Aa7Ud417d03f08f6917751e95726226b9775>

- [7] L. Pintilie and M. Alexe, Metal-ferroelectric-metal heterostructures with Schottky contacts. I. Influence of the ferroelectric properties, *Journal of Applied Physics* **98**, 124103(8 pp.) (2005).
- [8] L. Pintilie, I. Boerasu, M. J. M. Gomes, T. Zhao, R. Ramesh, and M. Alexe, Metal-ferroelectric-metal structures with Schottky contacts. II. Analysis of the experimental current-voltage and capacitance-voltage characteristics of $\text{Pb}(\text{Zr,Ti})\text{O}_3$ thin films, *Journal of Applied Physics* **98**, 124104(9 pp.) (2005).
- [9] L. C. Tănase, L. E. Abramiuc and C. M. Teodorescu, Photoelectron spectroscopic and microspectroscopic probes of ferroelectrics, *AIP Conference Proceedings* **1916**, 030001(10 pp.) (2017).
- [10] N. G. Apostol, L. E. Ștoflea, L. C. Tănase, I. C. Bucur, C. Chirilă, R. F. Negrea, and C. M. Teodorescu, Band bending at copper and gold interfaces with ferroelectric $\text{Pb}(\text{Zr,Ti})\text{O}_3$ investigated by photoelectron spectroscopy, *Applied Surface Science* **354**, 459-468 (2015).
- [11] I. C. Bucur, L. C. Tănase, L. E. Abramiuc, G. A. Lungu, C. Chirilă, L. Trupină, N. G. Apostol, R. M. Costescu, R. F. Negrea, L. Pintilie, and C. M. Teodorescu, Triggering surface ferroelectric order in $\text{Pb}(\text{Zr,Ti})\text{O}_3(001)$ by deposition of platinum, *Applied Surface Science* **432**, 27–33 (2018).
- [12] X. Hong, J. Hoffman, A. Posadas, K. Zou, C. H. Ahn and J. Zhu, Unusual resistance hysteresis in n-layer graphene field effect transistors fabricated on ferroelectric $\text{PbZr}_{0.2}\text{Ti}_{0.8}\text{O}_3$, *Applied Physics Letters* **97**, 033114(3 pp.) (2010).
- [13] E. B. Song, B. Lian, S. M. Kim, S. J. Lee, T.-K. Chung, M. S. Wang, C. F. Zeng, G. Y. Xu, Kin Wong, Yi Zhou, H. I. Rasool, D. H. Seo, H.-J. Chung, J. S. Heo, S. N. Seo, and K. L. Wang, Robust bi-stable memory operation in single-layer graphene ferroelectric memory, *Applied Physics Letters* **99**, 042109(3 pp.) (2011).
- [14] A. Rajapitamahuni, J. Hoffman, C. H. Ahn and X. Hong, Examining graphene field effect sensors for ferroelectric thin film studies, *Nano Letters* **13**, 4374–4379 (2013).
- [15] N.G. Apostol, G.A. Lungu, I.C. Bucur, C.A. Tache, L. Hrib, L. Pintilie, D. Macovei, and C.M. Teodorescu, Non-interacting, sp^2 hybridized carbon layers on ferroelectric lead zirco-titanate, *RSC Advances* **6**, 67883–67887 (2016).

Ferroelectric/multiferroic heterostructures: potential applications in electronics

Andra-Georgia Boni

*National Institute of Materials Physics, Atomistilor 405 A, Magurele, Ilfov,
077125, Romania*

email:andra.boni@infim.ro; web site: <http://www.infim.ro>

Ferroelectric and multiferroic heterostructures are used as multifunctional materials for their well-known properties. Nowadays possibilities of obtaining high-quality epitaxial thin film structures offers new ways to study different effects as strain or strain gradients, low dimensions, electrostatic conditions at interfaces on the electric characteristics of the possible devices. This approach gives possibility to obtained new properties and to evidenced new phenomena which could be the basis for developing new devices and functionalities. In this way we show that by constructing epitaxial multilayered thin film structures by alternating ferroelectric materials with layers with different magnetic and electric properties new ferroelectric and dielectric characteristics are obtained. We found that the ferroelectric polarization switching is dependent and can be controlled by strain or by different electrostatic boundary conditions. The most significant result is the developing structures with 2^n different and non-volatile polarization states (n -the number of ferroelectric layers separated by $n-1$ isolator layers).

Transient transport properties of nanoelectromechanical systems

R. Dragomir, B.Tanatar , V. Moldoveanu , S.Stanciu

*National Institute of Materials Physics, Atomistilor 405 A, Magurele, Ilfov,
077125, Romania*

A nanoelectromechanical system (NEMS) is a hybrid system made of a mesoscopic system such as a quantum dot, a quantum wire (QW), a single electron transistor, or a 2D lattice and a nanoresonator NR which can be a cantilever (or a tip), a fullerene molecule or a carbon nanotube. If these systems are coupled to wires, they present interest due to their quantum-like behaviour and sensing properties. Either the cantilever can be influenced by the current passing through the QW or the current is influenced by the oscillations of a driven cantilever. Such systems were studied both theoretically [1-7] and experimentally [8-11]. The transient phenomena are only rarely discussed in the literature, within the single-level model and the constant capacitance method and, mostly, only the steady-state regime is analyzed. The quantized vibrational modes of the cantilever tip are called vibrons and are different from phonons. The quantum dispersion of the displacement of the tip depends on the mass, the charge and the frequency of the tip.

A small mass and a large frequency are sought for in the experiments that are undertaken at low temperatures.

We solve the generalized Franck-Condon Master equation (GME) for an open NEMS in the Markov approximation and also take into account the intradot Coulomb interaction and the dissipation of vibrons due to thermal reservoirs. The numerical results coincide with the ones obtained upon employing a Lang-Firsov canonical transformation. The Hamiltonian of the free electrons (one energy level with spin), the free vibrons and the electron-vibron coupling is diagonalized numerically and the wires are described by tunneling operators between the wires and the QW. Upon expressing the tunneling operators in the basis of fully interacting states we obtain the Franck-Condon terms and an explicit form of the "Lindbladian" that describes transport phenomena up to second order in the coupling with the two wires. Observables such as the current, the expectation value of the displacement of the tip can then be computed. At zero temperature and if the Fermi functions of the wires are set in such a way that the upper chemical potential is above all energy levels of the QW and the lower chemical potential is below all energy levels in the QW (in

other words if they allow a current to flow through the QW) then we recover the exact form of a Lindbladian operator. We find that the tip oscillates even if the bias is zero and that the populations with more vibrons have lower amplitudes if the ratio between the electron-coupling and the energy quantum of the tip is smaller. The oscillations of the populations of the states with different vibron number but with the same electron configuration are found to be slightly out-of-phase.

The evolution of the populations of the vibronic states depend on the wavefunction of the electrons within the QW since it is possible to tune the oscillations by moving the tip along the x axis of the QW (in a plane perpendicular to the axis between the tip and the QW). The states with more vibrons are occupied on average to a less extent if the tip is off-centered w.r.t. to the QW. If the tip is moved along the z axis by bringing the tip closer to the QW, the mixing of the states with different number of vibrons is enhanced. The vibron expectation value of the number and the populations of fully many-body states display oscillations even in the transient regime. It is important to mention that the oscillations of the NR displacement settle down within several microseconds to an equilibrium position that is different from the initial one if the bias is finite.

Our intention is to further include the driving of the cantilever thereby studying possible feedback memory effects that are induced via the electron-vibron interaction in NEMS.

References

- 1.P. Weber, H. L. Calvo, J. Bohle, K. Gos, C. Meyer, M. R. Wegewijs, and C. Stampfer, *Nano Lett.* 15, 4417 (2015).
- 2.G. Piovano, F. Cavaliere, E. Paladino, and M. Sassetti, *Phys. Rev. B* 83, 245311 (2011).
- 3.Albrecht et al. *PRB* 87, 085127 (2013)
- 4.Kirton et al. *PRB* 87, 155407 (2013)
- 5.Liliana Arrachea et al. *PRB* 90 125450, (2014)
- 6.A. Erpenbeck et al. *PRB* 91, 195418 (2015)
- 7.D. W. Utami, H-S Goan, and G. J. Milburn, *Phys. Rev. B* 70, 075303 (2004).
- 8.G. A. Steele et al., *Science* 235, 1103 (2009)
- 9.H. B. Meerwaldt, G. Labadze, B. H. Schneider, A. Taspinar, Ya. M. Blanter, H. S. J. van der Zant, and G. A. Steele *Phys. Rev. B* 86, 115454 (2012).
- 10.M. D. LaHaye et al. *Science* 304, 74 (2004)
- 11.Park et al., *Nature* 407, 57 (2000)

Influence of Metal Ions Doping on the Properties of 1D Iron Oxide Nanoparticles

Stjepko Krehula

Division of Materials Chemistry, Ruđer Bošković Institute, P.O. Box 180, HR-10002 Zagreb, Croatia

Due to their favourable properties (nontoxicity, stability, low cost, band gap in the visible range, good magnetic, catalytic, adsorption and absorption properties, etc.) iron oxide nanoparticles are promising candidates for different applications (catalysts, photocatalysts, magnetic materials, gas sensors, adsorbents, absorbents, battery electrodes, supercapacitors, etc.). Properties of iron oxide nanoparticles depend on their crystal structure, crystallite and particle size, particle shape, porosity, and also on the substitution of Fe ions with other metal ions in the crystal structure of iron oxide. In this presentation the results of investigation of the influence of doping with selected metal cations on different properties (unit cell size, crystallite size, particle size and shape, hyperfine magnetic field, IR and UV-Vis absorption, thermal properties) of 1D iron oxide nanoparticles will be presented.

Specific magnetism and magneto-functionalities in amorphous RE-TM thin films

V. Kuncser^{1,*}, A. Stanciu^{1,2}, A. Catrina¹, C. Locovei^{1,2}, A. Kuncser¹,
N. Iacob¹, G. Schinteie¹, M. Valeanu¹,

¹ *National Institute of Materials Physics, 077125, Bucharest-Magurele, Romania*

² *Bucharest University, Faculty of Physics, 077125, Bucharest-Magurele, Romania*

The case of Fe-Gd and Fe-Dy (Dy is strongly anisotropic as compared to the isotropic Gd) thin films of different concentrations of RE (crossing the compensation point), as prepared by RF-magnetron sputtering with enriched ⁵⁷Fe will be detailed. The specific spero-magnetic non-collinear spin structures will be discussed in respect to their ingredients related to randomly distributed single ion anisotropy and the exchange interaction of the involved atoms. The morpho-structural and compositional characterization was realized via Grazing Incidence X-Ray Diffraction, X-Ray Reflectometry, Transmission Electron Microscopy and Scanning Electron Microscopy coupled with Energy Dispersive X-Ray Spectroscopy. Atomic local configurations and magnetic interactions were studied via Conversion Electron Mössbauer Spectroscopy and Superconducting Quantum Interference Device magnetometry whereas the distribution of local magnetization axis was analyzed via vectorial Magneto-Optic Kerr Effect measurements. A specific magneto-optical behaviour when crossing the compensation points will be also presented and specific peculiarities in magneto-conduction experiments will be discussed. Finally, a specific possibility to investigate magneto-optical effects in such micro-structured RE based systems, with micron-sized Laser spots will be emphasised.

Degradation and defects in Perovskite Solar Cells

Lucia Leonat*, Andrei Tomulescu, Viorica Stancu, Mihaela Florea,
Florentina Neatu, Stefan Neatu, and Ioana Pintilie

National Institute of Materials Physics, Magurele, Romania

**lucia.leonat@infim.ro*

Abstract

Thanks to a peerless collection of photo-physical properties, such as strong absorption coefficient, low exciton binding energy (~ 20 meV), long charge carrier diffusion length (>1 μm), deposition by a multitude of processing techniques, solar cell devices with hybrid perovskite achieved over 23% efficiency [1,2]. However, the main drawback is stability. Defects in perovskite films are the foremost source of degradation processes and generate inconsistencies in current-voltage curves and hysteresis, providing the pathway for ions migration and charge traps, that further initiate the degradation of the perovskite films. Two main sources for defect occurrence are closely related to the fabrication process and originate from: incomplete surface coverage or pinholes, and crystallization, which depends on the local properties of the material and specifically on the presence of structural and chemical defects. All defects will have an impact on the electronic and optoelectronic properties, ultimately reducing the power conversion efficiency in devices.

References

- [1]. A.B. Djuri, F.Z. Liu, H.W. Tam, M.K. Wong, A. Ngb, C. Surya, W. Chen, Z.B. He, *Progress in Quantum Electronics* 53 (2017) 1–37,
- [2]. <https://www.nrel.gov/pv/assets/images/efficiency-chart-20180716.jpg>, accessed august 2018,

Optical Properties of TiO₂ in Doped State: the Influence of the SiO₂ and Silver Nanoparticles

Andreea Nila,¹ Mihaela Baibarac,¹ Alice Mateescu,² Gheorghe Mateescu²

¹ National Institute of Materials Physics, Laboratory of Optical Processes
in Nanostructured Materials, Atomistilor street 405A, P.O.Box MG-7,
R077125, Bucharest, Romania

² Horia Hulubei National Institute for Physics and Nuclear Engineering,
Magurele-Bucharest, Ilfov, Romania

Titanium dioxide (TiO₂) has been widely used in various applications involving microelectronics [1], healthcare [2] and environment [2]. In the last decade, a special attention was given to the exciton-phonon interactions [3], the photocatalytic properties [2, 4] and antimicrobial activity of TiO₂ and its composites with carbon nanoparticles or conjugated polymers [2, 4].

The optical properties of the nitrogen-doped TiO₂ (TiO₂:N) as well as their mixtures with different concentrations of Ag and/or SiO₂ nanoparticles (0.5, 1 and 2 wt.%), prepared by mechanic-chemical interactions, will be shown. The influence of nanoparticles on the host material is evaluated by studies of Raman scattering, photoluminescence (PL), photoluminescence excitation (PLE) and UV-VIS spectroscopy.

An approach to improving the efficiency of TiO₂:N is to avoid the recombination of electrons and holes by using charge-transfer catalysts. The TiO₂:N/SiO₂ and TiO₂:N/Ag systems have a promising potential to control the efficient charge transfer. In this context, the UV-VIS reflectance studies indicate a shift of the band gap of TiO₂:N to the UV range as increasing of the SiO₂ and Ag nanoparticles concentration in the studied mixtures. The presence of Ag and SiO₂ in the host material indicates no broadening, shifting or additional lines in the Raman spectra. The PL intensities were decreased with increasing the Ag and/or SiO₂ nanoparticles concentration in host matrix mass, indicating the potential collectors of these materials. In order to explain these processes, the different de-excitation ways will be advanced, taking into account energy levels diagram of the TiO₂:N/SiO₂, TiO₂:N/Ag and TiO₂:N/Ag/SiO₂ systems. The plasmonic effect of Ag nanoparticles in above systems is highlighted for the first time by PLE studies.

Acknowledgement

This work was supported by a grant of the Romanian Ministry of Research and Innovation, CCCDI – UEFISCDI, project number PN-III-P1-1.2-PCCDI-2017-0350 / 44PCCDI / 2018, within PNCDI III.

References

- [1] Gyanan, S. Mondal, A. Kumar, *Superlattices and Microstructures* **100**, 876-885, 2016.
- [2] S. Ghosh, A. P. Das, *Toxicological & Environmental Chemistry* **97**, 5, 491-514, 2015.
- [3] A. Nila, I. Baltog, D. Dragoman, M. Baibarac, I. Mercioniu, *Journal of Physics – Condensed Matter* **29**, 365702, 2017.
- [4] I. C. Nica, M. S. Stan, M. Popa, M. C. Chifiriuc, G. G. Pircalabioru, V. Lazar, I. Dumitrescu, L. Diamandescu, M. Feder, M. Baibarac, M. Cernea, V. A. Malaroiu, T. Popescu, A. Dinischiotu, *Nanomaterials* **7**, 279, 2017.

The influence of synthesis parameters on iron oxide nanoparticles

Roxana Mioara Piticescu¹, Laura Madalina Cursaru¹, Ana-Maria Mocioiu¹, Dumitru Valentin Dragut¹, Adriana Gabriela Plaiasu², Catalin Marian Ducu²

¹*National Research-Development Institute for Non-Ferrous and Rare Metals, (INCDMNR-IMNR), 102 Biruintei Blvd., 077145, Pantelimon, Ilfov, Romania*

²*University of Pitesti, 1 Targu din Vale Street, Pitesti, Romania*

Biomedical applications of magnetic nanoparticles are of real scientific interest due to their magnetic, optical and electrical properties, as well as to the dimensional properties, surface-to-volume ratio, controllable morphology, functionality, bioavailability and improved biotolerability. Among the promising candidates for this purpose, magnetite nanoparticles (MNP) occupy an important place due to their good compatibility with the biological environment and low toxicity. The real potential for applying MNPs is, however, strongly dependent on their physicochemical properties, which are related to the synthesis process. Functionalization or coating of MNPs has been shown to directly influence magnetic susceptibility, colloidal stability, size, efficacy of cellular absorption and biodistribution.

In this study, iron oxide nanoparticles were synthesized at temperatures of 100-200° C and working pressures between 20-1000 bar. It has been found that the synthesis pressure influences the type of crystalline phase. Thus, at less than 100 atm pressures, iron oxide is predominantly formed as hematite, while at pressures above 100 atm, the major crystalline phase is goethite. Also, the crystallites size and medium particle size decreases with increasing pressure (for samples synthesized at $P \leq 100$ atm). Complex thermal analysis by the DSC method revealed the polymorphic changes of iron oxides at different temperatures.

Acknowledgement

The financial support of ERANET-EURONANOMED 2 project, acronym NANOVIBER, UEFISCDI ctr. no.1/2017 is gratefully acknowledged.

Organic Light Emitting Diodes (OLED): Past and Future

S. Polosan

*National Institute of Materials Physics, R-077125 Bucharest, Magurele,
Romania*

Organic Light Emitting Diodes (OLED) enter now in the third phase concerning their efficiency. In these devices, the emissive electroluminescent layer is composed of carbon-based (organic) semiconductors, typically aromatic small molecules, in contrast to the inorganic crystalline semiconductors used in traditional LEDs. If the first devices are based on pure organic materials, the second and the third generations are based on combinations between metals and organic ligands in so-called organometallics for which their external quantum efficiency is significantly increased. The second generation is now widely used in large displays reaching high efficiency because of the spin-orbit coupling which induces intersystem crossing between metals and their ligands. The third generation of OLED comprises in increased external quantum efficiency obtained by proper choice of the ligands, reaching a theoretical value of 100%. A brief description of these OLEDs will be presented together with their advantages and the obtained technologies for the next generation of displays.

Microstructural and optical properties of electrospun metal oxide nanofibres

Mira Ristić

Ruder Bošković Institute, P.O.Box 180, 10002 Zagreb, Croatia, (email: ristic@irb.hr)

One-dimensional (1D) metal oxide nanostructures are promising materials for different advanced applications in electronics, energy conversion and storage, gas-sensing, catalysis and photocatalysis. To produce these nanostructures various synthesis approaches can be applied. Among them, electrospinning method has received a remarkable interest. It allows the synthesis of very long fibres having diameter of tens to hundreds nanometers. The electrospinning is based on the effect that high voltage has on viscous, conductive polymer solution. When an applied electrostatic charge overcomes the surface tensions of the polymer solution an electrically charged polymer jet is formed.¹ The electrospun nanofibres are then collected on the opposite charged electrode. Finally, the electrospun metal oxide nanofibres are produced by calcination of as-spun fibres. Their properties will depend on the chemical and physical parameters of electrospinning process as well as the parameters of heating treatment. In this presentation the formation of Zn-, Ni-, Ru- and Fe-oxide nanofibres by electrospinning will be presented. The corresponding metal salts $Zn(NO_3)_2$, $Zn(ac)_2$, $Ni(NO_3)_2$, $Fe(NO_3)_3$ or $Ru(NO)(NO_3)_3$ were dissolved into C_2H_5OH solvent already containing polyvinylpyrrolidone ($M_w = 1300000$). Electrospinning of viscous solution in the system PVP- C_2H_5OH - H_2O - $Zn(ac)_2$ produced fibres which were additionally heated at 400 and 600 °C producing the fibres network consisting of primary ZnO particles with maximum width between ~20 and 80 -100 nm.² 1D ZnO nanoparticles were grown perpendicularly onto electrospun ZnO fibres at 160 °C in aqueous medium containing zinc(II)-acetylacetonate.³ In the system PVP- C_2H_5OH - H_2O - $Ni(NO_3)_2$ at lower concentrations of $Ni(NO_3)_2$ a porous microstructure consisted of interconnected fibres was obtained, whereas at a high $Ni(NO_3)_2$ concentrations a laminar microstructure was produced.⁴ Electrospinning of viscous PVP- C_2H_5OH - H_2O - $Ru(NO)(NO_3)_3$ solution followed by heating of the precursor fibres at 400 °C yielded the ribbon-like RuO_2/Ru nanofibres.⁵ In addition, the influence of metallic dopants on the formation and properties of γ - Fe_2O_3 nanofibres will be also presented.⁶ The differences obtained in the synthesis of these metal oxides by electrospinning method will be shortly discussed.

References

1. S. Ramakrishna, K. Fujihara, W.-E. Teo, T.-C. Lim, and Z. Ma, *An Introduction to Electrospinning and Nanofibers*, World Scientific Publishing Co. Pte Ltd., Singapore, 2005., pp. 396.
2. M. Ristić, M. Marciuš, Ž. Petrović, M. Ivanda, S. Musić, *Croat. Chem. Acta* **87** (2014) 315–320.
3. Ž. Petrović, M. Ristić, M. Marciuš, M. Ivanda, S. Musić, *Mat. Lett.* **176** (2016) 278-28.
4. M. Ristić, M. Marciuš, Ž. Petrović, M. Ivanda, S. Musić, *Mater. Lett.* **156** (2015) 142–145.
5. M. Ristić, M. Marciuš, Ž. Petrović, S. Musić, *Ceram. Int.* **40** (2014) 10119-10123.
6. M. Ristić, A. Kremenović, M. Reissner, Ž. Petrović, S. Musić, Microstructural and magnetic properties of electrospun hematite/cuprospinel nanocomposite, 2018, *in preparation*.

Photoelectrochemistry of water splitting from first principles

Nicola Seriani

ICTP - Trieste, Italy

First-principles simulations based on density functional theory can provide insight into the behaviour of electrode materials for photoelectrocatalytic devices. In order to achieve this, it is crucial to provide a realistic description of the effects of the complex environment on materials, interfaces and processes, in presence of the electrochemical interface, illumination and electric bias. In this talk, I will show how the environment can be taken into account, and how parameters relevant for materials performance can be extracted from the simulations, with particular reference to water splitting. A detailed understanding of mechanisms acting at atomic level can be attained. Finally, limitations of this approach and future research directions will be discussed.

Vibronic and chemical properties of supported single metal atom catalysts

E. Vesselli

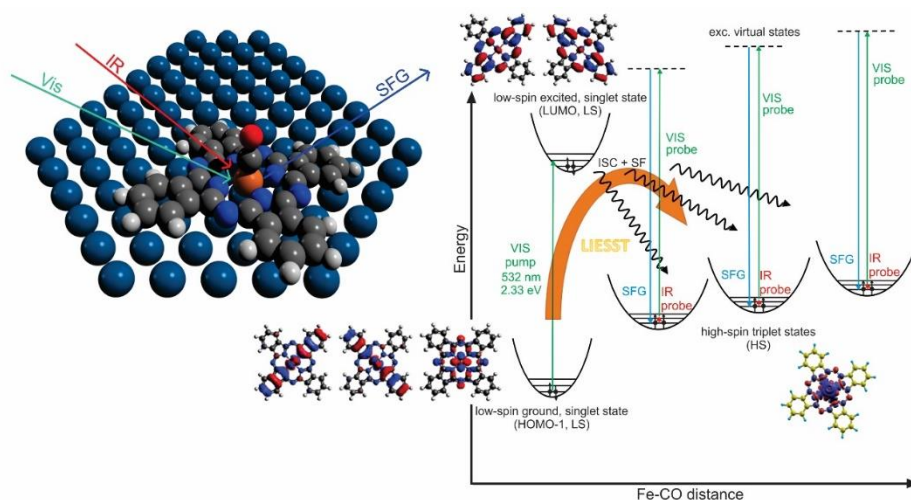
Dipartimento di Fisica, Università degli Studi di Trieste, via Valerio 2 –
34127 Trieste, Italy

and

CNR-IOM, SS 14 km 163.5 – Basovizza (Trieste), Italy

evesselli@units.it

Innovative and stable catalysts can be prepared within the framework of a biomimetic approach, thus embedding an active single metal atom in a tetra-pyrrolic cage. From the surface science point of view, an *in situ* and *operando* characterization of heme-like, simplified model systems may represent a challenge. Besides investigations at cryogenic temperature, a thorough atomic-level experimental understanding is not straightforward so far due to the near-ambient pressure conditions that are necessary to yield a significant interaction of the active core with gas phase molecules at room temperature. By exploiting non-linear laser spectroscopy, access to the vibronic properties of interfaces is possible under realistic operative conditions, allowing the investigation of 2D metal-organic supported systems.



Self-assembled 2D layers of metal-N₄ complexes deposited at single crystal terminations [1] and over supporting templates like graphene [2] or oxide films [3] will be described, with a specific focus on the interaction with

small gas-phase molecules. IR-Vis Sum Frequency Generation spectroscopy data combined with *ab initio* calculations provide a detailed insight into the structural and chemical behavior of the layers, including the role of Frenkel excitons [2]. The latter form upon illumination with visible light and, initially localized at the reactive centers, evolve through associated spin transition and singlet fission mechanisms, affecting the adsorbed ligand, i.e. the chemical reactant.

References

- [1] M. Corva and E. Vesselli, *J. Phys. Chem. C* **120** (2016) 22298.
- [2] M. Corva, A. Ferrari, M. Rinaldi, Z. Feng, M. Roiaz, C. Rameshan, G. Rupprechter, G. Pastore, G. Comelli, N. Seriani, and E. Vesselli, *Nat. Comm.* *in review*.
- [3] M. Corva, F. Mohamed, Z. Feng, T. Skala, G. Comelli, N. Seriani, M. Peressi, and E. Vesselli, *ACS Nano*, *in review*.